Universitat Autònoma de Barcelona

FACULTAT DE CIÈNCIES

DEPARTAMENT DE FÍSICA

NEUTRON SPECTROMETRY AND DOSIMETRY FOR RADIATION PROTECTION AROUND A HIGH ENERGY ELECTRON / POSITRON COLLIDER

TESIS DOCTORAL

Presented by
ROBERTO BEDOGNI

Supervised by
Prof. **FRANCISCO FERNÁNDEZ**

July 2006

Universitat Autònoma de Barcelona

FACULTAT DE CIÈNCIES

DEPARTAMENT DE FÍSICA

NEUTRON SPECTROMETRY AND DOSIMETRY FOR RADIATION PROTECTION AROUND A HIGH ENERGY ELECTRON / POSITRON COLLIDER

TESIS DOCTORAL

Presented by
ROBERTO BEDOGNI

Supervised by
Prof. **FRANCISCO FERNÁNDEZ**

Keywords: neutron, spectrometry, dosimetry, Bonner spheres, unfolding, radiation protection

July 2006

Contents

Chapter 3

THE BONNER SPHERE SPECTROMETER USED AT THE INFN FRASCATI NATIONAL LABORATORIES

Chapter 4

Chapter 5

Chapter 6

Chapter 7

Chapter 8

Chapter 9

Introduction

Particle accelerators, designed at the beginning for research applications, are now widely used in various aspects of life. Fields such as medical diagnosis, therapy, radio-pharmacy, material and polymer science, waste sterilization, food conservation, non-destructive inspection, etc. are heavily employing such devices. Moreover, European projects have been investigating in the fields of accelerator driven radioactive waste transmutation and fusion based energy production.

Despite a unique definition of *particle accelerator* can't be found in literature, a statement by E. Persico (Persico, 1968) could be adopted: *"Particle accelerators are machines built with the aim of accelerating charged particles to kinetic energies sufficiently high that they can be used to produce nuclear reactions".*

Though the definition doesn't cover the whole range of existing machines, yet it introduces the complexity of the radiation fields around accelerators, originated from the interaction of primary particles with targets, barriers and structural materials.

Since the discovery of X-rays (1895), the relevant aspects of radiation protection have been studied at accelerator facilities: the biological effects of radiation, the radiation syndromes, the activation of air and materials, and the studies on the radiotoxicity of the transuranic elements.

Owing to the peculiarities of such machines, in terms of complexity of the structures and type and energy of the radiation fields, it could be affirmed that they constitute the most complete training environment for radiation protection: "*..(at accelerators)..the science and technology of radiation dosimetry are at their most sophisticated. In only one other class of radiation environments, those met in extraterrestrial exploration, do such novel and diverse dosimetric challenges need to be faced. Even here the dosimetrist doesn't encounter the range of particle intensities, variety of radiation environments, or pulsed characteristics of radiation fields"* (Swanson, 1990).

At the Frascati National Laboratories (LNF) of the Italian National Institute for Nuclear Physics (INFN), an historical accelerator-based installation has been operating since the end of the '50s. It is in Frascati that some of the most advanced developments have been undertaken, such as the colliding beam technology and the radiation protection around accelerators. Since 1997, the 510 MeV electron / positron collider, DAΦNE, is operating at the LNF. DAΦNE is chosen as a workplace neutron field for this work.

At the LNF radiation protection group, an ad-hoc project has been set up to characterize the neutron fields around the accelerator, which are generated by the interactions of the beam with the deflecting devices, the attenuation and shielding elements and in general the structures of the accelerator itself. The instrument chosen for the spectra measurements is a commercial Bonner Spheres Spectrometer (BSS), with an additional lead loaded sphere for high energy neutrons.

A new unfolding code, FRUIT (FRascati Unfolding InTeractive), has been developed for the needs of the LNF radiation protection group.

Measurements with the Bonner Spheres Spectrometer were performed around the DAΦNE accelerator, for the accurate determination of the radiation protection related quantities. The results have been implemented in the radiation protection practices, for a better interpretation of the results from the routine survey-meters as well as the dose evaluation procedures.

Chapter 1 of this work introduces the radiation protection problems around the high energy electron accelerators.

Chapter 2 is a brief overview of the neutron dosimetry and spectrometry techniques, with special attention to the radiation environment at particle accelerators.

Chapter 3 introduces the Bonner Spheres Spectrometer used for the study, which is commercially available from Ludlum (*www.ludlums.com*). It consists of a ^{6}LiI(Eu) 4 mm x 4 mm scintillator and six polyethylene spheres of density 0.95 g.cm^{-3} and diameters 2”, 3”, 5”, 8”, 10”, 12”. Special attention has been given to the seventh additional 12” sphere, which includes a 1 cm lead layer with inner diameter 3”. This makes possible to obtain spectral information in the energy range above 20 MeV, due to the nuclear reactions Pb(n,xn).

Extensive efforts have been made to carry out all the calibration required such as:

- the neutron calibration with a known strength ^{241}Am-Be source;
- the tests with photons from ^{137}Cs and ^{60}Co to determine the photon sensitivity;
- the reproducibility routine checks, performed with a specially designed portable device, provided with a small ^{241}Am-Be neutron source.

Chapter 4 reports the energy response functions of the various spheres (response matrix), which has been taken from literature and partially verified with the MCNP Monte Carlo code.

Chapter 5 describes the experimental validation of the spectrometer response matrix, performed at the ENEA-Bologna Secondary Standard Calibration Laboratory, with the reference neutron fields of ^{241}Am-Be, ^{252}Cf, ^{252}Cf(D_2O) and thermal neutrons.

Chapter 6 introduces the unfolding algorithms. The “robust convergence” algorithm, which is on the basis of both the MITOM code, from UAB, and FRUIT, from LNF, is explained. Finally, the FRUIT code, specially developed for the needs of the LNF radiation protection group, is addressed in detail.

Chapter 7 reports the performance of the FRUIT unfolding code, tested with different reference neutron spectra.

Chapter 8 describes the spectrometric measurements obtained with the LNF Bonner Sphere Spectrometer around the DAΦNE facility, where neutron fields are produced from the interaction of the primary 510 MeV electrons and positrons with the targets, the accelerator structures and the barriers. The Bonner spheres readings have been unfolded using the FRUIT code. A special study is devoted to the measurement of high energy photo-neutrons. The unfolded spectra are then folded with the appropriate fluence-to-dose conversion factors, in order to obtain the ambient dose equivalent values in the points of test. Such values are compared with those directly obtained from the instrument used in the routine ambient monitoring, the rem counter Berthold LB6411. Workplace calibration factors are then derived for the mentioned instrument, in order to provide dosimetric procedures with improved accuracy for the routine surveillance of the installation.

The conclusions and the perspective for future development are reported in Chapter 9.

Chapter 1

RADIATION PROTECTION PROBLEMS ASSOCIATED WITH NEUTRON AND PHOTON FIELDS AT HIGH ENERGY ELECTRON ACCELERATORS

1.1 **The “source terms”**

The radiation “environment” at electron accelerators is a consequence, direct or indirect, of the interaction of the primary particles, i.e. the electrons intentionally generated and accelerated, with the targets, the shutters, the accelerator structures and barriers (Esposito, 1992). Moreover, additional source terms can arise from the high power radiofrequency generators (klystrons), the high voltage valves such as the triodes and the electron source (electron gun). The variety, complexity and intensity of the secondary radiation fields depend on the accelerator configuration, the energy and current of the primary electrons.

In general, all electron accelerators contain the same basic configuration: the vacuum chamber, where electrons are driven, the associated radiofrequency power equipment, a number of magnets for deflecting and focusing the beam, the vacuum system, the water cooling system, the beam diagnosis instrumentation, the safety devices, the radiation shielding and the structures of the experiments to be performed. All mentioned elements can have a direct or indirect impact on the radiation environment and radiation safety aspects.

As far as the primary electron energy is concerned, it defines the variety of radiation protection problems that can be encountered. In general, by “high energy”, it is meant that the energy interval is above few tens of MeV, where the electromagnetic cascade dominates the interaction of the beam with matter.

For electron energy below 10 MeV, it can be roughly assumed that the secondary fields is only given by bremmstrahlung photons, originated in the interaction of the primary electrons with the accelerator structures, targets and barriers. Ozone can be generated by air ionization from electrons travelling in air.

Above 10 MeV, the interaction of secondary photons with high Z materials can produce neutrons by means of photo-production (γ, n) reactions. Neutrons can also be produced by electro-production reactions (e, n), but the associated cross section is two orders of magnitude lower than for the (γ, n) reaction. The photo-production reactions are characterized by an energy threshold, which ranges in 8-10 MeV for all materials used for targets and structures. A related problem is the activation of the materials, due to the photo-reactions and the interaction of the secondary neutrons.

Photonuclear (γ, n) reactions with carbon, nitrogen and oxygen of the air can produce ^{11}C

(threshold 20 MeV), ^{13}N (10.6 MeV) and ^{15}O (15.7 MeV). Above 213 MeV, the production of muon-antimuon pairs becomes possible.

1.2 Radiation safety impact of the accelerator configuration

Figure 1.1 represents the schematic diagram of the structure of an accelerator, and the constitutive elements shown here, are considered for their radiological impact.

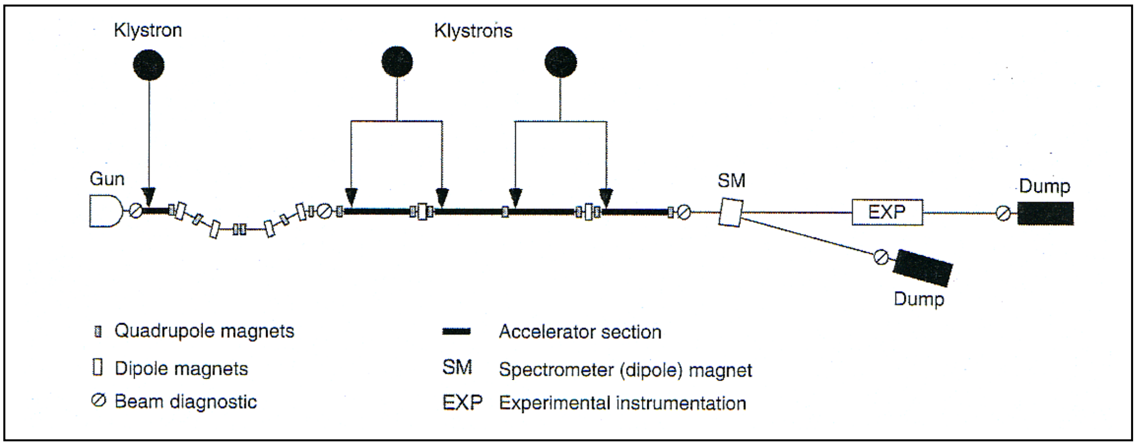

Figure 1.1: The typical structure of a LINAC. Taken from (Vylet, 2001).

1.2.1 *Klystrons*

A klystron (Figure 1.2) is a RF power amplifier, which provides energy to accelerate the electrons in the accelerator sections. The low power input RF is amplified in the klystron cavity by the passage of electron bunches, accelerated from 100 to 400 kV and stopped in the klystron collector, with consequent production of bremmstrahlung X-rays. Since such devices are located outside the accelerator building, their shields have to be carefully dimensioned and periodically verified. Though the klystron collector is always shielded by the manufacturer, with 5-10 cm of lead, yet additional shields are usually required around the whole structure (See Figure 1.2).

Figure 1.2: A modern klystron with its power supply at the LNF. Even though the manufacturer shielded a large part of the device, yet additional lead foils were necessary to protect the surrounding working area.

1.2.2 *The electron gun*

The electron gun constitutes the first part of the LINAC. It can be seen as a cathode plus an extraction system. The cathode is called:

· *thermionic*, or *hot cathode*, if an heating system is used to reduce the work function for the extraction of the electrons.

· *photocatode*, if laser pulses are used to extract electrons.

Both types of cathodes can be coupled with a Direct Voltage (*DC HV gun*) or RF (*RF gun*) extraction systems. Since the electron bunches in the accelerator must have a well defined spatial and time structure, the accelerator section, immediately after the gun, operates in a drastic selection of the produced electrons. For this reason such section usually constitutes a strong source of low energy X-rays.

1.2.3 *Magnets*

Dipole magnets are used to deflect the electron beam into the desired direction. Low current dipoles are used, e.g. for adjusting trajectories in LINACs, whilst big elements are used to steer the beam in accumulation rings or “chicane” structures. A “chicane” is a series of dipoles arranged in order to select only particles in a given momentum range. Dipoles constitute a potential radiation source, since they stop all particles of energy and/or trajectory that are not adequate to be deflected in the desired direction. Moreover, all kinds of electric failure in the magnets will deflect the particles in unwanted directions, producing photon and neutron radiation fields. Local shields are usually placed around the dipoles in order to reduce such leakage radiation.

Quadrupole magnets are used to focus the electron beam, for instance they're placed before and after the bending magnets. Sextupoles and Octupoles are used for higher degree corrections in the beam optics. Also these elements can produce stray leakage radiation in case of mis-steering.

1.2.4 *Beam diagnostics*

This includes a wide range of devices used to monitor various beam parameters, such as shape and profile. Some of them are external to the beam, such as the Average Current Monitors (ACM), i.e. toroids mounted on the beam line, giving an induced current which is proportional to the beam current. The use of other devices can imply the insertion of wires or fluorescence screens on the beam-line. Faraday cups are massive chambers, usually placed at the end of a beam line, which completely stop the beam to measure the time integrated transported charge. In general, beam diagnostics can cause beam losses and then undesired radiation fields.

1.2.5 *Other devices*

Experimental equipments are, in general, systems of targets and collision detectors which, in principle, can generate undesired secondary radiation.

The distilled water of the cooling system can be activated, since it can be used to cool components which are directly exposed to the beam, such as beam stoppers or collimators.

The vacuum system is usually distributed along the beam line with a series of vacuum sections, valves and pumps. A number of vacuometers placed along the beam line are usually part of the safety system, since an unwanted residual air pressure inside the beam pipe can cause stray radiation fields.

1.3 **Prompt radiation fields**

The interaction of the primary beam with the accelerator structures generates prompt photon and neutron fields, especially in correspondence of injection sections, collimators, large angle bending magnets, scrapers and beam stoppers. In electron / positron machines, like DAΦNE, attention has to be paid to a special section of the LINAC, the electron to positron converter. It is a target where a 10 A current of 250 MeV electrons produces positrons, via pair production effect, with an efficiency of about 0.9%.

The importance of the various contributions to the prompt radiation field in electron accelerators, supposing electron beams striking targets in unshielded condition, is shown in Figure 1.3 (Vylet, 2001). Here the ambient dose equivalent rate per unit beam power, at 1 m from high Z targets, is plotted as a function of the beam energy, for various field components: bremmstrahlung X-rays, prompt neutrons, muons and activity induced in the materials.

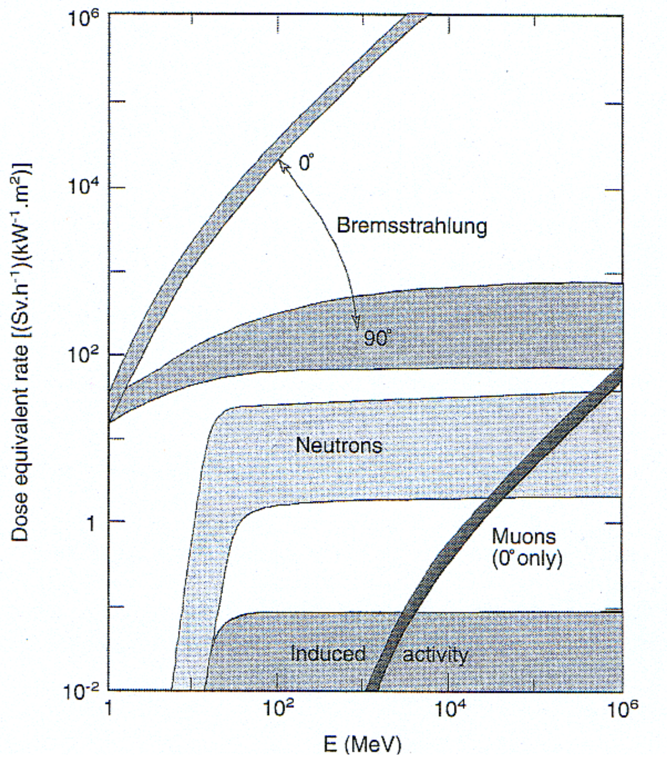

Figure 1.3: The importance of various contributions to the prompt radiation field in electron accelerators, assuming electron beams striking targets in unshielded conditions. Taken from (Vylet, 2001).

1.4 The electromagnetic cascade

The interaction of electrons striking target materials at energy of hundreds MeV can be described using the *electromagnetic cascade* concept (EMC). The EMC is the process for which electrons loose their energy by conversion in photons, and vice-versa (Figure 1.4). High energy electrons loose their energy mainly by radiative (bremmstrahlung) process; this generates high energy photons which produces e^+/e^- pairs, and so on. During the radiative stage it can be assumed that the electron energy decreases continuously:

$$dE = -\frac{E}{X_0}dx \qquad (1.1)$$

Where *E* is the electron energy, *dE* the energy decrement, *dx* the infinitesimal material thickness and X_0 the constant of the attenuation process, called *radiation length*. By integrating equation 1.1, the residual electron energy at the depth *x* is given by:

$$E(x) = E_0 \cdot e^{-\frac{x}{X_0}} \qquad (1.2)$$

The process can be depicted as in Figure 1.5, where an electron of energy *E* penetrates a thickness ξ (half value layer), after that shares its energy with a bremmstrahlung photon; after another ξ the process is repeated, moreover the photon is transformed in an e^+/e^- pair, and so on. The energy degradation and the multiplication process of the secondary particles are regulated by the same factor.

The radiation length X_0 (g·cm^{-2}) is only the function of the material (mass number *A* and atomic number *Z*):

$$X_0 = \frac{716 \cdot A}{Z \cdot (Z+1) \cdot \ln \frac{287}{\sqrt{Z}}} \qquad (1.3)$$

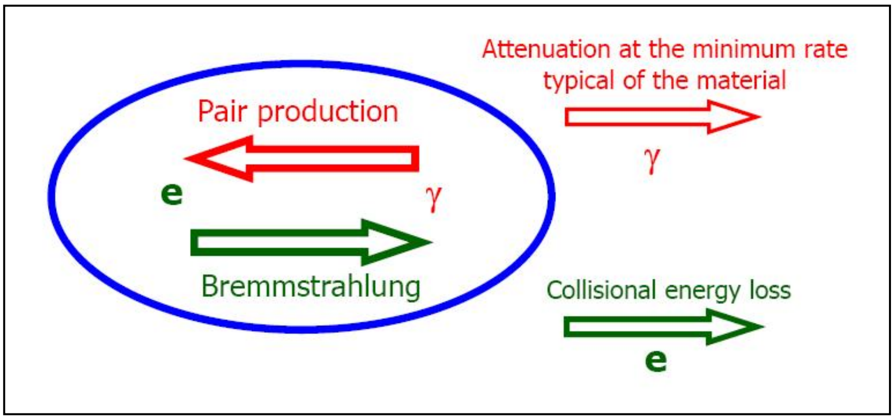

Figure 1.4: Schematization of the electromagnetic cascade process.

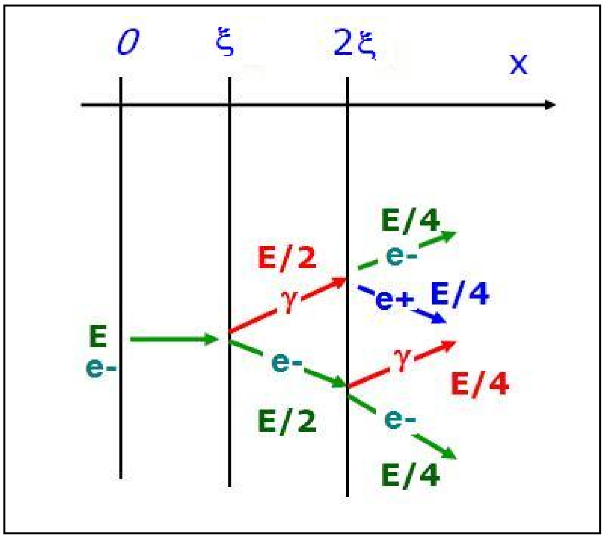

Figure 1.5: Energy degradation and particle multiplication processes.

The dose rate around the target will reach its maximum value when the number of secondary particles will be maximum (maximum of the EMC).

This iterative process continues until the electrons energy falls below the *critical energy* (E_c) of the material, i.e. the electron energy at which the collisional and the radiative losses have the same importance. The parameter E_c is only a function of the atomic number of the material, Z:

$$E_c = \frac{800}{Z + 1.2} \qquad (1.4)$$

For high Z materials, such as lead ($Z = 82$), E_c is of the order of 10 MeV. When electrons approach the E_c limit, they stop contributing to the EMC. This point corresponds to the maximum of the EMC. The photons continue contributing to the EMC by producing e^+/e^- pairs, until the Compton Effect dominates their attenuation process. During attenuation in a material, photons naturally tend to accumulate at the energy value at which the total absorption cross section is minimum (the *maximum transparency energy* or *Compton window, E_{min}*). Therefore, also photons stop contributing to the EMC when their energy approaches E_{min}. For most of the materials the following relation between E_c and E_{min} is valid: $0.3\ E_c < E_{min} < 0.5\ E_c$.

The spatial profile of the process is shown in Figure 1.6, where the fraction of total energy deposited by the EMC per unit length is reported as a function of the depth in the material, normalized to the non-dimensional length parameter λ:

$$\lambda = \frac{325 \cdot \ln E_0}{(\ln Z)^{1.73}} \qquad (1.5)$$

E_0 represents the initial electron energy.

The EMC reaches its maximum at the depth X_{max}, which depends on the critical energy E_c, the initial electron energy E_0 and the radiation length X_0:

$$X_{\max} = 1.01 \cdot X_0 \cdot (\ln \frac{E}{E_c} - 1) \qquad (1.6)$$

The radial distribution of the cascade is described in terms of Molière radius, defined as $X_m = X_0 \frac{21.2}{E_c}$. About 90% of the energy is deposited in 1 X_m, 99% in 3.5 X_m.

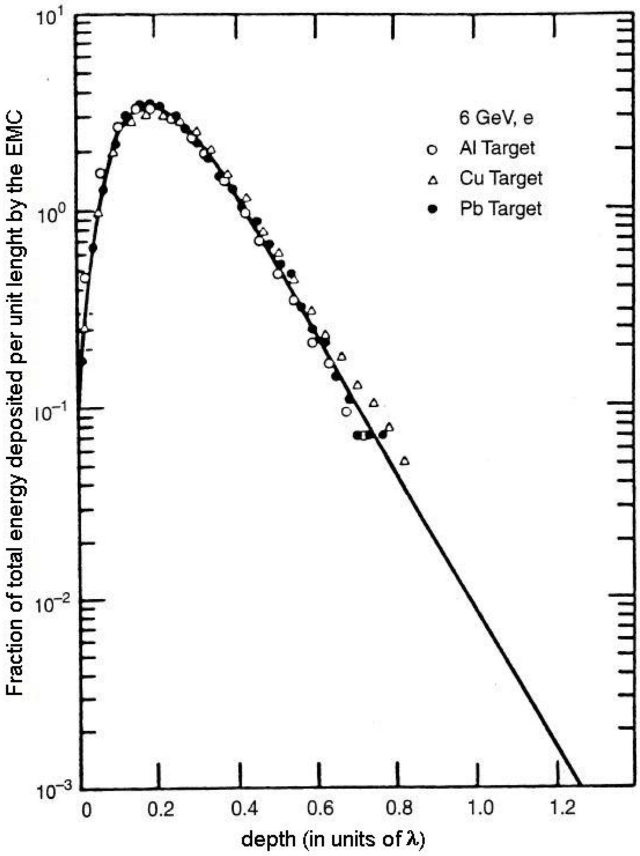

Figure 1.6: Spatial profile of the Electromagnetic cascade. The quantity in ordinate is the fraction of total energy deposited per unit length, where the length is expressed in units of λ. Taken from (NCRP, 2004).

1.5 The photon field

Supposing an electron beam striking a high *Z* target, the energy distribution and the intensity of the bremmstrahlung photon field are function of the target thickness, *t*, and angle of observation, θ. In the “thin” target hypothesis, i.e. $t << X_0$, the photon yield increases as *t* increases, with the same slope as the initial part of the curve in Fig. 1.6. The photon production reaches its maximum for $t = X_{max}$ (optimized target), then, for higher values of *t*, it decreases due to the photon attenuation in the target itself. In radiation protection calculations, the conservative hypothesis of “optimized target” is often used. In such hypothesis, the absorbed dose rate per unit beam power at a distance of 1 m from an optimized target, as a function of the incident electron energy E_o is given in Figure 1.7 for incidence angles of 0° and 90°.

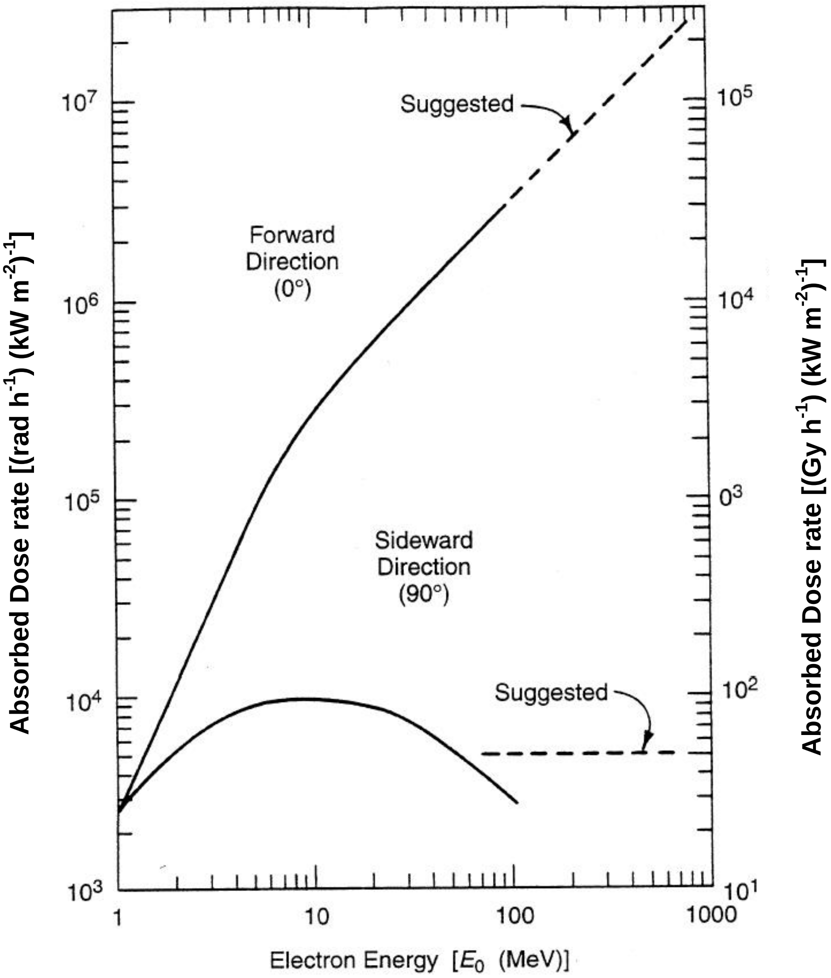

Figure 1.7: Thick target bremmstrahlung yield from a high *Z* target. The absorbed dose rate per unit beam power at a distance of 1 m from an optimized target, as a function of the incident electron energy *Eo* is given for incidence angles of 0° and 90°. Taken from (NCRP, 2004).

The curves of Figure 1.7 are quantified by the Swanson "rules of thumb" (Swanson, 1979), here reported with *dD/dt* = absorbed dose rate at 1m (Gy·h^{-1}·kW^{-1}) and E_o expressed in MeV.

Rule 1 $$\frac{dD}{dt} = 20 \cdot E_0^{\,2} \quad (\theta = 0° \text{ and } E_o < 20 \text{ MeV}) \tag{1.7}$$

Rule 2 $$\frac{dD}{dt} = 300 \cdot E_0 \quad (\theta = 0° \text{ and } E_o > 20 \text{ MeV}) \tag{1.8}$$

Rule 3 $$\frac{dD}{dt} \approx 50 \qquad (\theta = 90° \text{ and } E_o > 100 \text{ MeV}) \tag{1.9}$$

The bremmstrahlung radiation is highly forward peaked. The parameter $\theta_{1/2}$ is used to express the angle at which the intensity falls to one half of the 0° value. $\theta_{1/2}$ is inversely proportional to the initial energy, so if E_o increases, the emission is more forward peaked.

$$\theta_{1/2} = \frac{100}{E_0} \qquad (1.10)$$

The forward emission can be very penetrating, since it contains all energies from 0 to E_o. The energy distribution of the photon fluence, $\frac{d\phi_\gamma}{dE}$, is roughly proportional to $1/E^2$ for thick targets, whilst for thin targets the following approximation is more adequate:

$$\frac{d\phi_\gamma}{dE} \alpha \frac{t}{X_0 \, E} \qquad (1.11)$$

The photon emission at wide angles, such as 90°, doesn't depend on the electron energy (equation 1.9) but only on the beam power. Moreover, a very high fraction of emitted photons have energy lower than 10 MeV. Those below 1.5 MeV are produced by Compton interaction, whilst the higher energy component is given by small angle bremmstrahlung from secondary electrons scattered at wide angles from the beam line (Mao, 2000). Such photons are typically produced by electrons in the maximum of the EMC, so their energy distribution will have a "natural" accumulation point around the maximum transparency energy (typically between 3 and 5 MeV).

When traveling in a straight path, the electron beam can produce bremmstrahlung by interacting with the atoms of residual air in the beam pipe. The so called "gas-bremmstrahlung" (Pelliccioni, 1987), produces an extremely forward peaked and highly penetrating photon emission, which constitutes a potential way of exposure at synchrotron light facilities, where it can propagate along the experimental channel tangential to the accelerator rings. For this reason, terminal shields of 20-30 cm of lead are usually put at the end of the synchrotron light lines.

1.6 The neutron field

The neutrons in a high energy electron accelerator are produced by photonuclear reactions, as (γ, n) (γ, 2n), (γ, pn) and electro-nuclear (e, e'n), but photons have larger nuclear cross sections (10^2 times) than electrons. Therefore, neutrons and other particles escaping from nuclear inelastic reactions, mainly come from the photon component of the EMC. Such reactions are characterized by a threshold energy value, corresponding to the binding energy of the "last nucleon" in the nuclear structure. The energy threshold ranges in 8-10 MeV for high *Z* materials.

High energy neutrons constitute the more penetrating radiation component at accelerators, and usually dominate the field behind the shields.

The photo-neutron source term from EMC on thick targets, in terms of neutrons per unit time and beam power, is given, for different materials as function of electron energy, in Figure 1.8.

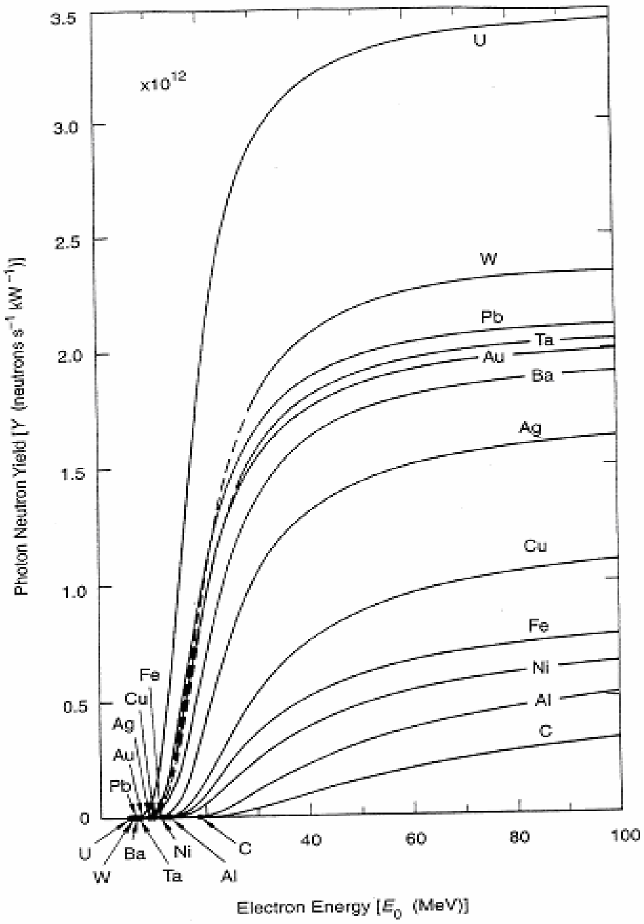

Figure 1.8: Photo-neutron yield of EMC on thick targets. Taken from (NCRP, 2004).

At energies above 100 MeV, the neutron production is energy independent (saturation effect in Fig. 1.8) for medium-high Z materials ($Z > 50$). Lighter materials reach the saturation above 500 MeV. For $E_0 > 200$ MeV, the neutron yield per unit of integrated beam power (neutrons·J^{-1}), Y_n, is approximately given by the following relation (NCRP, 2004):

$$Y_n = 1.21 \cdot 10^8 \cdot Z^{0.66} \qquad (1.12)$$

For light nuclei, such as ^3H, Lithium and Beryllium, equation 1.12 is an underestimation. This occurs also for transuranic elements, due, in this case, to the fact that photo-fissions are not taken into account. The photo-neutrons are produced by three effects: the *giant resonance*, the *pseudo-deuteron* and the *photo-pion* effects.

1.6.1 The giant resonance production

The giant resonance effect is the emission of neutrons by a nucleus which has been excited by the absorption of a photon. Since it is a decay process, the emission is isotropic. The cross section shows a giant resonance, of the order of 0.1 barn, at around 20-23 MeV ($A<40$) or 13-18 MeV ($A>40$). For nuclei with $A>40$ the cross section maximum is roughly located at an energy value of $80\cdot A^{-1/3}$ (MeV). Neutrons from the giant resonance process can be “evaporation” or “direct emission” neutrons. The energy distribution of evaporation neutrons is well described by a Maxwellian function with temperature parameter in the range $0.5 < T < 1.5$ MeV. The average energy, $2T$, which also corresponds to the maximum of the distribution, ranges in $1 < E_{av} < 3$ MeV. Equation 1.13 shows the expression of the fluence energy distribution.

$$\frac{d\phi_n}{dE}\alpha\frac{E}{T^2}\cdot e^{-\frac{E}{T}} \tag{1.13}$$

The giant resonance effect determines the lower energy part of the photo-neutron source term. This process has lower energy threshold and higher cross section than the others, which occur at higher energy. By combining this with the $1/E$ or $1/E^2$ shapes of the photon energy distribution, it is clear that the neutron field is highly dominated by the giant resonance production at any value of initial energy, E_0.

As an example, the neutron spectra from the SLAC accelerator are shown in Figure 1.9.

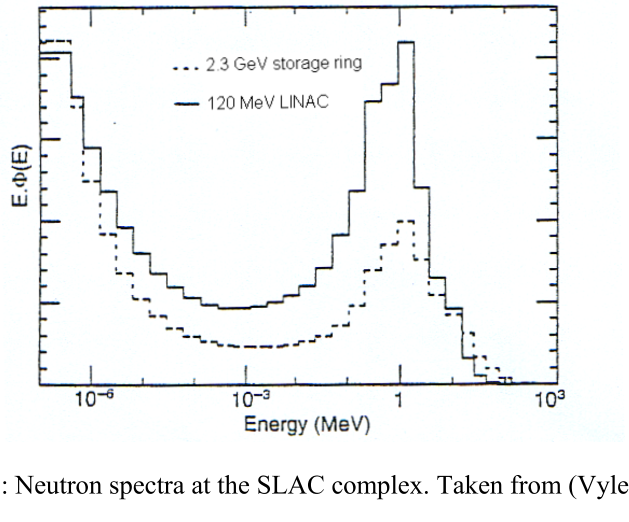

Figure 1.9: Neutron spectra at the SLAC complex. Taken from (Vylet, 1997).

1.6.2 The pseudo-deuteron effect

Whilst the photons in the giant resonance energy range interact with the nucleus as a whole, determining the lower energy part of the neutron spectrum, the higher energy photons (30 - 300 MeV) directly interact with proton-neutron pairs, with a resonance cross section of about 10^{-2} barn, yielding higher energy neutrons (around 100 MeV).

1.6.3 The photo-pion effect

At photon energies above 140 MeV, the pion production effect can occur, with the main resonance, of about 10^{-2} barn, at 300 MeV. The interaction of pions with nuclei generates high energy neutrons, which easily penetrate the shields extracting secondary neutrons and photons. The neutron spectrum within the shields will be therefore dominated by two components: a highly penetrating one, due to the photo-pion effect, and a less penetrating one, locally produced by degradation of the first one.

Vylet (Vylet, 1997) described the energy distribution of the pseudo-deuteron and photo-pion induced neutrons with a $E^{-\alpha}$ high energy "tail", with 5 MeV $< E < E_o/2$ and $1.7 < \alpha < 3.6$ (See Fig. 1.9).

Chapter 2

AMBIENT AND PERSONAL DOSIMETRY FOR RADIATION PROTECTION AROUND HIGH ENERGY ELECTRON ACCELERATORS

2.1 **Limiting and operational quantities**

The International Commission on Radiological Protection, ICRP, in its Publication n. 60 (ICRP, 1991), defined a radiation protection system which has been implemented in almost all national regulations. In this framework, the quantity *Effective Dose*, *E*, is chosen for estimating the risk due to the exposure to ionizing radiations. *E* is therefore a limiting quantity (or protection quantity), i.e. a quantity in terms of which the dose limits for workers and population are defined.

The effective dose is a weighted sum, over different kinds of radiations and different tissues or organs, of the average absorbed doses in the human body.

$$E = \sum_T w_T \sum_R w_R \cdot \overline{D}_{T,R} \qquad (2.1)$$

Where $\overline{D}_{T,R}$ is the average absorbed dose, in a given organ or tissue, *T*, due to a given type of radiation, *R*.

W_R is the radiation weighting factor, reflecting the different probability of health detriment coming from radiations with different LET. The quantity $H_T = W_R \cdot \overline{D}_{T,R}$ is called tissue/organ equivalent dose. The radiation weighting factors are given in Table 1:

Radiation type	Energy range	Radiation weighting factor, w_R
Photons, electrons and muons	all	1
Neutrons	< 10 keV	5
	10 to 100 keV	10
	0.1 to 2 MeV	20
	2 to 20 MeV	10
	> 20 MeV	5
Protons (not recoils protons)	> 2 MeV	5
Alpha, fission fragments and heavy nuclei	all	20

Table 2.1: Radiation weigthing factors recommended in ICRP 60.

Till the 60s, the radiation "effectiveness" was taken into account with the RBE (Parker, 1948), then, from 1964, with the quality factors (ICRP, 1964). One of the main reasons for defining new radiation weighting factor, was the necessity to take into account the higher biological effectiveness of fission neutrons (0.1 – 2 MeV). This resulted in dramatic implications in the neutron metrology and dosimetry.

w_T represents the tissue/organ weighting factor, defined as the risk fraction with respect to the uniform irradiation, i.e. the ratio between the probability of stochastic effects in case of selective irradiation of a given tissue/organ and the probability of stochastic effects in case of whole body irradiation at the same value of equivalent dose. ICRP 60 stated the w_T value for 12 tissues or organs, whilst 10 additional organs are classified as “remainder”. The “remainder” organs have been slightly modified by ICRP Publications n. 69 (ICRP, 1995) and n. 71 (ICRP, 1996).

The effective dose and the equivalent dose to organ/tissue, chosen as limiting quantities, are not measurable, because are defined in the body of each single person. This introduces the necessity of defining new measurable quantities, “operational” quantities, suitable to demonstrate the compliance with the dose limits. The duality can be depicted by the following sentence of R. H. Thomas (Thomas R., 1997):

“Almost without realizing the fact we have slowly slipped into a dichotomy in which protection standards are expressed in ICRP quantities (limiting quantities) *that are not measurable (but may be calculated) and the operational quantities, by which compliance with dose limits may be demonstrated, defined by the ICRU”.*

Among the operational quantities, introduced by the International Commission on Radiation Units and Measurement (ICRU) in Reports n. 39 (ICRU, 1985), n. 43 (ICRU, 1988), n. 47 (ICRU, 1992) and n. 51 (ICRU, 1993), we recall the pe*rsonal and ambient dose equivalent*, for the individual and area monitoring respectively. Such quantities are measurable and traceable to metrology standards, as directly obtainable by multiplying the particle fluence, Φ (for neutrons), or the air kerma, K_a (for photons), by appropriate conversion coefficients. Since the operational quantities provide a conservative estimation of the limiting quantities in almost all irradiation scenarios, they can be used to demonstrate the compliance with the dose limits.

The ambient dose equivalent, $H^*(d)$, *is the dose equivalent that would be produced by the corresponding expanded and aligned field in the ICRU sphere at a depth, d, on the radius opposing the direction of the aligned field*. The unit is J.kg^{-1} and its special name is Sievert (Sv).

The ICRU sphere is centered in the measurement point. The “expanded and aligned field” means a field with the same fluence and energy distribution as the point of measurement, but unidirectional angle distribution (see Figure 2.1). The $H^*(d)$ value, calculated in the point P, is supposed to be representative of the effective dose for the area monitor purposes.

The ICRU sphere is made by the four elements tissue equivalent material (76.2% Oxygen, 10.1% Hydrogen, 11.1% Carbon and 2.6% Nitrogen), with 30 cm diameter and 1000 kg.m^{-3} density. For penetrating radiations as photons and neutrons, the thickness *d* is set to 10 mm.

Albeit the human trunk is more similar to a cylinder, a spherical phantom facilitates the instruments design. Moreover, the dose equivalent at 10 mm is almost phantom shape independent.

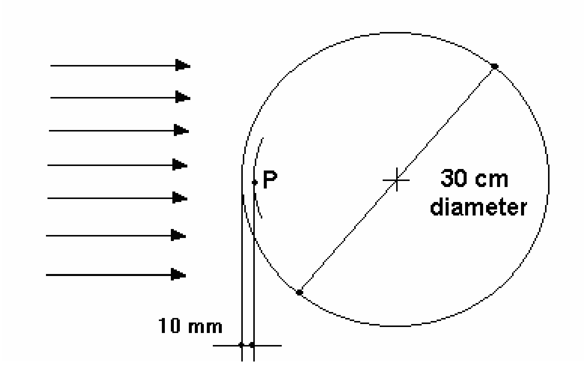

Figure 2.1: The expanded and aligned field and the definition of *H*(d)*, where *d* set to 10 mm for strongly penetrating radiation area monitor purposes.

The *dose equivalent, H,* is calculated by folding the lineal energy distribution of the absorbed dose, $\frac{dD}{dL}$, with the radiation quality factor *Q(L)*, in a specified point in the phantom:

$$H = Q \cdot D = \int Q(L) \cdot \frac{dD}{dL} \cdot dL \qquad (2.2)$$

Q(L) is a function of L (expressed in keV·µm^{-1}) in water. The definition of the quality factor has been revised, by ICRP 60, as follows:

$$Q(L) = \begin{cases} 1 & \text{for } L < 10 \\ 0.32 \cdot L - 2.2 & 10 < L < 100 \\ 300 \cdot L^{-1/2} & L > 100 \end{cases}$$

Convenient conversion coefficients, to be used in practice to calculate the operational quantities from basic physical quantities, were evaluated by a joint ICRP/ICRU group and published in ICRU 57 (ICRU, 1998) and ICRP 74 (ICRP, 1996a). Those coefficients are expressed as dose equivalent per unit fluence (for neutrons) or unit air kerma (photons). Figures 2.2 and 2.3 present the *H*(10)* conversion coefficients, for neutrons and photons, respectively. In the mentioned ICRU/ICRP recommendations, conversion coefficients are reported up to 200 MeV for neutrons and 10 MeV for photons. Data for higher energies are becoming available (Pelliccioni, 2000; *www.lnf.infn.it/services/radiation/conversion_coefficients*), although the adequacy of the current operational quantities, in such energy interval, has been put in doubt (Ferrari, 1995). The concern, especially for photons, is due to the presence of secondary charged particles with higher range than the recommended depth, *d*, which can contribute significantly to organ doses. Thus, the use of conversion coefficients calculated in charged particles equilibrium, could lead to underestimate the risk.

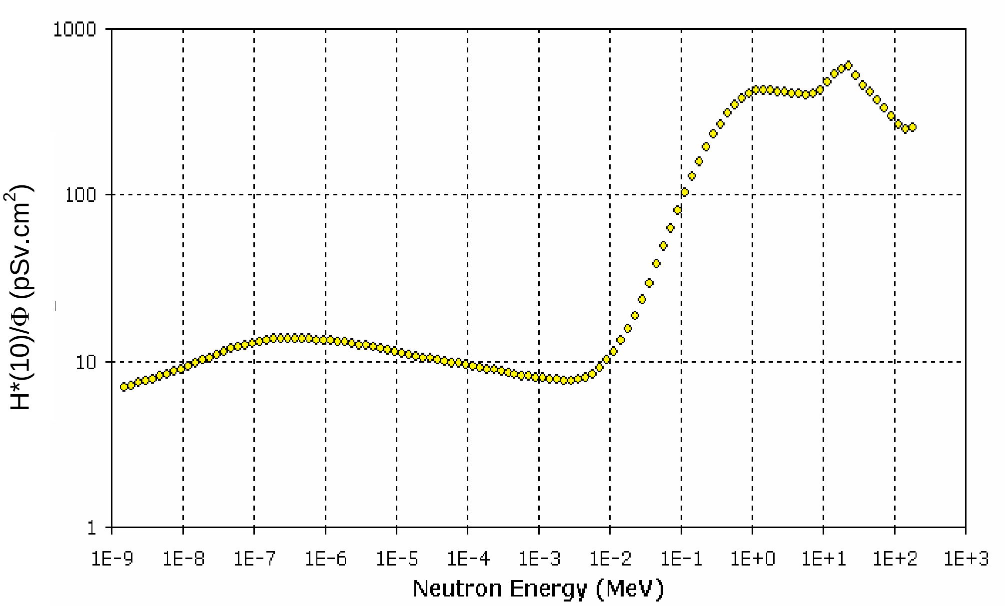

Figure 2.2: Energy dependence of the neutron fluence to ambient dose equivalent conversion factor. Data taken from (ICRP, 1996a).

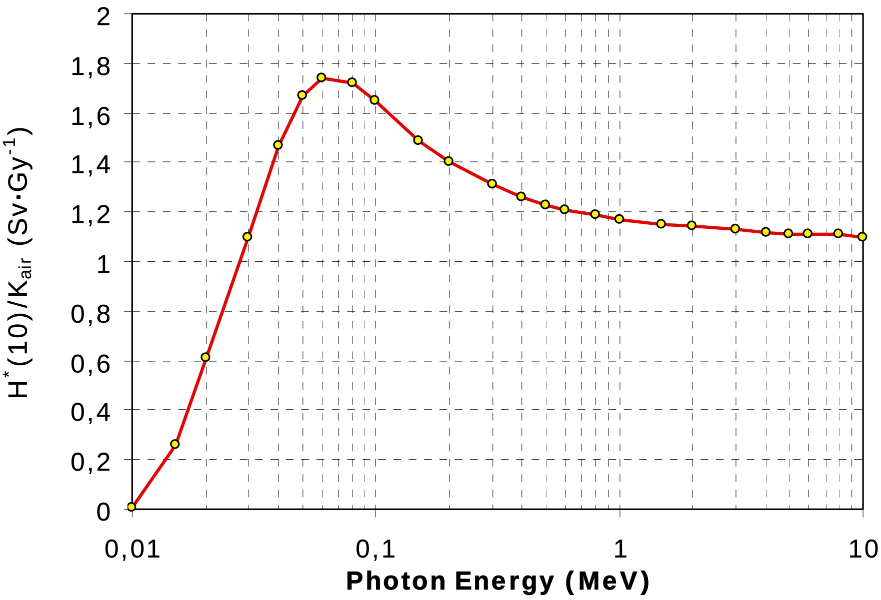

Figure 2.3: Photon air kerma to ambient dose equivalent conversion factor. Data taken from (ICRP, 1996a).

As far as individual monitoring of workers is concerned, the recommended operational quantity is the *personal dose equivalent at a depth d,* $H_p(d)$*,* defined as *the dose equivalent in soft tissue at an appropriate depth, d, below a specified point on the body.* The unit is J.kg^{-1} and its special name is Sievert (Sv).

Unlike $H^*(d)$, the $H_p(d)$ is defined in the body. For strongly penetrating radiation, as photons and neutrons, the depth *d* is set to 10 mm. But, for calculating the conversion factors, a phantom is required. The recommended phantom for calculation is a 30 cm x 30 cm x 15 cm four elements ICRU tissue parallelepiped; whilst the phantom for dosemeters calibration, recommended by ISO, is a water filled 30 cm x 30 cm x 15 cm slab.

Also for $H_p(d)$, the conversion factors for neutrons and photons are specified in ICRU 57 (ICRU, 1998) and ICRP 74 (ICRP, 1996a). Since, from its definition, the $H_p(d)$ value depends on the angle of incidence of the radiation, the conversion coefficients are tabulated as a function of both energy and angle of incidence. Numerical values are omitted here, since this work is mainly focused on area monitor applications.

Operational quantities are suitable for instruments calibration, because a calibration field with known neutron fluence or air kerma, and energy distribution, is also fully characterized in terms of dose equivalent. Area monitors and personal dosemeters should therefore respond in terms of $H^*(d)$ or $H_p(d)$. It should be noticed that, whilst a personal dosemeter is calibrated on a phantom, an area monitor is calibrated in air.

Since the operational quantities are retained to be conservative estimations of the protection quantities in the majority of the irradiation scenarios, the compliance with dose limits can be demonstrated and controlled by using instruments which respond in terms of such quantities.

2.2 Peculiarities of radiation monitoring at high energy accelerators

At high energy electron accelerators, the measurement of operational quantities has to face the following problems:

- the variety of particles: electrons, photons and neutrons. Where neutrons are produced, photons are always present. Also the presence of muons can be of radiological relevance.
- the broad range of energies and angles at which those particles are produced. Whilst the muons production is highly forward peaked, photons and neutrons are more isotropic.
- the time and space distribution of the radiation fields. Active instruments can loose their reliability in presence of pulsed particle fields. Active instruments can be trusted if the count rate is negligible with respect to the repetition rate of the accelerator (NCRP, 2004). If T is the accelerator pulse length and f the pulse frequency, the time between two pulses will be $(f^{-1} - T)$.

Let τ the resolving time of the instrument, with $T < \tau < (f^{-1} - T)$. The true counting rate, n, can be obtained by the apparent count rate, m, as follows:

$$n = f \cdot \ln \frac{f}{f - m} \qquad (2.3)$$

• ICRP 60 has increased the weighting factor for neutrons in the energy range 0.1 - 20 MeV, where the peak of the energy distribution at electron facilities is usually located. This can complicate to demonstrate the compliance with the radiation protection constraints, which are usually a small fraction of the relevant dose limits. As a consequence, very accurate neutron measurements are needed, requiring an accurate knowledge of all factors influencing the response of the instruments, the main of which is the energy distribution of the neutron fluence. The use of neutron spectrometry techniques, in addition to routine survey instruments, is therefore highly recommended.

2.3 Dosimetry of photon radiation

The electromagnetic cascade is mainly constituted by low LET (Linear Energy Transfer) particles, electrons and photons, with energy from zero to the initial accelerator energy, E_0. Since the quality factor, Q, has unity value for such particles, the measurements of a dose equivalent is, in principle, reduced to the measurement of an absorbed dose.

Common area monitors and personal dosemeters can be adopted, but their results must be interpreted with care (Hoefert, 1980), due to the following reasons:

· pulsed fields can heavily affect the reading of active monitors. In special cases, the correction factor is known (see 2.2);

· the energy and angle dependence of the response of the instruments, in addition to the wide energy range of the photon field, can lead to over- or under-estimate the doses;

· although the instruments should be used to assess the operational quantities, most of them have been designed to respond in terms of *air kerma*. The energy dependence of the *air kerma* to operational quantities conversion coefficients can also lead to systematic errors in the measurements;

· because photons at high energy electron accelerators are always mixed with neutrons, it is always recommended to characterize a measurement point with two instruments, one for photons and one for neutrons. Moreover, the knowledge of the neutron sensitivity of the photon instrument, as well as the photon sensitivity of the neutron meter, is very important to interpret and/or correct the measurement.

The following photon instruments are commonly used around accelerators: ionization chambers, Geiger-Mueller counters and Thermoluminescence dosemeters (TLDs).

Ionization chambers: the dose equivalent in a mixed field, with variable composition of low LET (photons and muons) and high LET particles (neutrons), can be estimated with a single instrument, as follows:

$$H = \overline{Q} \cdot D \qquad (2.4)$$

Where D represents the absorbed dose, and $\overline{Q}$ the average quality factor of the field, to be measured with a LET spectrometer. In absence of this information, a conservative $\overline{Q}$ value may be applied, with a considerable increase in the uncertainty. $\overline{Q}$ can be conservatively estimated as 10, even if in most real situations it ranges from 1 to 6 (NCRP, 2004).
Because the chamber walls and filling gas can be sensitive to neutrons, tissue equivalent proportional counters are frequently preferred.

Geiger-Mueller counters are used for immediate operational evaluations, such as the identification of areas with high residual activity. Because of the dead time related problems, dosimetric evaluations are only allowed in low dose rate areas.
Nevertheless, small volume photon counters with low neutron sensitivity and reasonable flat energy response have been developed (Wagner, 1961).

Thermoluminescence dosemeters (TLDs) are widely employed, due to various advantages:
· the response is dose rate independent, so the use in pulsed fields is possible;
· ^{7}Li enriched detectors are almost insensitive to neutrons;
· TLDs can be spatially arranged around complex devices, such as klystron or bending magnets, in order to identify leakage points;
· TLDs are often used to carry out accurate ambient dose maps around the installation;
· combinations of multiple TLDs, adequately filtered, can be studied in order to assembly personal dosemeters with flat energy response in terms of $H_p(10)$;
· because of their small size, TLDs are suitable for low penetrating radiations, such as beta (Bedogni, 2001). This is often applied for the extremity monitoring during the manipulation of activated materials, where the $H_p(0.07)$ due to beta radiation can be even a factor of ten higher than the $H_p(10)$ due to photons.

2.4 **Dosimetry of neutron radiation: the need for spectrometric techniques**

The dosimetry of neutron radiation is one of the most complicated tasks in radiation protection. This arises from several factors, related to either the definition of the operational quantities, or the practical problems in the instrument design and calibration.

Although the ICRU operational quantities were designed to give a conservative estimate of the limiting quantities, for some neutron energies and irradiation geometries there is a significant divergence, which could lead to a relevant over- or under-estimation of the risk. Consequently, spectrometric information is needed in situations where the operational quantities approach or exceed the limits.

Figure 2.4 shows the energy dependence of the ratio between the ambient dose equivalent, *H*(10)*, and the Effective dose, *E*, in three different irradiation geometries.

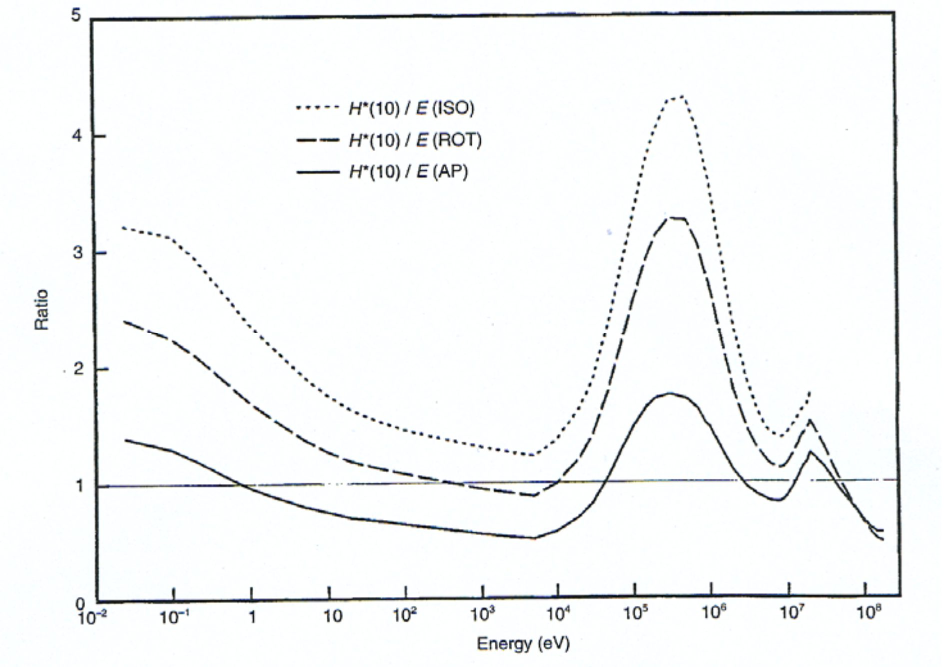

Figure 2.4: Energy dependence of the *E/H*(10)* ratio in three different irradiation geometries: anterior to posterior (AP), rotational (ROT) and isotropic (ISO). Taken from (Bartlett, 2003).

As far as the measurement aspects are concerned, the impossibility to design instruments with accurate *H*(10)* or $H_p(10)$ response at all energies and irradiation angles is the major problem (ICRU, 2001). This arises from the fact that the neutron interaction mechanisms in the dosemeter are different than in the human body. A neutron in tissue induces a complex secondary charged particles field, which is difficult to simulate with a personal dosemeter. The situation is even more complex if the neutron energy ranges from thermal (10^{-8} MeV) to hundreds of MeV. Since the detection mechanisms are very different than the processes of energy deposition in tissue, the dose equivalent responses of personal and area dosemeters have prominent energy dependence.

Designing accurate neutron instruments is also made difficult by the dramatic dependence of the fluence-to-dose-equivalent conversion coefficients, which vary of a factor 40 as the energy changes from 1 keV to 1 MeV. This partially reflects the behavior of the neutron weighting factor, w_R (see 2.1), which shows a peak in the range 0.1 – 20 MeV.

Instruments with reasonably flat dose equivalent response have been developed, but only within a restricted energy sub-interval. Commonly employed area monitors, such as rem counters with spherical (Leake type) or cylindrical (Anderson-Braun type) moderator, or tissue equivalent proportional counters (TEPC), show satisfactory energy response in the MeV region (which usually corresponds to the energy of the calibration sources), but their performances in the intermediate neutrons region are very poor.

To improve the response of rem counters at energies above 20 MeV, a lead shell of one centimeter has been included in the moderator. This enhances the instrument response because it extracts secondary neutrons via (n, xn) reactions. This principle, initially introduced at INFN-Frascati with the LINUS counter, has been widely applied (Birattari, 1990; Birattari, 1998).

Figure 2.5 compares the *H*(10)* /Φ coefficient with the fluence response of a commercial rem counter with spherical moderator (Burgkhardt, 1997), as a function of the neutron energy.

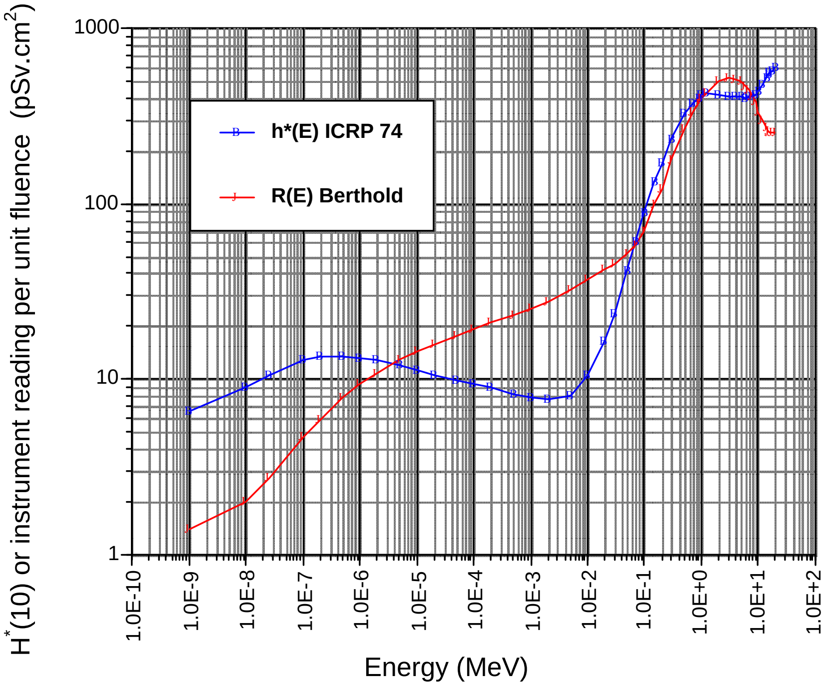

Fig. 2.5: Energy dependence of the *H*(10)/ϕ* coefficient compared with the fluence response of a Berthold LB6411 rem counter. Data taken from (Burgkhardt, 1997).

The suitability of a given instrument in a specific environment should be, therefore, evaluated by comparing the workplace neutron spectrum with the energy response of the device, thus requiring spectrometric information.

Another critical aspect in neutron dosimetry is the calibration: instruments must respond over a wide energy range to cover the entire energy range of the workplace neutron spectra. Since the energy dependence of the instruments is usually relevant, significant over/under estimation of the dose equivalent (McDonald, 2001) can occur, if an instrument is used in a workplace field with different energy distribution than the calibration field. Moreover, only one facility adequately equipped with ISO reference fields (ISO, 1998; ISO, 2000; ISO, 2001) is available in Italy (Bedogni, 2002), and only a limited number can be found within Europe. The characteristics of the ISO reference fields produced by radioisotopic sources (continuous spectra) are reported in Table 2.2.

Moreover, thermal neutrons (2.53E-8 MeV) and quasi mono-energetic beams (0.002, 0.024, 0.144, 0.25, 0.565, 1.2, 2.5, 2.8, 5, 14.8 and 19 MeV) have been standardized (ISO, 2001) for instrument calibration purposes.

Source	Type	$T_{1/2}$ (years)	Specific neutron yield	E_ϕ [2] (MeV)	E_H [3] (MeV)	h^*_ϕ [4] (pSv cm^2)
^{241}Am-Be	(α, n)	432	6.6E-5 s^{-1} Bq^{-1}	4.16	4.4	391
^{241}Am-B	(α, n)	432	1.6E-5 s^{-1} Bq^{-1}	2.72	2.8	408
^{252}Cf	fission	2.65	2.4E+15 s^{-1} kg^{-1}	2.13	2.4	385
^{252}Cf(D$_2$O) [1]	fission	2.65	2.1E+15 s^{-1} kg^{-1}	0.55	2.1	105

Table 2.2: Characteristics of the ISO radioisotope reference fields.

[1] The ^{252}Cf source is placed at the center of a heavy-water sphere with a diameter of 300 mm, covered with a cadmium shell of thickness approximately 1 mm. Of the source neutrons, 11.5 % are moderated below the cadmium cut-off and captured in the cadmium shell.

[2] E_ϕ is the fluence averaged neutron energy

[3] E_H is the dose equivalent averaged neutron energy.

[4] h^*_ϕ is the fluence averaged fluence-to-ambient dose equivalent conversion factor.

Since all ISO reference fields are below 20 MeV, the high energy accelerators field is not covered. A simulated workplace of high energy neutrons may be developed for calibration purposes, as indicated in the Standard ISO 12789 (ISO 2001a). The main requirements for the qualification of a simulated workplace are the repeatability of the irradiation conditions, which is not trivial in a complex environment such as a reactor or an accelerator, and the knowledge of the field by means of spectrometric measurements and/or calculations. The reliability of the spectrometer should be ensured by calibration and validation against nationally or internationally recognized metrological standards. As an example, the high energy calibration facility CERF (Birattari, 1998a) has been created at CERN. At CERF, high energy radiation fields are produced to simulate the workplace spectra encountered at high energy accelerators or the cosmic rays field.

From the above mentioned factors, it follows that neutron spectrometry techniques are of great importance in neutron dosimetry. If reliable spectrometric measurements are available, the *H*(10)* value may be derived with the following relation:

$$H^*(10) = \int_{E\min}^{E\max} dE \cdot \Phi(E) \cdot h^*_\phi(E) \qquad (2.5)$$

where $\Phi(E)$ is the fluence energy distribution and $h^{*}_{\phi}(E)$ the fluence to ambient dose equivalent conversion coefficient. If the angular distribution of the field is also known, the personal dose equivalent can be determined. In crucial situations, i.e. near the limits, even the effective dose could be, in principle, calculated. In absence of angular information, estimations for $H_p(10)$ and E can be provided, referring to a conservative irradiation geometry, usually the AP one.

In routine measurements, where the doses are low and the need for very accurate measurements is not so stringent, rough spectrometric information could be enough for dosimetry purposes. Anyway, due to the increasing need to keep doses as low as possible, and in order to demonstrate the compliance with non-relevance criteria and best practice requirements, reliable spectrometric techniques are highly recommended also in the routine radiation protection practices.

2.5 Current techniques for neutron dosimetry

Due to the limitations in the dose equivalent response of almost all dosemeters, as shown in 2.4, the following general requirements should be taken into account in neutron radiation protection dosimetry:

· calibration in a reference field with similar energy distribution as the workplace field;
· knowledge of the energy dependence of the dose equivalent response of the dosemeter;
· knowledge of the energy distribution of the workplace field;
· determination of a workplace specific calibration factor.

In addition to the above mentioned conditions, the neutron dosemeters to be used at high energy electron accelerators should have adequate sensitivity in the 0.1 – 10 MeV interval, where the workplace spectra usually show a maximum. Moreover, this range also corresponds to the maximum value of w_R and the interval where the fluence to dose equivalent conversion coefficients show the maximum variability.

Thermoluminescence dosemeters: as shown in 2.3, TLDs are widely employed, mainly due to their capability to discriminate thermal neutrons to photons. This is done by using ^{6}LiF and ^{7}LiF based paired detectors. Moreover, recently developed ^{6}LiF based materials (*www.tld.com.pl/mcpns.html*) with high thermal neutron to photons sensitivity ratio and high absolute neutron sensitivity, makes this technique highly promising for low dose rate measurements (Bedogni, 2006; Bedogni, 2006a). Moreover, TLDs are not affected by RF noise and pulsed fields.

Since TLDs are insensitive to fast and intermediate neutrons, suitable area or personal dosemeters can be obtained relying on moderated configurations. This is usually done by placing the detectors inside polyethylene cylinder or spheres (as area dosemeter), or into albedo

personal dosemeters (Budzanowski, 1995).
Since the TLD response is known to be LET dependent (Spurny, 2004), TLD based methods have been developed to evaluate the mean quality factor in mixed fields (Hajek, 2002).

Activation detectors: the use of activation reactions is of interest, especially in high intensity fields (Thomas D. J., 2002; Gualdrini, 2004) or for criticality dosimetry (Gualdrini, 2004a). The materials have to be chosen with care and provided in high purity standards, since the competing reactions can lead to mis-interpret the readings. Corrections have to be applied to take into account the irradiation time, the post irradiation delay and the measurement time. The following reactions have been used:

· $^{197}Au(n,\gamma)^{198}Au$ ($T_{½}$=2.7 d) or $^{115}In(n,\gamma)^{116}In$ (54.2 min) for thermal neutrons;
· $^{32}S(n,p)^{32}P$ (14.3 d), threshold at 3.2 MeV;
· $^{27}Al(n,\alpha)^{24}Na$ (15 h), threshold at 6 MeV;
· $^{12}C(n,2n)^{11}C$ (20.4 min), threshold at 20 MeV;
· $^{27}Al(n, 2p4n)^{22}Na$ (2.6 y), threshold at 25 MeV;
· $^{12}C(n,spall)^{7}Be$ (53 d), threshold at around 30 MeV.

Also fission reactions on bismuth, thorium and uranium have been used. Moreover, minimum detectable doses lower than 100 μSv can be achieved by the combination of fissile radiators to and track-etch detectors, such as polycarbonate (Griffith, 1990).

Track-Etch detectors: This technique has various advantages, such as the insensitivity to photon radiation and the high sensitivity to fast neutrons. A minimum detectable doses of 100-200 μSv can be achieved. Moreover, the low cost make the track-etch dosemeters attractive for routine personal dosimetry. Different track detectors, etched chemically or electro-chemically, have been successfully employed in neutron dosimetry: cellulose nitrate, Lexan, polycarbonate and, mostly used, the CR-39® (Griffith, 1990).
The Chemically etched (CE) CR-39 shows an energy threshold of about 0.1 MeV (which decreases to about 0.05 MeV in the electrochemical etching, ECE) and a typical energy dependence of ±40% in the energy interval 0.5 – 14 MeV. Taking advantage of image processing algorithms, based on the area distribution of the tracks, it is possible to perform a rough spectrometry, resulting in a reduction of such dependence to ± 15% (Bedogni, 2002a). Nylon converters have been successfully used to enhance the response to thermal and intermediate energy neutrons, obtaining an energy dependence of the response of ± 14% in the range from thermal to ^{241}Am-Be neutrons. (García, 2005). For high energy neutrons, the detectors can be combined with (n, xn) converters or fission radiators. Various automatic CR-39 readers, based on slide scanners (Gilvin, 2001) or dedicated motion/vision systems (Bedogni,

2003) have been developed for the needs of routine dosimetry services. Moreover, accurate material selection protocols have been developed, in order to optimize the measurement reproducibility and lower the minimum detectable dose (Fantuzzi, 2002).

2.6 Neutron spectrometry: an overview

Since the discovery of neutrons by Chadwick (1932), many methods for measuring the energy distribution of the neutrons have been developed. Before 1960 the following spectrometers techniques were already in use (Brooks, 2002): nuclear emulsions, proportional counters, cloud chambers, organic scintillators and recoil telescopes. ^{3}He proportional counters and ^{6}LiI(Eu) scintillators, where the energy of the charged particles produced by nuclear reactions was measured, were also used. In the same period the time-of-flight and the activation foils techniques were also known.
A crucial development occurred in 1960 with the introduction of the multi-sphere spectrometer (Bramblett, 1960) (also called Bonner Sphere Spectrometer, BSS), based on a thermal neutron sensor placed at the centre of polyethylene spheres of different diameters (up to 18”). Iterative unfolding codes were introduced, allowing inferring the neutron spectrum on the basis of the readings of the different spheres. Semiconductor based spectrometers were introduced in 1963, and superheated drop detectors were firstly used by Apfel in 1979. Since the 80s, computer based techniques became essential for neutron spectrometry: Monte Carlo codes were used to generate the response functions of the detectors, and iterative algorithms were applied to unfold the neutron spectra from the spectrometer readings.

At present the following techniques, other than the BSS, are widely used:

Recoil nuclei spectrometry: these spectrometers register the pulse height spectrum of the neutron induced recoil products at all angles or at a given angle (recoil telescopes). The typical energy range for proportional counter based devices is 0.05 – 4 MeV; the typical energy resolution of the pulse height is 10% for 1 MeV neutrons. Better performance in terms of energy range (up to 200 MeV) can be achieved with telescope detectors or organic scintillator based instruments. Reviews of the proportional counter or liquid scintillator based spectrometers are given in (Tagziria, 2003) and (Klein, 2003).

Nuclear reaction based spectrometers: they rely on the measurement of the pulse height spectrum of the charged particles produced by neutron induced nuclear reactions (exothermic or endothermic). The reactions are ^{3}He(n,p)^{3}H (Q=0.764 MeV), ^{6}Li(n,α)^{3}H (Q=4.786 MeV), ^{10}B(n,α)^{7}Li (Q= 2.792 MeV), ^{12}C(n,α)^{9}Be (Q= -5.70 MeV) and ^{28}Si(n,α)^{25}Mg (Q = -1.65 MeV). The most popular reaction is the ^{3}He(n,p)^{3}H, which allows to cover the energy range 0.05 – 5 MeV with typical resolution of 15-40 keV.

Time-of-flight methods: (Elevant, 2002) this relies on the measurement of the time spent by neutrons to travel a given distance. Whist the “arrival” signal is given by a scintillator detector, two methods are used to give the “start” signal: the scattering in a first scintillator, or the detection of an associated particle or photon. The typical energy range is 1 - 15 MeV, with resolution of 5% at 2.5 MeV.

Threshold detectors spectrometers: an appropriate set of nuclear reactions with well known threshold energy can constitute a neutron spectrometry. The activation foils technique (Gualdrini, 2004a) and the superheated drop detectors spectrometry (d’Errico, 2003) are based on this principle.

2.7 **Bonner Spheres Spectrometers**

2.7.1 *Overview*

The Bonner Sphere Spectrometer (BSS) has been widely applied for more than 40 years in the field of neutron dosimetry and spectrometry. The isotropy of the response, the wide energy range (from thermal to GeV neutrons) and the easy operation make these systems still useful (Thomas D. J., 2002a). The reason for measuring moderated neutrons with a thermal neutron sensor is the availability of high sensitivity thermal neutron detectors with good gamma rays rejection. The direct detection of fast neutrons is much more complex and occurs at considerably lower values of cross sections. For the same reason, moderation based instruments such as long counter and rem counters have been developed. On the other hand, an experimental difficulty of large diameter moderated instruments is the uniform irradiation condition, under which the response functions are calculated. This condition can be fulfilled with point sources at large distances. In collimated beam accelerators, it is usually difficult to reach this condition, especially for the large sphere sizes.

The neutron moderation process within the Bonner Spheres (BS) is mainly due to elastic scattering, H(n,n)H and C(n,n)C, at energy lower than 4 MeV. At higher energies, the threshold reactions C(n,n’3γ) (threshold $\approx$ 5 MeV), C(n, α) (7 MeV), C(n,n’3α) (8 MeV), C(n,p) (15 MeV), C(n,n’p) (15.5 MeV), C(n,p) (18 MeV) become also important (Alevra, 2003).

A suitable set of polyethylene spheres of different diameter makes it possible to obtain spectral information over the desired neutron energy range. The response function of a given sphere, usually generated with Monte Carlo codes and available in literature (IAEA, 2001), shows a peak at a well determined energy, which corresponds to those neutrons that are better thermalized by the sphere. Lower energy neutrons are captured by the polyethylene (giving 2.2 MeV gamma rays), whilst higher energy neutrons escape from the assembly. The peak energy, uniquely related to the sphere diameter, increases as the sphere diameter increases. The Bonner spheres are usually identified by their diameter expressed in inches. Figure 2.7 shows, as an example, the response function of a 8” polyethylene (density 0.95 g·cm^{-3}) sphere using a cylindrical 4 mm x 4 mm ^{6}LiI(Eu) scintillator, as the one proposed by Bonner in 1960, and adopted in this work.

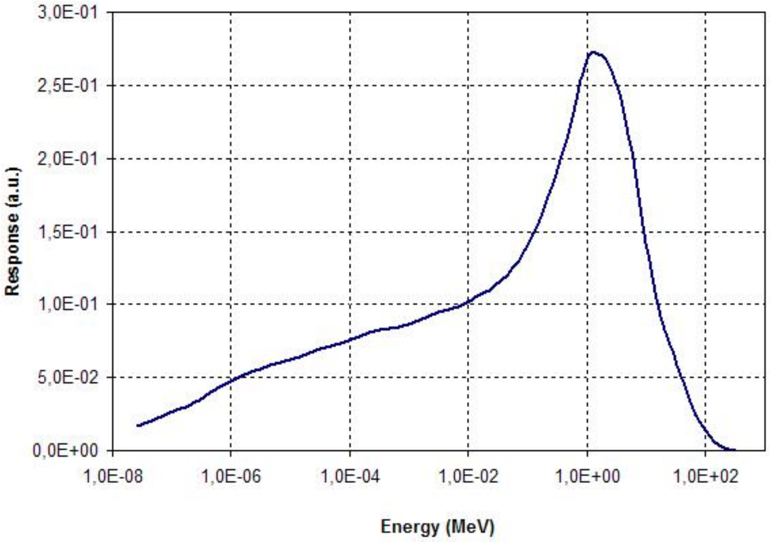

Figure 2.6: Response function of a cylindrical 4 mm x 4 mm ^{6}LiI(Eu) scintillator at the center of a 8” polyethylene (density 0.95 g·cm^{-3}) sphere. Data taken from (IAEA, 1990).

The polyethylene sphere diameter usually ranges up to 12”, covering the energy range from thermal to 20-30 MeV neutrons. Well documented BSSs in this energy range are in use in Europe, namely:

· PTB, Braunschweig (D): the PTB “C” set has 14 configurations: bare, bare+Cd, 3”, 3.5”, 4”, 4.5”, 5”, 6”, 7”, 8”, 10”, 12”, 15” and 18” (Alevra, 2002).

· Universidád Autónoma de Barcelona, Spain: 11 configurations: 2.5”, 3”, 4.2”, 5”, 6”, 8”, 10”, 12”, 2.5” + 1 mm Cd, 3” + 1 mm Cd, 4.2” + 1 mm Cd (Lacoste, 2004).

· IRSN Cadarache, (F): 13 configurations: 0”, 2.5”, 3”, 3.5”, 4.2”, 5”, 6”, 7”, 8”, 9”, 10”, 11” and 12”. A 1 mm thick cadmium shield can be used with the five smaller spheres (Lacoste, 2004).

· NPL (UK): 11 configurations: bare, 2”, 2.5”, 3”, 3.5”, 4”, 5”, 6”, 8”, 10” and 12” (Thomas D. J., 2002).

The INFN Frascati National Laboratory has initially adopted the commercial set from Ludlum, equipped with six spheres: 2”, 3”, 5”, 8”, 10” and 12”.

Due to the need to perform neutron spectrometry at high energy particle accelerators or in cosmic rays fields, some laboratories have added new spheres, equipped with internal metal shells, to extend the energy range to GeV neutrons. The metal layers act as (n, xn) converters, as first suggested for the LINUS counter (Birattari, 1990; Birattari, 1998). PTB has added four polyethylene spheres (maximum diameter 8”) with copper and lead inlets, to the “C” set, augmenting the energy range up to 10 GeV. The resulting system, NEMUS (Wiegel, 2002), has been used to measure the neutron component of the cosmic rays at flight altitudes and at ground level (Wiegel, 2002a).

For the high energy electron accelerators, Vylet introduced a 12” sphere with an internal 1 cm lead layer (Vylet, 1997). The same approach has been followed by INFN. The characterization of the complete INFN system for use in high energy electron accelerator is a part of this work.

2.7.2 *The response of a BSS*

Since each polyethylene sphere has a unique energy response function, the neutron spectrum can be inferred, from the readings of the *m* spheres, by inverting the Fredholm integral (unfolding procedure):

$$C_i = \int dE \cdot R_i(E) \cdot \frac{d\Phi}{dE} \qquad \text{i = 1,..,m} \qquad (2.6)$$

Where C_i represents the count rate of the ith sphere (measured in counts per second, s^{-1}), $R_i(E)$ the energy response function (cm^2) of the thermal neutron sensor at the center of the ith sphere and $\frac{d\Phi}{dE}$ the energy distribution of the neutron fluence (cm^{-2}·MeV^{-1}). Good approximation of the $R_i(E)$ functions can be obtained with Monte Carlo calculations. Their validation should be done taking advantage on measurements with well characterized radionuclide neutron sources and monochromatic neutron beams. Since the $R_i(E)$ are calculated as discrete functions, the problem should be solved in the discrete version:

$$C_i = f \cdot \sum_{j=1}^{N_g} R^*_{ij} \cdot \Phi_j \cdot \Delta E_j \qquad (2.7)$$

Where R^*_{ij} is the response function (simulated with Monte Carlo codes or taken from literature) of the i-th sphere averaged on the energy interval ΔE_j. The whole energy range has been divided in N_g groups, usually equi-lethargic. Φ_j is the neutron fluence (cm^{-2}) in the energy interval ΔE_j and f represents the spectrometer calibration factor, which takes into account the efficiency of the specific thermal sensor employed. f has to be determined with a calibration in a reference neutron field.

Since $\frac{d\Phi}{dE}$ can be written as $\Phi\cdot\frac{d\varphi}{dE}$, where Φ is the total neutron fluence (cm^{-2}) and $\frac{d\varphi}{dE}$ its energy distribution normalized to the unity, in analogy Φ_j can be written as $\Phi\cdot\varphi_j$, where φ_j is the discrete version of $\frac{d\varphi}{dE}$. Therefore the equation (2.7) is equivalent to

$$C_i = f \cdot \Phi \cdot \sum_{j=1}^{N_g} R^*_{ij} \cdot \varphi_j \cdot \Delta E_j \qquad (2.8)$$

The unfolding procedure, required to invert the equation (2.8) to obtain the neutron spectrum from the sphere readings, will be discussed in detail in Chapters 6 and 7.

2.7.3 *Selecting the central thermal neutron sensor*

Various thermal neutron sensors have been used at the centre of the BSS, in order to adapt the system to different operative needs. Designed to be used with a cylindrical 4 mm x 4 mm scintillator LiI(Eu), the BSS has been employed with various active and passive detectors. Active detectors, due to their high sensitivity, are usually employed at low intensity fields. On the other hand, their use in pulsed fields, or in presence of electromagnetic noise, can lead to distorted results. Another drawback is the sensitivity to gamma radiation, which limits their use in high gamma background scenarios. The following active sensors are often used:

The cylindrical 4 mm x *4 mm* ^{6}*LiI(Eu) scintillator*: used in the original Bonner system, the LiI(Eu) scintillator is supplied with the commercial Ludlum BSS. The high capture cross section of the ^{6}Li (940 barn at 0.025 eV) together with the high density of the LiI, result in a very good thermal neutron efficiency. Moreover, the small dimension of this detector allows employing it with very small spheres, such as 2”, 2.5” and 3”.

On the other hand, the high density and high atomic number of iodine make this detector sensitive to photons too. The ^{6}Li(n,α)T neutron capture reaction shares the Q value of 4.78 MeV between the triton and the alpha. The absorption of such energy produces a Gaussian shaped peak in the pulse height spectrum, which in general is superposed to a continuous, exponentially decreasing, photon background. Since the separation of the neutron to photon events is the main problem of LiI detector, a detailed knowledge of its gamma sensitivity becomes essential.

A reliable version of the response functions of this detector in the Ludlum 0.95 g.cm^{-3} spheres has been derived with MCNP ver. 4 by Mares and Schraube (Mares, 1994).

This system has been recently used at SLAC (Vylet, 2002), at the Georgia Institute of Technology (Veinot, 1998), in Mexico (Vega-Carrillo, 2004) and in Spain (Barquero, 2005).

^{3}*He filled proportional counters*: In order to provide a small thermal sensor with reduced gamma sensitivity, a 8 kPa ^{3}He 10 mm x 9 mm cylindrical proportional counter, type 05NH1 (Eurisys, 1999), was developed in the 80s and it is currently used by many groups, as the Radiation Physics Group of the UAB and the IRSN (France) (Lacoste, 2004). Its response is almost twice than the 4 mm x 4 mm ^{6}LiI(Eu).

One of the most popular detectors is the spherical SP9 counter by Centronic Ltd., UK. Compared with the 05NH1 counter, the thermal sensitivity is around a factor five higher. On the other hand, the large diameter (3.2 cm) impedes the use of small spheres such as the 2”. The SP9 counter has been extensively used by the PTB (Alevra, 2003) and transferred from PTB to other laboratories (Alevra, 2002).

For high energy neutron fields around charged particle accelerators, Vylet (Vylet, 2002) has used a 12.7 x 12.7 cm^2 organic scintillator, which is very convenient in the energy region above 20 MeV, due to the activation of the carbon ^{12}C(n,2n)^{11}C, characterized by a threshold at 18 MeV.

Passive detectors: Since active detectors can fail in scenarios characterized by pulsed fields, high electromagnetic noise and high photon background, various passive detectors have been developed in order to overcome these difficulties. BSSs have been frequently used with TLD pairs (Vega-Carrillo, 2002) or activation detectors, such as gold foils (Thomas D. J., 2002). The main disadvantage of passive detectors is their low sensitivity, but they can be exposed for long time and don't need electric supply. Moreover, high sensitivity TLD materials with interesting neutron to gamma discrimination capability are becoming commercially available (Bedogni, 2006a) and have been recently investigated for their use inside BSS (Bedogni, 2006).

2.7.4 *Influence of the polyethylene density on the BSS response functions*

The diameter and the density of the spheres can constitute sources of discrepancy between the experimental and the calculated response functions of a BSS. Such parameters should be carefully verified, especially if the spheres are fabricated by a non specialized manufacturer. Data from Thomas (Thomas D. J., 1992) show that the relative change in the sphere response due to 1% change in the polyethylene density, $(dR/R)/(d\rho/\rho)$, is a function of the neutron energy and the sphere diameter. Such parameter, which can be as high as 6, is more important in energy regions where the sphere response is poor. The response function of a given sphere can be corrected for a density change, by attributing to the sphere a different diameter than the real one, according to the following relation (Alevra, 2003):

$$R(D,E,\rho \pm \Delta\rho) = R(D \pm \Delta D, E, \rho) \quad with \left(\frac{\Delta D}{D}\right)_{\rho} = \left(\frac{\Delta\rho}{\rho}\right)_{D} \qquad (2.9)$$

Thus, differences in sphere diameter or polyethylene density could be corrected, provided there is a method to calculate the response function of a sphere with diameter *D+ΔD,* by perturbing the response function of a sphere with diameter *D*. Interpolation methods are suggested in (Mares, 1994) and (Wiegel, 1994).

Chapter 3

THE BONNER SPHERE SPECTROMETER USED AT THE INFN FRASCATI NATIONAL LABORATORIES

3.1 **Overview**

The BSS in use at the LNF is based on the commercially available Ludlum system (Model 42-5 Neutron Ball Cart). The central detector is a LiI(Eu) (96% ^{6}Li enrichment) cylindrical 4 mm x 4 mm scintillator, connected through a Plexiglas light pipe to a magnetically shielded photomultiplier. The pulse spectrum is collected by a control unit (Model 2350-1 data logger) which also separates the gamma background from the neutron induced events. The detector and the data logger system is controlled by a portable PC through a serial port.

The data logger unit counts the events only above a fixed threshold. The operation parameters provided in the *certificate of calibration*, have been optimized and measured from the manufacturer:

- photomultiplier operating voltage = 525 V;
- pulse height threshold = 10 mV;
- detector dead time = 5 μs.

All counting parameters can be modified or controlled via computer.

The detector can operate in either rate-meter or integration modes. For the purposes of this work, only the integration mode will be adopted. The detector and its aluminum holder are shown in Figure 3.1.

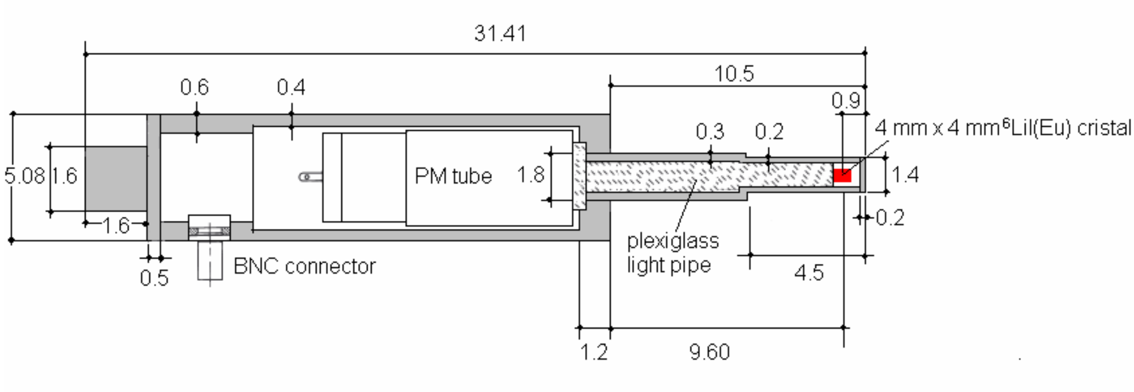

Figure 3.1: The 4 mm x 4 mm LiI(Eu) scintillator and the aluminium holder. All measures are in cm (data provided from the manufacturer).

In its original version, the system was equipped with six spheres: 2”, 3”, 5”, 8”, 10” and 12”. The polyethylene density is 0.950 ± 0.001 g.cm^{-3}. In order to adapt the system to high energy neutron fields, an additional 12” sphere with an inner 1 cm Pb layer was specially manufactured. Figures 3.2 and 3.3 show the Bonner Spheres set with the control unit and the new lead loaded sphere. To transport the BSS and perform the irradiations in reproducible geometry condition, a mobile unit is used, as shown in Figure 3.4.

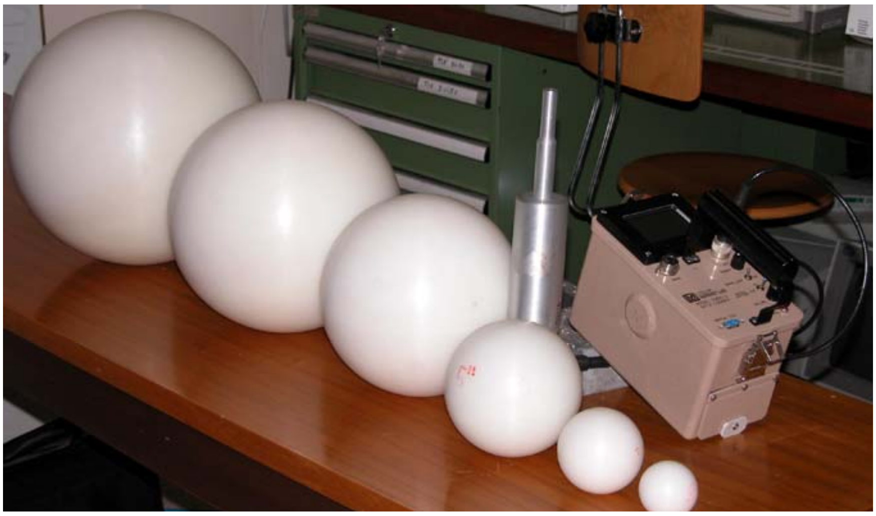

Figure 3.2: The LNF BS set with the detector part and the control unit.

Figure 3.3: The 12” sphere with the 1 cm lead insert. The lead shield, formed by two half shells, is placed around an inner 3” polyethylene sphere which is held by a polyethylene cylinder.

Figure 3.4: The mobile unit used to transport the spheres and perform the irradiations in reproducible geometry.

3.2 Discrimination of the photon background

As indicated in 2.7.3, the 4 mm x 4 mm ^{6}LiI(Eu) cylindrical scintillator shows a high thermal neutron efficiency, due to the high neutron capture cross section of ^{6}Li and the high mass density of the LiI. Unfortunately, the detector is also sensitive to photons, due the high density and the high atomic number of iodine. This could significantly perturb the results, especially if the photon field has high intensity and the photon energy is high enough to produce pulses in the 4.78 MeV region, where the neutron peak arises. In addition, it isn't possible to extract a pulse height spectrum from the 2350-1 data logger unit. For these reasons, the knowledge of the photon sensitivity of the system becomes crucial.

This parameter for the LNF spectrometer has been experimentally determined using reference photon fields of ^{137}Cs and ^{60}Co at the LNF Secondary Standard Calibration Laboratory and the ENEA Radiation Protection Institute, Bologna.

The LNF and the ENEA photon facilities (Figure 3.5), consist of remotely controlled irradiators (single-source or multi-source) with collimated fields. The photon kerma rate values along the optical bench have been determined with reference ion chambers and are traceable to the Italian Primary Metrology Institute (INMRI, ENEA Casaccia - Rome).

Whilst the LNF facility can produce low kerma rate photon fields (10^{-3} to 10^{-1} mGy/minute), the ENEA facility has been used to test the spectrometer at medium-high kerma rate values (1 to 30 mGy/minute).

Figure 3.5: The LNF spectrometer being exposed in the gamma irradiation unit of the LNF (left) and ENEA (right) Secondary Standard Calibration Laboratories.

The photon sensitivity of the spectrometer is expected to be a function of the photon energy, the kerma rate and the sphere diameter. Namely, the response should increase as the kerma rate and the photon energy increase. In fact, the detection of a gamma induced pulse in the neutron peak could be caused by:

- photons with energy 4.78 MeV or higher;
- the pile-up of different photons, arising in a smaller time than the resolution time of the spectrometer, with total deposited energy equal or greater than 4.78 MeV. In this hypothesis, pulses can be produced by photons below 4.78 MeV. In addition, since the pile-up probability increases as the photon fluence rate increases, the photon response of the spectrometer will increase as the photon kerma rate increases.

In order to “quantify” the above said hypothesis, the photon response of the bare detector (in counts per mGy of photon kerma) has been measured at different values of kerma rate for ^{60}Co and ^{137}Cs, obtaining the results of Figure 3.6.

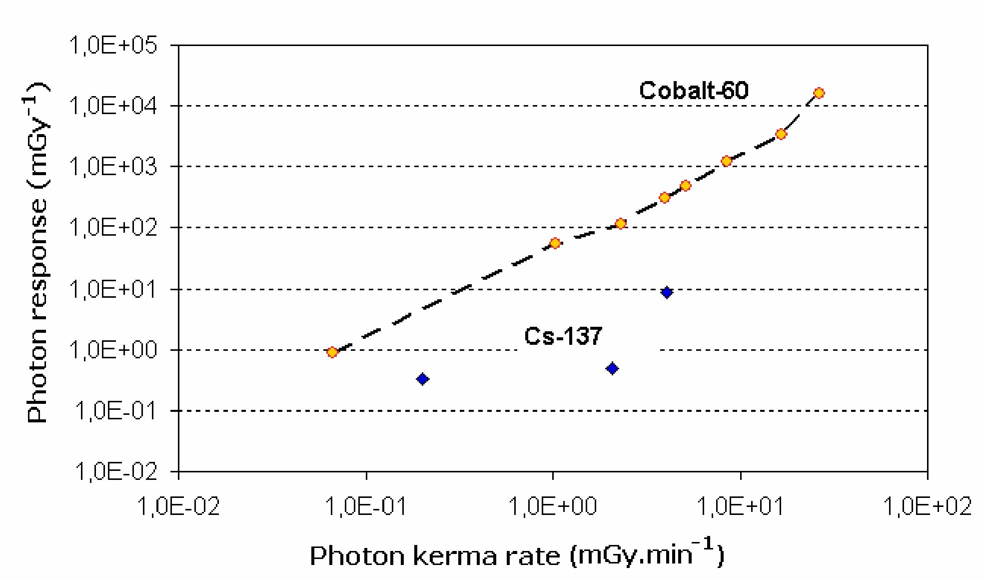

Figure 3.6: Dependence of the photon response of the bare ^{6}LiI detector on the kerma rate for ^{60}Co and ^{137}Cs. All uncertainties on the Cobalt series are less than 5%. For the Cs series the uncertainties range from 15% to 30%.

From Figure 3.6, the photon response to ^{60}Co shows a log-log dependence on the kerma rate; moreover, the change in photon energy from ^{60}Co to ^{137}Cs implies, at the same kerma rate value, a decrease of a factor of about 50 to 100 in the photon response.

As far as the influence of the moderating sphere on the photon response is concerned, an attenuation factor of about 3.1±0.4 has been measured from the bare detector to the 8” configuration; a factor 1.5±0.2 has been measured from 8” to 12”. Both factors refer to the ^{60}Co radiation.

As expected, the photon contribution to the detector response is not negligible. Its magnitude should be evaluated for each specific situation.

In most cases, anyway, this perturbation is not significant, since high photon kerma rates (in the order of 0.1 mGy.min^{-1} = 6 mGy.h^{-1} for ^{60}Co) are required to yield a photon response of 1 count per mGy, which is very low compared with the neutron response of the spectrometer. E.g. for a ^{241}Am-Be source, the neutron response of the spheres ranges from 10000 to 300000 counts per mSv. The photon to neutron dose equivalent ratio for this source is lower than 5%.

In the workplace fields encountered in radiation protection around accelerator facilities, photon kerma rates of ~ mGy.h^{-1} exist only inside the accelerator room in “beam on” condition. Since no personnel is working in such environment, the interest for neutron spectrometry measurement is limited.

The workplaces where the neutron spectrometry is of interest for the radiation protection, i.e.

where personnel can be present, are instead characterized by low kerma rate photon fields (lower than 50 $\mu Gy \cdot h^{-1}$). Moreover, since these places are located behind the shielding structures, the energy distributions are dominated by low energy photons (Sheu, 2003). Measurements performed around DAΦNE with thermoluminescence dosemeters with different filtration showed that the mean energy of the photon field ranges in the 0.2 – 0.3 MeV region, depending on the measurement point (Bedogni, 2006b).

As a conclusion, the gamma sensitivity of the neutron spectrometer can be probably neglected in the majority of the experimental scenarios of our interest. Anyway, since a photon measurement in a given workplace field is usually available or readily achievable, the perturbation due to photons is normally accountable.

3.3 Reproducibility of the LiI detector

In order to monitor the efficiency of the ^{6}LiI(Eu) detector and its reproducibility, an operational check device has been set up. It is a 15 cm diameter x 15 cm height polyethylene cylinder, equipped with two cylindrical cavities, for the LiI detector and the test source respectively (see Figure 3.7). The source is a cylindrical (1.8 cm diameter x 2 cm height) ^{241}Am-Be with reference ^{241}Am activity 3.7 GBq (100 mCi) on 2/5/1986. The neutron emission is around $2.4 \cdot 10^{5}$ s^{-1}. The geometry of source and detector is fixed. Such device is easy to use, the source can be safely stored at the laboratory in a polyethylene container, and the measurements can be done frequently and in few minutes, since the detector counting yield is reasonably high.
The alternative is to check frequently the calibration of the spectrometer in a reference neutron field. In our case, this is done yearly.

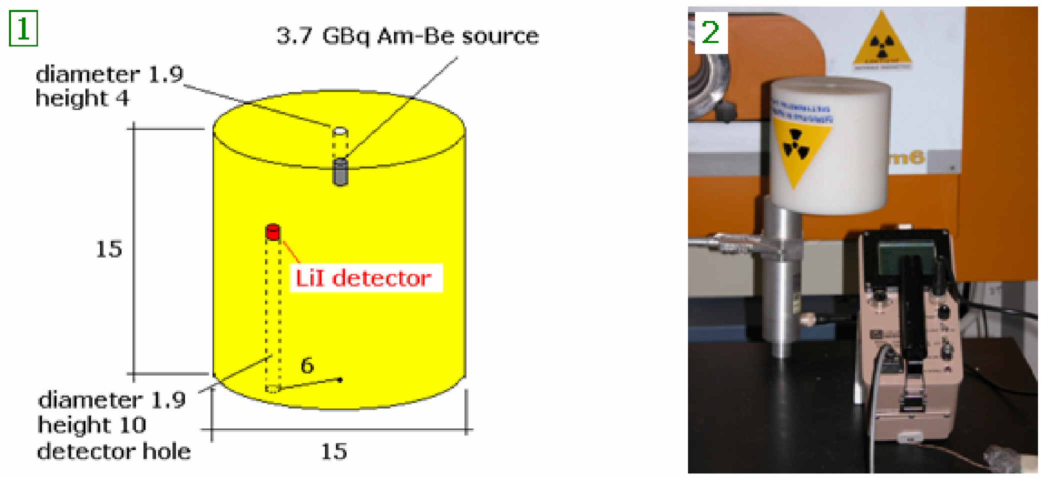

Figure 3.7: The operational reproducibility check device to monitor the efficiency of the LiI detector (1) and the irradiation set up (2). The experimental set up is always used in the same position inside the room, in order to maintain the scattered neutrons contribution constant. All dimensions are in cm.

The detector has been monitored for four days with the just said device. Each day, 10 acquisitions of 1200 s have been performed, every 40 min during the working day. A 1200 s exposure yields nearly 20000 counts. The results are shown in Figure 3.8 and summarized in Table 3.1.

In order to look for variability causes other than the counting statistics, the measurement variability (standard deviation of the measurements distribution, σ) has been separated into a poissonian component, $\sigma_p=1/20000^{1/2}$ = 0.7%, and a residual component, $\sigma_{res}=(\sigma^2- \sigma_p^2)^{1/2}$. The latter, whose maximum value is 0.4%, could be ascribed to voltage fluctuations.

Days	Average count rate (s^{-1})	Measurement variability ($1\ \sigma$)	Poissonian component	Residual component
1	18.02	0.7%	0.7%	none
2	17.96	0.5%	0.7%	none
3	17.97	0.8%	0.7%	0.4%
4	17.87	0.8%	0.7%	0.4%

Table 3.1: Results of the reproducibility test on the LiI detector.

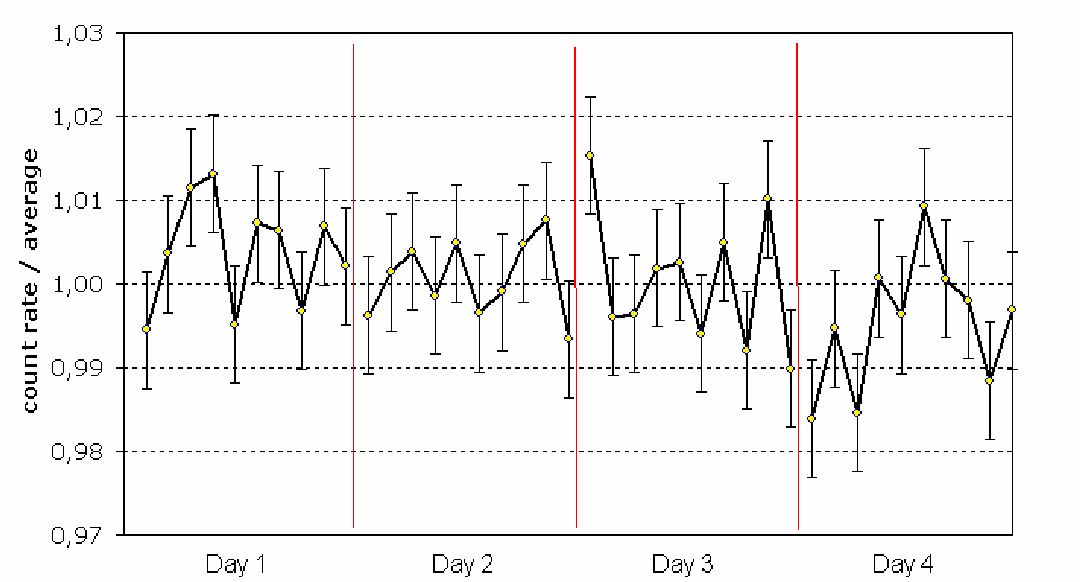

Figure 3.8: Time variability of the efficiency of the LiI detector. All error bars rely on 68% confidence level (1 sigma).

As far as the operative use of the system is concerned, a reproducibility test of two hours (~ 130000 counts) is recommended to establish the working point, and consequently the efficiency, prior to a spectrometry measurement. Then, an additional ±0.4% uncertainty should be added in order to account for voltage fluctuations.

3.4 Calibration of the spectrometer with an ^{241}Am-Be source

The BSS has been calibrated, using the shadow cone technique, in a ISO standard field produced by a ~ 185 GBq (5 Ci) ^{241}Am-Be source (ISO, 2001) at the Secondary Standard Calibration Laboratory of the ENEA – Radiation protection Institute, Bologna (see Figure 3.9). This facility consists of a remote control device which allows locating different sources (ISO standard ^{241}Am-Be, bare and D_2O moderated ^{252}Cf) at the reference position inside a 9.3 m x 8.2 m x 3 m irradiation room.

The source is located at the centre of the room and at 1.75 m height. The source height was experimentally chosen, with the goal of minimizing the scattered radiation at the calibration position (typically from 1 to 2 m from the source). A remote control device allows transferring the sources from the polyethylene bank to the irradiation point and putting it in slow rotation. This allows minimizing the effects of the emission anisotropy on the irradiation plane.

A precision motion system ensures the positioning of the instruments with 0.1 mm accuracy. An actuator allows interposing a suitable shadow cone between the source and the detector to subtract the direct beam contribution. It is also possible to automatically insert the source in a D_2O sphere, designed according to the ISO standards (ISO, 2000). The metrology characterization of this facility is reported elsewhere (Bedogni, 2000).

The irradiation room is equipped with 30-40 cm concrete walls and 16 cm bricks ceiling.

The design and the dimension of the room are very important, because they strongly influence the amount of scattered radiation in the measurement point, which always affects the measurement. Since the instruments should be calibrated to the uncollided neutron spectrum, the scattered radiation in the experimental room should be either reduced by means of appropriate room design or evaluated by means of appropriate calibration techniques, namely the shadow-cone, semi-empirical or polynomial techniques (ISO, 2000).

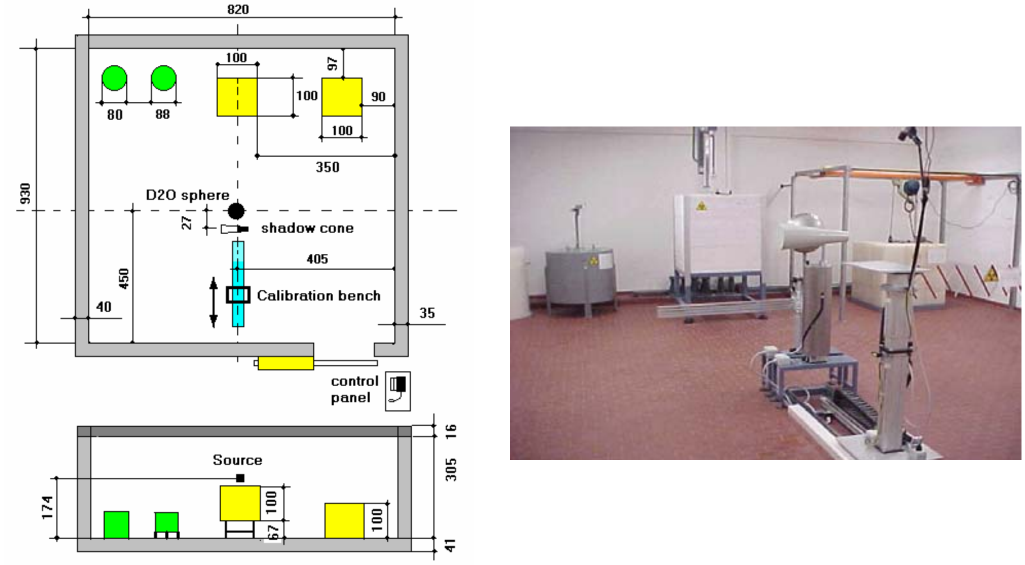

Figure 3.9: The neutron calibration room of ENEA Bologna (dimensions in cm).

3.4.1 *The shadow-cone procedure*

The calibration procedure basically requires the knowledge of two quantities:

- the reference “uncollided” neutron fluence in a given point;
- the contribution of the reference “uncollided” neutron fluence to the instrument reading.

Whilst the first quantity for a reference field is known, the determination of the second one requires the application of special techniques to reduce or measure the “scattered” radiation in the measurement point. The shadow cone technique has been applied for the large spheres: 5”, 8”, 10”, 12” and 12”+Pb.

Each sphere has been exposed in both “total spectrum” and “shadowed” configurations. The contribution of the uncollided fluence, Φ_{ref}, to the reading of the i-th sphere, is therefore calculated as:

$$C_i = C_i^{tot} - C_i^{s} \qquad (3.1)$$

where:

C_i^s is the in-scattered count rate, measured behind the shadow cone. The cone is assumed to completely remove the uncollided radiation.

C_i^{tot} is the total (uncollided + in-scattered) count rate, determined through the non-shadowed measurement.

Three shadow cones of different dimensions are available at the ENEA calibration room. According to ISO 8529-2, the shadow cones are constituted by a 20 cm iron front part, followed by 30 cm polyethylene (at ≥ 5% boron loading) in the rear part (See Figure 3.10). Table 3.2 presents the shielding capability of the ENEA shadow cones, expressed in terms of obscured diameter at a given source-detector distance.

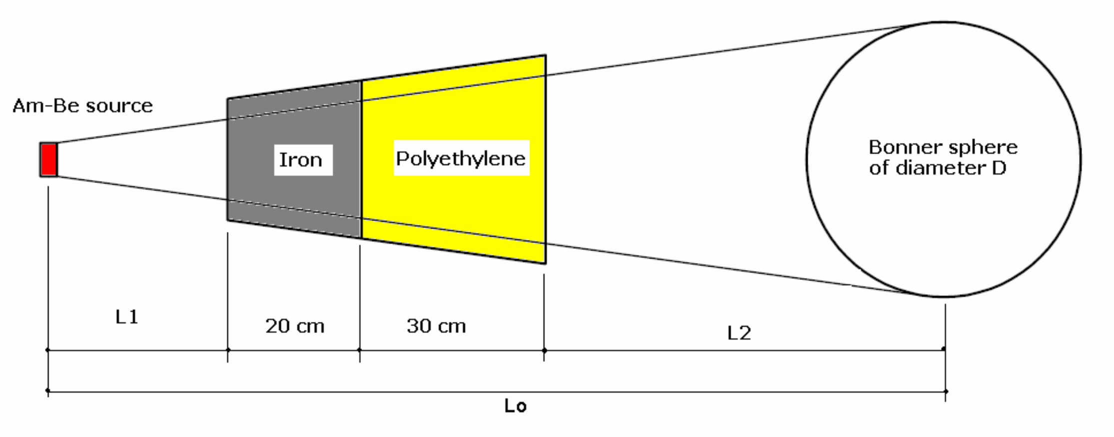

Figure 3.10: Geometry of the irradiation with shadow cone. All dimensions are in cm.

Distance (cm)	Obscured diameter from cone 1 (cm)	Obscured diameter from cone 2 (cm)	Obscured diameter from cone 3 (cm)
60	21.3	13.4	10.5
115	35.0	20.3	15.4
300	81.3	43.7	32.1

Table 3.2: Shielding capability of the cones available at the ENEA calibration room, expressed in terms of obscured diameter at a given source-detector distance.

The correct application of this technique requires the following characteristics:

- a large room, in order to limit the scattered radiation in the measurement point. The increase in the instrument reading due to the scattered radiation should not exceed 40%;

- the source to detector distance: the minimum distance should be greater than twice the shadow-cone length. Being the cones 50 cm long, 115 cm was selected as calibration distance;

- the shadowed area at the calibration distance should be ideally equal to the instrument cross sectional area. In practice, an over-obscuration up to a factor two is acceptable. This limitation is also very important, since in over-shadowed geometries the instrument will underestimate the scattered radiation, giving rise to an overall overestimation of the uncollided radiation. With the available shadow cones, only the 5” up to 12”+Pb spheres met this requirement.

Also the distance between the source and the front face of the cone (L1 in Fig. 3.10) should be accurately optimized:

- at too short distances, the source neutrons emerging at higher angle than that defined by source and detector, would be absorbed instead of contributing to the in-scattered component;

- at too long distances, the in-scattered contribution would be over-estimated, since the obscured angle would be lower than that defined by source and detector.

The optimal distance must be experimentally determined. At the ENEA calibration room, the source to cone distance was fixed to 6 cm.

3.4.2 *The polynomial procedure*

Since no cone was adequate for the smaller spheres (2” and 3”), the polynomial technique has been used to determine the contribution of the “uncollided” radiation to their reading at a given measuring point.

The polynomial technique relies on a series of measurements of the “total field” at different distances from the source, the interpolation of which provides the “uncollided” and the scattered contributions. The formula (3.2) is applied:

$$\frac{C_i^{tot}(L)\cdot L^2}{F_1(L)} = K\cdot(1+A\cdot L+S\cdot L^2) \qquad (3.2)$$

where:

- $C_i^{tot}(L)$ represents the reading of the i-th sphere at the distance *L*.

- *F₁(L)* is the geometric correction factor, which takes into account the “non uniform irradiation” of the detector at short distances. This factor, calculated by using the methods suggested in (ISO, 2000), varies between 1.00 and 1.02 for the 2” and 3” spheres.

- *K* is the “uncollided” contribution, i.e. the count rate of a given sphere at 1 m distance. The uncollided radiation obviously decreases with the distance following the inverse square law.

- $A\cdot L$ and $S\cdot L^2$ represent the air scatter and room scatter contributions respectively.

If the left term of (3.2) is calculated at each distance, then *K*, *A* and *L* are derived by a second degree interpolation in function of *L*. For the scopes of this work, only the value of *K* is of interest.

The 5” sphere has been calibrated with both the shadow cone and the polynomial techniques.

3.4.3 *Results*

The reference quantity, Φ_{ref}, i.e. the uncollided fluence in the test point at 115 cm, has been derived by applying the inverse square law and the air attenuation coefficient to the source strength, as follows:

$$\Phi_{ref} = \frac{B}{4\cdot\pi\cdot l_o^{\,2}}\cdot e^{-\Sigma\cdot l} \qquad (3.3)$$

Where *B* is the source strength (expressed in s^{-1}), l_o the source to detector distance, Σ the air attenuation coefficient. For the ^{241}Am-Be spectrum, $\Sigma = 890 \cdot 10^{-7}$ cm^{-1}. l represents the air distance between source and detector (115 cm), therefore $l = l_o - r$, where r is the sphere radius. Since the variation of the quantity $e^{-\Sigma \cdot l}$ with the sphere diameters is negligible (less than 0.1%), the same Φ_{ref} has been considered for all spheres, being equal to (57.4±0.6) cm$^{-2}\cdot$s^{-1} at 115 cm distance.

Relying on equation. 2.8 the BSS calibration factor can be estimated from each sphere, as follows:

$$f_i = \frac{C_i}{\Phi_{ref} \cdot \sum_{j=1}^{N_g} R^*_{ij} \cdot \varphi_j^{Am-Be} \cdot \Delta E_j} \qquad (3.4)$$

where φ_j^{Am-Be} is the discrete version of the Am-Be ISO spectrum, normalized to unity. The R^*_{ij} functions are known (details on the adopted response functions and the energy binning selected will be given in Chapter 4). Thus, the summation $\sum_{j=1}^{N_g} R^*_{ij} \cdot \varphi_j^{Am-Be} \cdot \Delta E_j = R_i^{Am-Be}$, is also known for all the spheres. C_i, which represents the contribution of the "uncollided radiation" to the sphere reading, is expressed in counts per second (s^{-1}).

Being the factor f only related to the thermal neutron efficiency of the bare detector, it shouldn't depend on the neutron energy and the sphere diameter. Therefore a calibration of a single sphere in a reference neutron field should be sufficient for determining it. In this work, f has been calculated as weighted average of all f_i values. The results are reported in Table 3.3.

For the spheres calibrated with the shadow cone technique (5" up to 12"+Pb), the ratio between the shadowed area and the sphere cross sectional area, R_{shadow}, is also reported in the Table.

For the 2" and 3" spheres, C_i (uncollided count rate at l_o) has been calculated by applying the inverse square law to the K value obtained from the polynomial technique: $C_i = K / l_o^{\ 2}$.

Figures 3.11 and 3.12 illustrate the polynomial fit for the left term of equation 3.2, for the 2" and 3" spheres. The interpolated K value for these spheres is (0.133±0.003) m$^2\cdot$s^{-1} and (0.746±0.007) m$^2\cdot$s^{-1} for the 2" and 3" spheres respectively. For the 5" sphere, a 2% agreement was found between the C_i value calculated with the shadow cone or polynomial methods. Only the shadow-cone value is reported here.

Sphere	C_i (s^{-1})	ΔC_i	R_i^{Am-Be} (cm^2)	f_i	R_{shadow}
bare	-	-	$2.7 \cdot 10^{-4}$	-	-
2”	0.101	±2%	$6.08 \cdot 10^{-3}$	0.289	-
3”	0.561	±1%	$3.39 \cdot 10^{-2}$	0.288	-
5”	2.10	±1%	$1.32 \cdot 10^{-1}$	0.276	1.5
8”	3.18	±2%	$2.01 \cdot 10^{-1}$	0.276	1.0
10”	3.01	±2%	$1.84 \cdot 10^{-1}$	0.285	1.9
12”	2.52	±2%	$1.53 \cdot 10^{-1}$	0.287	1.3
12”+Pb	2.51	±2%	$1.59 \cdot 10^{-1}$	0.275	1.3

Table 3.3: Calibration table of the BSS. The uncertainties are calculated as 1 sigma. The R_i^{Am-Be} value, calculated from the literature response functions (See Chapter 4), can be considered as affected by ±3% uncertainty (See Chapter 5). The “bare” configuration wasn’t considered because its response to ^{241}Am-Be is practically null and affected by large uncertainty.

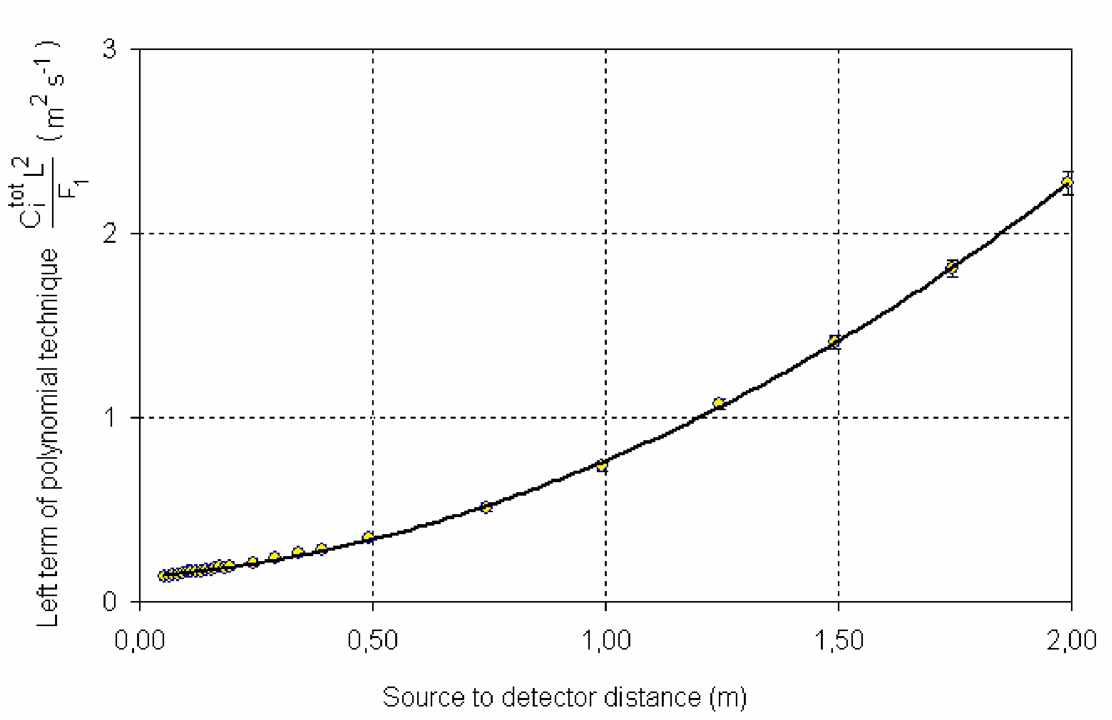

Figure 3.11: Polynomial interpolation for the 2” sphere. The “uncollided” count rate of the sphere at 1 m distance is the constant term of the interpolating equation.

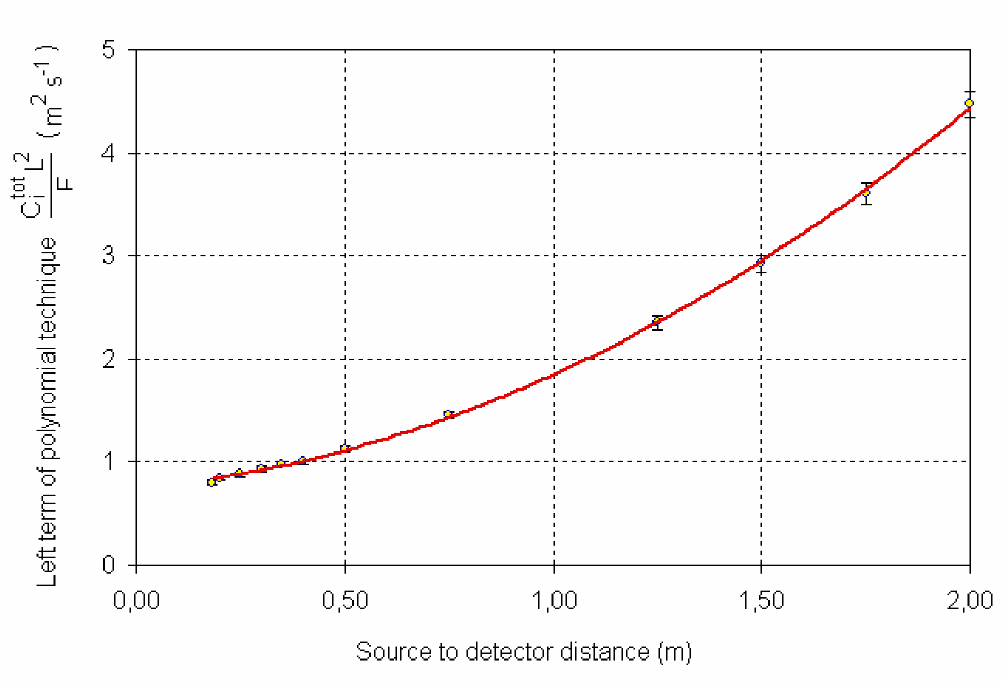

Figure 3.12: Polynomial interpolation for the 3” sphere. The “uncollided” count rate of the sphere at 1 m distance is the constant term of the interpolating equation.

The best estimation of the spectrometer calibration factor, f_{best}, has been obtained as a weighted average of the f_i values obtained from all spheres. As weighting factor, the inverse square of the uncertainty was used. The result is:

$$f_{best} = 0.282 \pm 0.003$$

The uncertainty, 1.2% (calculated as 1 sigma), is the quadratic composition of two terms: the statistical contribution from the weighted average process (±0.6%) and the uncertainty on the reference neutron fluence (±1%). The uncertainty on the R_i^{Am-Be} values (±3%) wasn’t considered at this stage. This will be evaluated in Chapter 5, on the basis of several irradiations in reference fields.

f is far from unity because the calculated BSS response functions rely on a ideal LiI detector of the same dimension as the LNF one. This implies 100% of ^{6}Li with 100% scintillation efficiency, yielding an absolute efficiency possibly very far from the real instrument.

The accuracy of f_{best} can be verified by comparing the measured fluence, $\frac{C_i}{f_{best} \cdot R_i^{Am-Be}}$, with the reference value Φ_{ref}, for the different sphere configurations (See Figure 3.13).

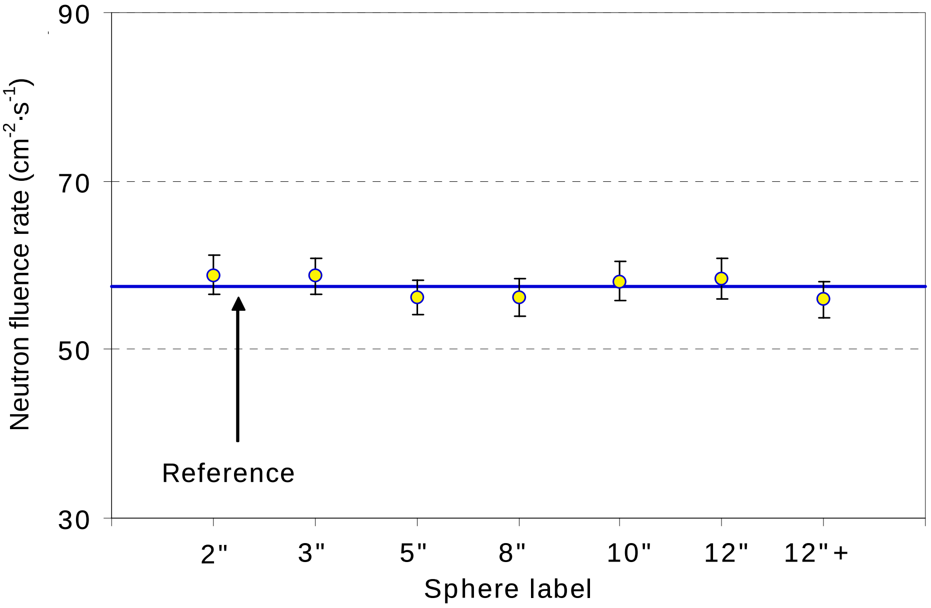

Figure 3.13: Comparison between the neutron fluence measured by each single sphere and the reference value. The blue line represents the reference fluence value. The error bars, around ±4%, take into account the uncertainties on the counts (±1% to ±2%), on f (±1.2%) and on R_i^{Am-Be} (assumed ±3%).

3.4.4 *Correction of the calibration factor for routine measurements*

Immediately before and after the calibration measurements, a two hours reproducibility check (as described in 3.3) has been performed, in order to establish the "point of work" of the system at the calibration time. As a result, the "reference" count rate, $Q_{ref} = (18.01 \pm 0.05)\ \mathrm{s}^{-1}$ has been fixed. Therefore, for a measurement performed at any time, the calibration factor may be corrected as follows:

$$f = 0.282 \cdot \frac{Q}{Q_{ref}} \qquad \pm 1.3\% \qquad (3.5)$$

where f and Q are the calibration factor and the result of the reproducibility test at the measurement time respectively.

The uncertainty associated with f, 1.3%, is the square summation of 1.2% (uncertainty on f_{best}), two times 0.3% (uncertainty on Q and Q_{ref}) and 0.4% (daily variability of the working point, see 3.3).

Chapter 4

SELECTION OF THE ENERGY RESPONSE FUNCTIONS OF THE BSS

4.1 **Overview**

As anticipated in Chapter 2, the knowledge of the energy response function of a given neutron instrument is essential for a correct interpretation of its reading in a given neutron field. This is essential in both dosimetry and spectrometry, since the neutron energy of the workplace neutron fields ranges from thermal up to hundreds of MeV neutrons, and the variability of the response of any instrument over such a large interval is, in principle, very important. Also for the neutron spectrometry with Bonner Spheres, an accurate knowledge of the energy dependence of the fluence response function of each sphere (also called *response function*) is therefore essential. In addition, since the neutron spectrum calculation procedure (unfolding) relies on a set of different sphere readings simultaneously considered, an error affecting a single response function would propagate over the whole unfolding process. This could result in serious deviations in the calculated spectrum and the related integral quantities: fluence, average energy and dose equivalent. Variations of the order of ±15% in the fluence value and ±40% in the fluence averaged energy, have been encountered when unfolding the same BSS readings with different response functions independently determined (Lowry, 1986).

Owing to the mentioned reasons, the calculation or selection of the BSS response functions should be done with accuracy and verified with experimental tests in calibration neutron fields with known fluence rate and energy distribution.

Since the BSS in use at the LNF is the commercial version of the original Bonner instrument, different versions of the related response functions (the while set of response functions is called *response matrix*) are available in literature. Table 4.1 (Mares, 1994), summarizes the main response matrices which have been calculated for the same scintillator and polyethylene density in use at the LNF.

Authors	Year	Reference	Method	Energy range
Sanna	1973	Sanna, 1973	DTF-IV	thermal – 400 MeV
Hertel and Davidson	1985	Hertel, 1985	adjoint method and ANISN	thermal – 17 MeV
Mares and Schraube	1994	Mares, 1994	MCNP4	thermal – 100 MeV

Table 4.1: Main response matrices derived in the past for the LNF spectrometry system.

Among the response matrices reported in Table 4.1, the Sanna version (31 groups) is reported in the IAEA Technical Report Series N. 318 (IAEA, 1990). The Hertel matrix is still used by some authors (Barquero, 2005). Finally, the Mares and Schraube version, adapted to 60 energy groups (up to 400 MeV), has been adopted in the IAEA Technical Report Series N. 403 (IAEA, 2001).
In this work, the Mares and Schraube matrix has been adopted for the following reasons:

- the matrix has been calculated with MCNP. The previous calculations mainly relied on multi-group codes, using discrete cross section libraries and unable to treat the hydrogen bonded in polyethylene for the low energy scattering. These points can be improved with the MCNP code, which, in addition, allows managing complicate geometries.

- the Mares and Schraube matrix has been validated against experimental data taken with quasi-monoenergetic neutrons (at the PTB primary metrology laboratory) in the range from thermal to 14.8 MeV neutrons. The variability of the related calibration factor with the neutron energy and the sphere diameter was ±8% (1 standard deviation). The following spheres were tested: 0" (bare), 2", 3", 4", 5", 7", 8", 10" and 12", whilst the neutron energy were (in MeV): $4.7\cdot10^{-8}$, $1.20\cdot10^{-3}$, $8.15\cdot10^{-3}$, $2.74\cdot10^{-2}$, $7.10\cdot10^{-2}$, $1.44\cdot10^{-1}$, $2.50\cdot10^{-1}$, $4.25\cdot10^{-1}$, $5.65\cdot10^{-1}$, 1.20, 2.50, 5.00 and 14.8.

In this work, this response matrix has been verified with radionuclide neutron sources (see Chapter 5). Moreover, the additional lead loaded sphere has been included and its response, calculated up to 3 GeV (Vylet, 2005) has been also validated.

This work adopts the Mares and Schraube matrix adjusted to 116 energy groups, in order to describe the energy region from $1.5\cdot10^{-9}$ to around 500 MeV neutrons. This upper limit has been fixed in order to completely describe the neutron spectra around DAΦNE, which aren't expected to exceed the 100 MeV.
The binning is equi-lethargic, providing 10 energy groups for each order energy decade. The energy binning is reported in Table 4.2, whilst the response functions are reported in the following paragraph.

1.50E-09	1.88E-08	2.36E-07	2.97E-06	3.73E-05	4.68E-04	5.87E-03	7.37E-02	9.25E-01	1.16E+01	1.46E+02
1.89E-09	2.37E-08	2.98E-07	3.73E-06	4.69E-05	5.89E-04	7.39E-03	9.28E-02	1.16E+00	1.46E+01	1.84E+02
2.38E-09	2.98E-08	3.74E-07	4.70E-06	5.90E-05	7.41E-04	9.30E-03	1.17E-01	1.47E+00	1.84E+01	2.31E+02
2.99E-09	3.75E-08	4.71E-07	5.92E-06	7.43E-05	9.32E-04	1.17E-02	1.47E-01	1.84E+00	2.32E+01	2.91E+02
3.76E-09	4.73E-08	5.93E-07	7.45E-06	9.35E-05	1.17E-03	1.47E-02	1.85E-01	2.32E+00	2.91E+01	3.66E+02
4.74E-09	5.95E-08	7.47E-07	9.37E-06	1.18E-04	1.48E-03	1.85E-02	2.33E-01	2.92E+00	3.67E+01	4.60E+02
5.96E-09	7.48E-08	9.40E-07	1.18E-05	1.48E-04	1.86E-03	2.33E-02	2.93E-01	3.68E+00	4.62E+01	
7.50E-09	9.42E-08	1.18E-06	1.48E-05	1.86E-04	2.34E-03	2.94E-02	3.69E-01	4.63E+00	5.81E+01	
9.44E-09	1.19E-07	1.49E-06	1.87E-05	2.35E-04	2.94E-03	3.70E-02	4.64E-01	5.83E+00	7.31E+01	
1.19E-08	1.49E-07	1.87E-06	2.35E-05	2.95E-04	3.71E-03	4.65E-02	5.84E-01	7.33E+00	9.20E+01	
1.50E-08	1.88E-07	2.36E-06	2.96E-05	3.72E-04	4.66E-03	5.86E-02	7.35E-01	9.23E+00	1.16E+02	

Table 4.2: Energy binning (expressed as central energy of the bin, in MeV) of the LNF response matrix.

4.2 The response matrix

The 116 groups response functions are reported in Figures 4.1, 4.2 and 4.3. All functions are expressed in cm^2, meaning the expected number of ^{6}Li(n,α) reactions per unit neutron fluence at a given energy. The response of the real counter is expected to be proportional to the calculated response through the spectrometer calibration factor *f*, as shown in Chapter 3.

The *bare detector* configuration is the most difficult to simulate and validate, since the absence of moderator makes any detail around the detector essential for the response. Its response isn't completely isotropic, due to the non-spherical shape of the detector and the presence of the photomultiplier and the light pipe. Consequently, different responses can be obtained when changing its orientation with respect to the source. Mares calculated this response function in lateral irradiation geometry, i.e. with the neutron beam perpendicular to the detector axis. The experimental calibration factor shows a ±11% variability (1 standard deviation) with 8 neutron energies from thermal to 14.8 MeV.

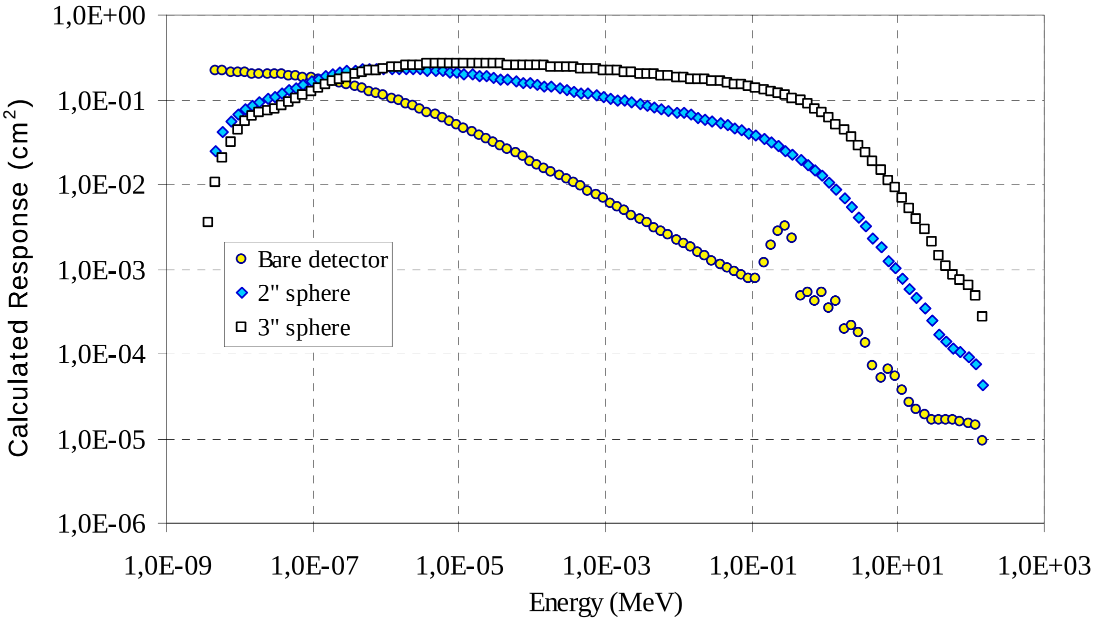

Figure 4.1: Energy response function of the bare detector and of the 2” and 3” configurations.

Similar difficulties also arise in the 2” sphere. Also in this case, the literature calibration coefficient is affected by a ±11% (1 standard deviation) variability as the neutron energy varies. For the 3” up to the 12” sphere, such variability is reduced to 5% - 7%.

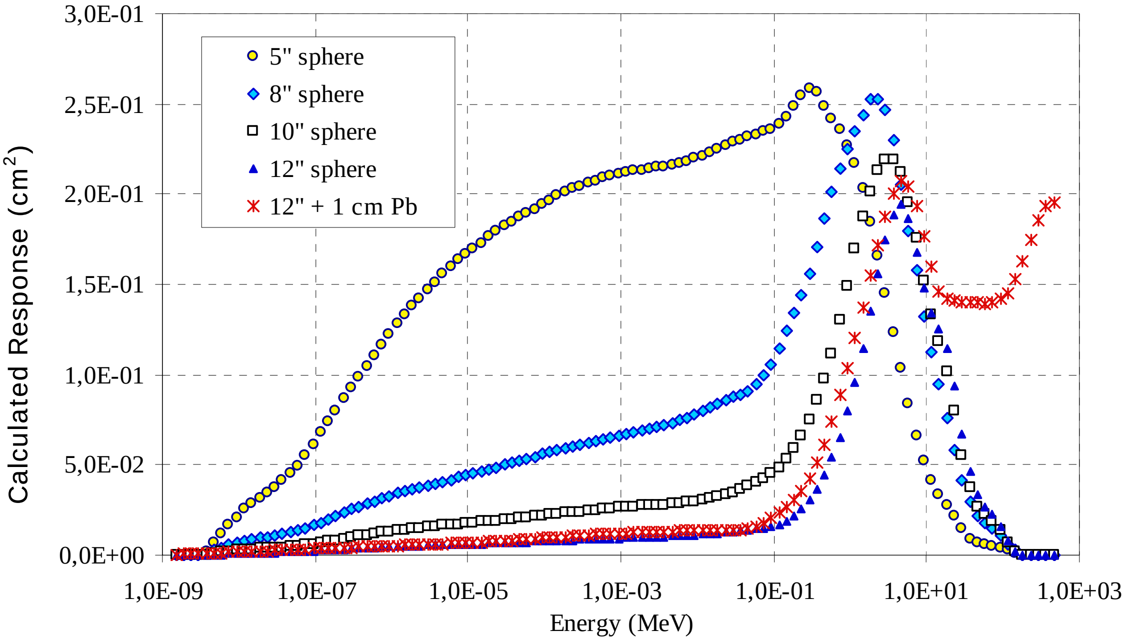

Figure 4.2: Energy response function of the 5”, 8”, 10”, 12” and 12”+Pb configurations.

Figure 4.2 clearly indicates the role of the lead loaded sphere for the energy domain higher than 20 MeV.

The whole response matrix is shown in Figure 4.3, where a solid line joins the individual values of the calculated functions.

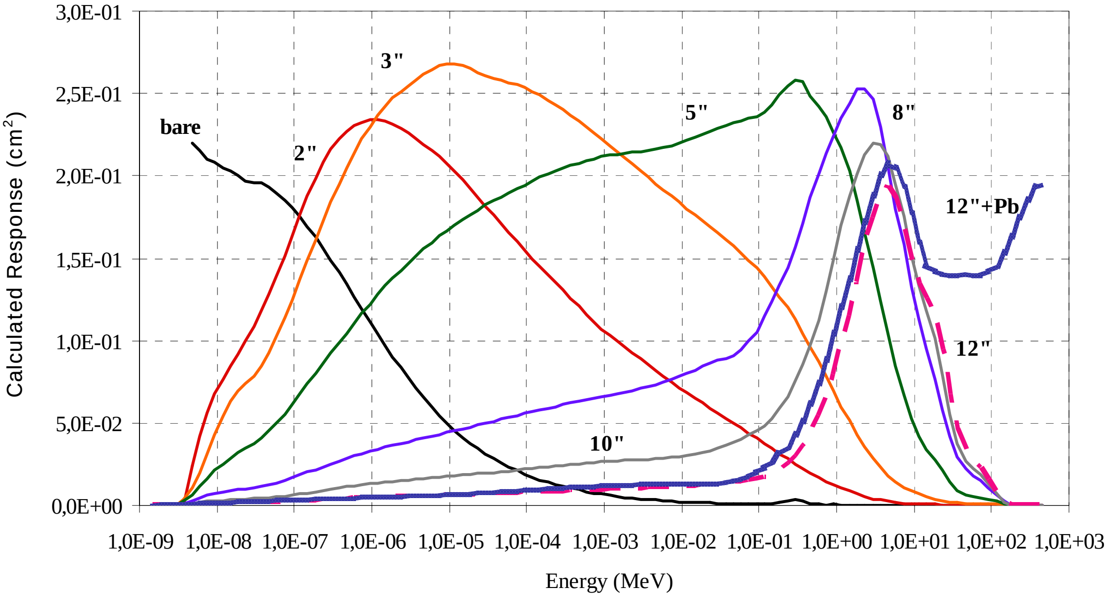

Figure 4.3: Complete response matrix of the LNF spectrometer.

4.3 Geometry verification

In order to evaluate the accuracy of the detector's geometric model used by Mares and Schraube for calculating the matrix, a Monte Carlo calculation with the code MCNPX has been performed for the 8" configuration, taking advantage of the real geometry and materials, as provided by the manufacturer. Figures 4.4 and 4.5 show the detector and its MCNP model, used for the calculation.

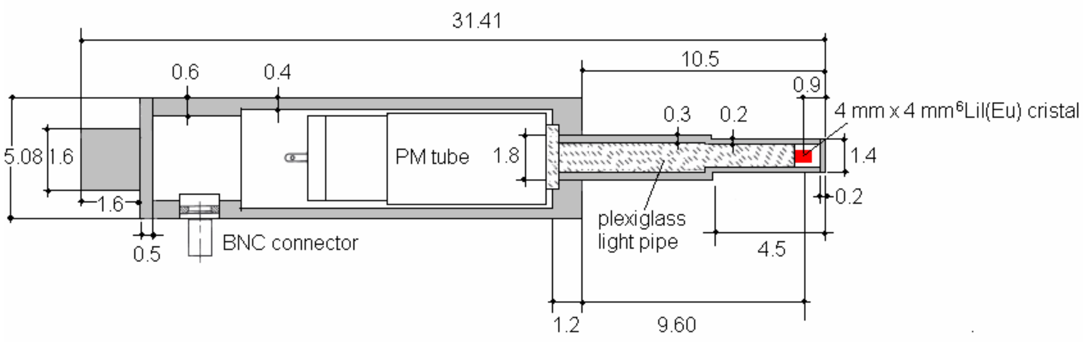

Figure 4.4: Geometry and materials of the LiI detector (not in scale). Dimensions are in cm.

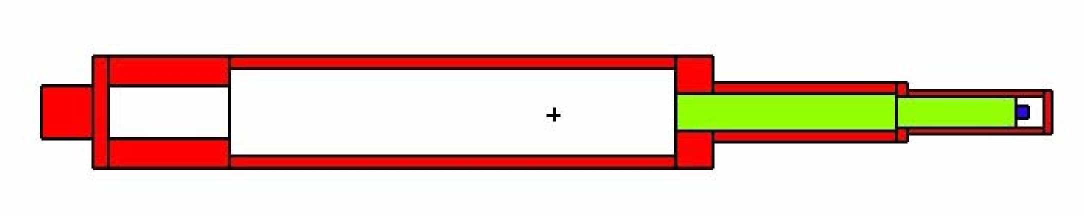

Figure 4.5: MCNP model of the ^{6}LiI(Eu) detector (in scale).

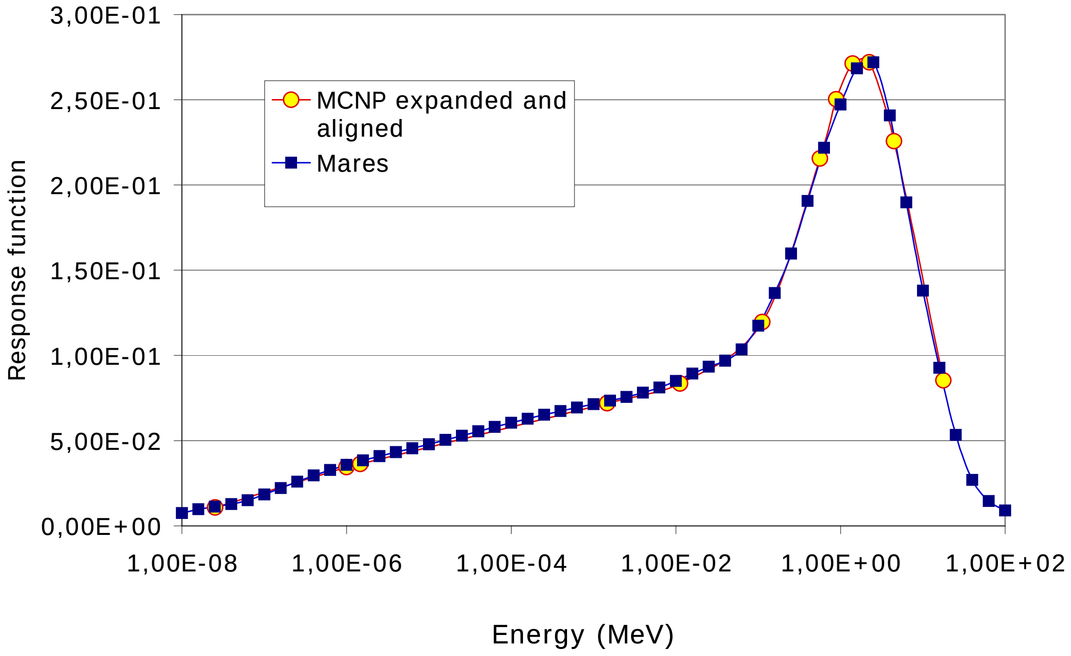

Figure 4.6: 8” sphere - comparison between the literature response function and the MCNPX calculations.

With the MCNP model of Figure 4.5, the 8” sphere configuration has been simulated in 11 energy points only, covering the thermal to 100 MeV range. An aligned and expanded field, emerging from a disk source of the same diameter of the sphere, has been used. The axis of the radiation field and the LiI detector are parallel, i.e. the irradiation geometry was frontal.

As shown in Figure 4.6, the 11 calculated points are in good agreement (within ±1%) with the Mares response function for the 8” sphere.

Then, before using the system on the field, the response matrix has been validated by irradiation with reference neutron fields. This is described in Chapter 5.

Chapter 5

EXPERIMENTAL VALIDATION OF THE BSS RESPONSE MATRIX

5.1 **Introduction**

As said in Chapter 4, the BSS in use at the LNF is a well known commercial instrument, for which various versions of the response matrix have been calculated and used since many years. The most recent version (Mares, 1994), calculated with the Monte Carlo code MCNP, has been validated against reliable experimental data obtained with monoenergetic neutrons at PTB (Alevra, 1992) and thermal neutrons (Thomas D. J, 1994).

Since reliable and validated response functions are available in literature for the LNF instrument, only a limited number of validation experiments with radionuclide neutron sources and thermal neutrons have been performed in this work.

The tests took place at the ENEA-Bologna neutron calibration room, with the previously characterized ISO reference fields (Bedogni, 2002) (Gualdrini, 2004) as follows:

- ^{241}Am-Be, ^{252}Cf, ^{252}Cf(D_2O),
- Thermal neutrons;

For each reference field, the spheres were exposed using the shadow cone or polynomial technique (ISO, 2000) to a given fluence value, Φ_{ref}, and the corresponding readings (uncollided contribution), C_i, have been registered. Then, the reference unity spectrum has been integrated with the response function of the spheres, obtaining the quantity $R_i^{ref\ field}$. The experimental fluence from each sphere and reference field was calculated from

$$\varPhi_{\exp} = \frac{C_i}{f \cdot R_i^{ref\ field}} \qquad (5.1)$$

The accuracy of the response function of a given sphere, in given reference field, has been evaluated from the ratio

$$r_{i,ref\ field} = \left(\frac{\varPhi_{\exp}}{\varPhi_{ref}} \right)_{i,ref\ field} \qquad (5.2)$$

Then, the overall accuracy of the response matrix has been calculated as the standard deviation of the $r_{i,\,ref\ \ field}$ values obtained with different spheres and different reference fields.

In order to determine the contribution of the “uncollided” radiation to the sphere counts, the shadow cone technique has been applied, when adequate cones were available. Thus, the 5”, 8”, 10”, 12” and 12”+Pb spheres have been tested in this condition with the ^{241}Am-Be and ^{252}Cf sources. For the 2” and 3” spheres, the polynomial technique (ISO, 2000) has been applied.

Since no suitable attenuators were available to shield the ^{252}Cf(D_2O) source, the total spectrum in the test point has been used. This has been simulated and kindly provided by G. Gualdrini from ENEA-Bologna.

In the case of the thermal reference field, the “bare” configuration was exposed to the total field. The other spheres weren’t exposed, because their presence could perturb the reference field obtained in a point very close to the facility itself. This facility is described in 5.5.

5.2 Measurements with the ^{241}Am-Be source

The data obtained with the ^{241}Am-Be, used in Chapter 3, to determine the spectrometer calibration factor, are re-organized here in order to derive the quantity $r_{i,\,Am-Be}$ defined in equation (5.2). Table 5.1 shows the results. The ^{241}Am-Be reference fluence at the calibration distance, 115 cm, was (57.4±0.6) cm^{-2}·s^{-1}.

The net count C_i has been obtained from the shadow cone (5”, 8”, 10”, 12” and 12”+Pb) or polynomial fit (2” and 3”) procedures.

Sphere	C_i (s^{-1})	ΔC_i (%)	R_i^{Am-Be} (cm^2)	$\Phi_{\exp}$ (cm^{-2}·s^{-1})	$r_{i,\,Am-Be}$
2”	0.101	±2%	$6.08\cdot10^{-3}$	58.8	1.03
3”	0.561	±1%	$3.39\cdot10^{-2}$	58.7	1.02
5”	2.10	±1%	$1.32\cdot10^{-1}$	56.2	0.98
8”	3.18	±2%	$2.01\cdot10^{-1}$	56.2	0.98
10”	3.01	±2%	$1.84\cdot10^{-1}$	58.1	1.01
12”	2.52	±2%	$1.53\cdot10^{-1}$	58.5	1.02
12”+Pb	2.51	±2%	$1.59\cdot10^{-1}$	55.9	0.97

Table 5.1: Evaluation of the accuracy of the reponse matrix with the ^{241}Am-Be reference field.

5.3 Measurements with the ^{252}Cf source

The ^{252}Cf source has been also measured at 115 cm distance. The shadow cone technique has been used with the 5”, 8”, 10”, 12” and 12”+Pb spheres, whilst the polynomial techniques have been used with the 2” and 3” spheres. The reference fluence at the calibration distance of 115 cm was (494±10) cm^{-2}·s^{-1} on 11/04/2006. The results are reported in Table 5.2.

Sphere	C_i (s^{-1})	ΔC_i (%)	R_i^{Cf} (cm^2)	$\Phi_{\exp}$ ($cm^{-2} \cdot s^{-1}$)	$r_{i,Cf}$
2”	1.37	2%	1.01E-02	484	0.98
3”	7.06	1%	5.38E-02	465	0.94
5”	26.0	2%	1.85E-01	499	1.01
8”	29.7	2%	2.20E-01	478	0.97
10”	24.1	2%	1.73E-01	495	1.00
12”	16.5	2%	1.21E-01	485	0.98
12”+Pb	18.5	1%	1.30E-01	503	1.02

Table 5.2: Evaluation of the accuracy of the reponse matrix with the ^{252}Cf reference field. All uncertainties are expressed as 1 standard deviation.

5.4 Measurements with the ^{252}Cf(D_2O) source

As anticipated in 5.1, the measurements with the moderated Californium source have been performed using the total spectrum at 115 cm, calculated with the Monte Carlo code MCNP (See Figure 5.1). The total fluence at the measuring point on 12/04/2006 was (820±20) $cm^{-2} \cdot s^{-1}$.

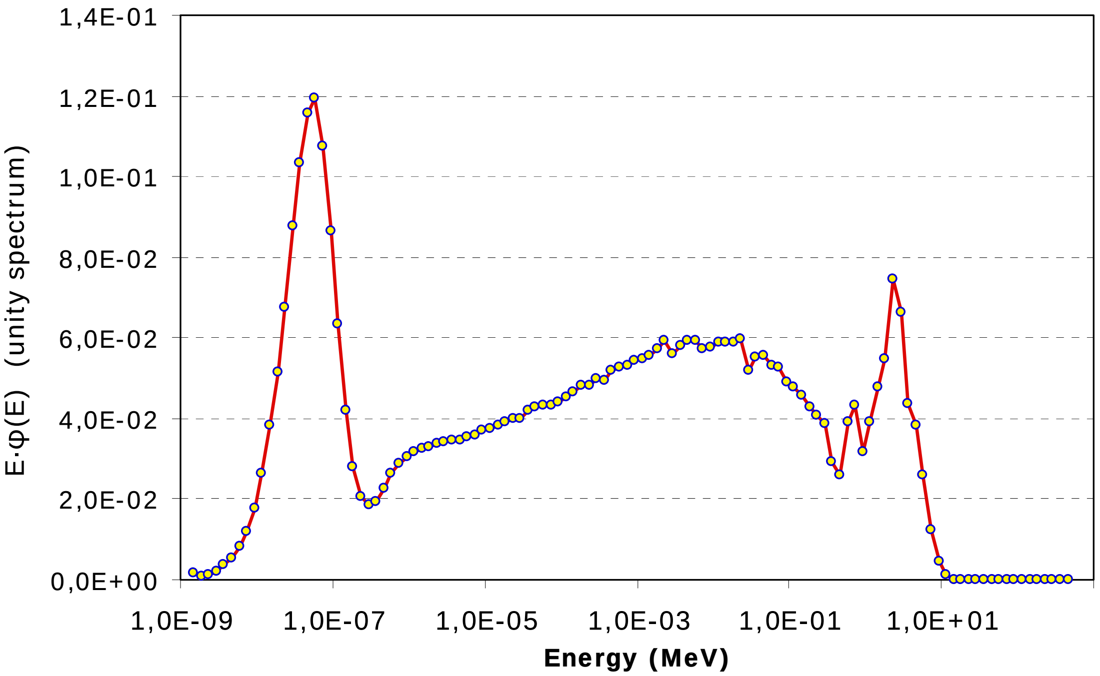

Figure 5.1: Total spectrum of the ^{252}Cf(D_2O) source at 115 cm distance calculated with MCNP (normalized to unity integral and in equilethargic representation).

The results are reported in Table 5.3.

Sphere	C_i (s^{-1})	ΔC_i (%)	R_i^{Cfm} (cm^2)	$\Phi_{\exp}$ ($cm^{-2} \cdot s^{-1}$)	$r_{i,Cfm}$
2”	25.9	1%	1.09E-01	846	1.03
3”	37.4	1%	1.63E-01	816	0.99
5”	36.2	1%	1.62E-01	794	0.97
8”	17.0	1%	7.65E-02	788	0.96
10”	9.93	1%	4.24E-02	830	1.01
12”	5.62	2%	2.36E-02	843	1.03
12”+Pb	6.56	2%	2.61E-02	893	1.09

Table 5.3: Evaluation of the accuracy of the response matrix with the $^{252}Cf(D_2O)$ reference field. All uncertainties are expressed as 1 standard deviation.

5.5 Measurements with the thermal neutrons field

The ENEA-Bologna thermal neutron reference field has been recently set up (Gualdrini, 2004; Bedogni, 2004) by adapting an existing facility, a 1 m x 1 m x 1 m polyethylene cube with three Am-Be sources embedded and three coaxial irradiation internal cavities (Figure 5.2a). One of the polyethylene modules, formerly used to position the samples inside the largest cavity, has been removed. Thus, a 20 cm x 20 cm thermal column has been created. The fluence profile along the column section has been flattened with a polyethylene pyramidal filter, in order to create a homogeneous irradiation area. The calibration area (Figure 5.2b), defined at 5 cm distance from the column output, has been characterized through MCNP simulation and gold foils measurements.

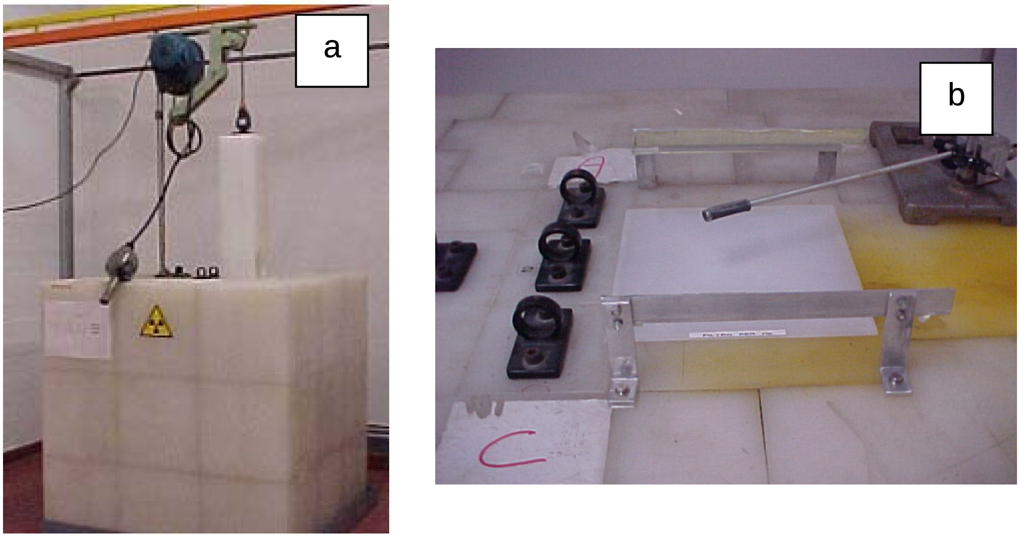

Figure 5.2: The ENEA-Bologna thermal neutrons calibration facility on the left (a) and the thermal column output with the pyramidal flattening filter on the right (b).

The neutron spectrum at the central point of the calibration area, calculated with MCNP, is reported in Figure 5.3.

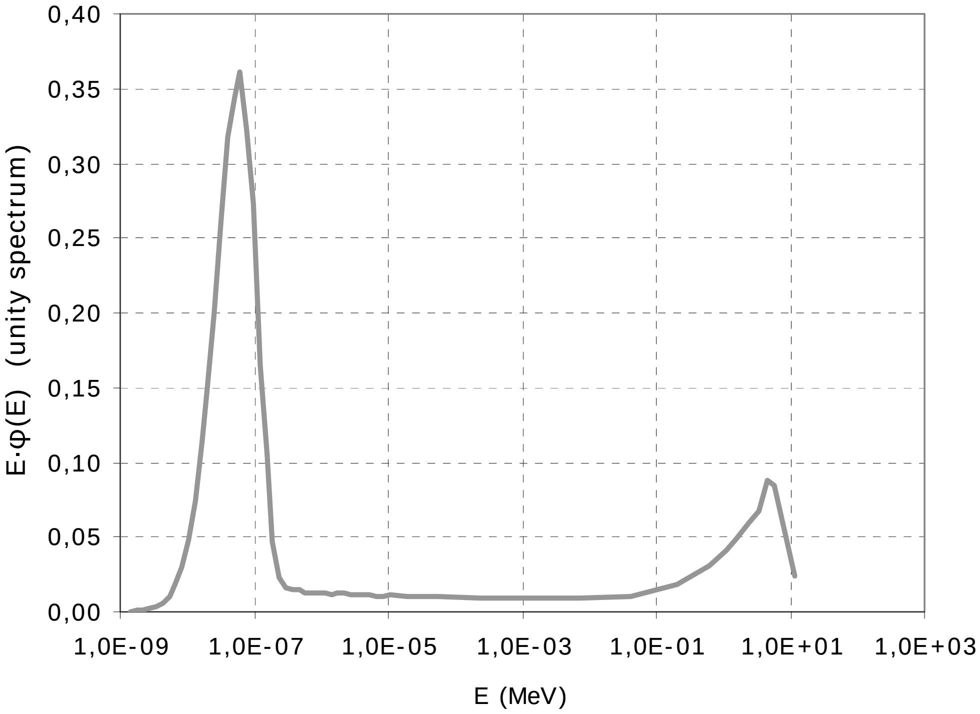

Figure 5.3: Neutron spectrum in the central point of the calibration area of the ENEA Bologna calibration facility (normalized to unity integral and in equilethargic representation).

The total neutron fluence in central point of the calibration area at the measuring time was (608±9) $cm^{-2}\cdot s^{-1}$. The "bare" detector has been exposed in this point with "lateral" irradiation geometry, i.e. the detector axis was perpendicular to the axis of the thermal column (as the response function of the detector was calculated). The spheres weren't exposed in this facility, because their presence could perturb (through multiple scattering with the facility itself) the field in the reference point.

The result for the "bare detector" is reported in Table 5.4.

Sphere	C_i (s^{-1})	ΔC_i (%)	$R_i^{thermal}$ (cm^2)	Φ_{exp} ($cm^{-2}\cdot s^{-1}$)	$r_{i,\,thermal}$
bare	22.2	1%	1.30E-01	605	0.99

Table 5.4: Evaluation of the accuracy of the "bare" detector response with the ENEA-Bologna thermal neutron reference field. The uncertainties are expressed as 1 standard deviation.

5.6 **Final considerations**

The results of the validation test show that the discrepancy of the Mares and Schraube matrix with respect to the experimental points reaches a maximum value of 9%. The distribution of the $r_{i,\,ref\;\;field}$ has mean value of 1.00 and standard deviation of 3%.

±3% can be therefore considered as the uncertainty contribution arising from the detector modeling and the Monte Carlo simulation of the response functions. Table 5.5 summarizes the results.

Sphere	Thermal	^{252}Cf(D_2O)	^{252}Cf	^{241}Am-Be
Bare	0.99			
2”		1.03	0.98	1.03
3”		0.99	0.94	1.02
5”		0.97	1.01	0.98
8”		0.96	0.97	0.98
10”		1.01	1.00	1.01
12”		1.03	0.98	1.02
12”+Pb		1.09	1.02	0.97

Table 5.5: Results of the validation experiments. The quantity $R_i^{ref\;\;field}$ for each sphere and reference field is reported.

Chapter 6

UNFOLDING PROCEDURES

6.1 Overview

This chapter will address the neutron spectra unfolding problem and the main methods to solve it. Since an extensive mathematical approach is given elsewhere (Matzke, 2003), the topic will be presented here under a "practical" approach.

The computer unfolding codes will be introduced, with special attention to the MITOM code (Thomás, 2004), developed at he UAB. A new unfolding code, developed at the INFN-LNF on the basis of the MITOM convergence algorithm, will be described. The new code, FRUIT (FRascati Unfolding InTeractive code) has been developed in the LabView visual environment for the needs of the LNF Radiation Protection Group, concerning the physical surveillance around the Frascati electron accelerators. Moreover, the code is supposed to be used for scientific inter-comparisons and research activities in neutron dosimetry and spectrometry.

6.2 The unfolding problem

As anticipated in Chapter 2, the determination of the neutron fluence from the reading of the BSS is equivalent to solve for φ_j the following system:

$$C_i = f \cdot \Phi \cdot \sum_{j=1}^{N_g} R^*{}_{ij} \cdot \varphi_j \cdot \Delta E_j \quad \text{i=1,..,m (number of spheres)} \qquad (6.1)$$

The calibration procedure, described in Chapter 3, and the establishment of a well known response matrix (Chapters 4 and 5), allow determining the quantities *f*, $R^*{}_{ij}$ and their uncertainties.

The unfolding problem in the Bonner Sphere Spectrometry is under-determined, i.e. the number of independent measurements, *m*, is largely lower than the number of unknown, *Ng*. This, together with the relevant overlapping between the energy response function of different spheres, implies that "*fine structures*" eventually present in the fluence energy distribution, such as "resonance" narrow peaks, could be lost during the inversion procedures. Moreover, a mathematical consequence of the under-determination is that an infinite number of functions could satisfy equation (6.1). Normally, only a small sub-set of meaningful functions satisfy this equation, within some tolerance connected to the statistical and systematic uncertainties affecting the sphere counts and the response matrix.

In practice, the unfolding procedure applies the response matrix of the spectrometer to a "trial spectrum", obtaining a set of "calculated" sphere counts, C_i^{calc}, which in comparison with the measured counts, C_i, provides an "error signal" that gives information about the vicinity of the trial spectrum to the unknown fluence spectrum. Then the trial spectrum is iteratively varied until the error signal is "small enough" compared with the statistical and systematic uncertainties. The convergence procedure attempts minimizing the following reduced chi-squared value:

$$\chi^2 = \frac{1}{m-1}\sum_{i=1}^{m}\frac{(C_i - C_i^{calc})^2}{u_i^2} \quad \text{i=1,..,m} \qquad (6.2)$$

Where *m* is the number of sphere readings, C_i the measured count for the i-th sphere, C_i^{calc} the count of the the i-th sphere calculated by applying the sphere response function to the trial spectrum and u_i an uncertainty term (one standard deviation) which quadratically combines the uncertainties affecting C_i and C_i^{calc}. The uncertainty on C_i^{calc} has been estimated by validation experiments, as described in Chapter 5.

6.3 **Main methods to solve the inverse problem**

6.3.1 Least-square methods

The calculation procedure on the basis of the least-square methods is able to include all possible information on the problem to be solved, namely the sphere counts, any a priori determination of the fluence spectrum (obtained by calculation, previous measurements or published data) and pre-information on the response matrix. All pre-information must be accompanied by the uncertainties. A general chi-square is defined, combining the quadratic difference between measured and calculated counts, initial and calculated fluence spectrum, initial and calculated response matrix. According to the iterative algorithm used to minimize that general chi-square, several least-square based unfolding computer codes have been developed. Those codes are characterized by very high degree of flexibility, e.g. the possibility to treat variable response matrices. On the other side, a priori information on the fluence spectrum is highly recommended to obtain meaningful results. Moreover, negative fluence values could arise from the algorithm. To remediate the latter, codes based on the logarithm (STAY'SL (Perey, 1978) and its improved PTB version, MINCHI (Matzke, 1994), SAND II (McElroy, 1967) and its improved version GRAVEL (Matzke, 1994), BUNKI (Lowry, 1984) and SPUNIT (Doroshenko, 1977)) or square power (LOUHI code (Routti, 1980)) of the sphere counts have been developed.

Owing to the strong dependence of the results on the initial hypothesis, it is useful to use those codes only when reliable information is available, e.g. when a MCNP calculation or a spectrum from another type of code is provided.

6.3.2 Methods relying on the Bayesian theory and the principle of maximum entropy

The specialized literature (Matzke, 2003) refers that a number of recently developed codes, relying on the Bayesian methods (such as MITOM) or the maximum entropy principle (MIEKE (Matzke, 1994), UNFANA (Weise, 1995) and MAXED (Reginatto, 1998)), generally provide more reliable results compared to the least-square based codes. These methods are considered to be less dependent on the initial guess hypothesis and allow evaluating the uncertainties on the results. As far as the Bayesian methods (or Monte Carlo based methods) are concerned, they usually operate by modelling a fluence spectrum with a set of parameters. The code simulates a number of such sets by iterative process and calculates the associated fluence spectra. The spectrometer response matrix is then applied to each of these spectra, obtaining the calculated sphere counts C_i^{calc}. Only the sets which provide a “small enough” value of χ^2 are then selected, and their average is used to generate the best approximation of the fluence spectrum to be determined. The Bayesian theorem states that the limit of such average, when the number of trials tends to + ∞, tends to the solution of the problem.

6.4 **A priori information and performance of the codes**

Since the inverse problem in Bonner Sphere spectrometry is largely under-determined, some initial hypothesis are usually introduced in the unfolding codes in order to facilitate the converge process and avoid meaningless results. Some “a priori” information are necessarily required by physical constraints, as described by Alevra and Thomas (Alevra, 2003):

- no negative values for the neutron fluence are accepted;
- if applicable, upper limit for neutron energy (e.g. 20 MeV for fission reactors);
- the lower energy part of the spectrum has a Maxwellian shape;
- the solution should be a smooth function. The unfolding codes are even able to recognize broad peaks. If narrow peaks, fine structures or oscillations aren’t present in the guess spectrum and appear in the final spectrum, the unfolding code had a failure.

Some unfolding codes require an initial guess spectrum: for the least-square based methods this information is usually derived by Monte Carlo simulation or previous estimations. The guess spectrum strongly influences the results and should be therefore as realistic as possible. For the Bayesian methods the choice of the guess spectrum is, in general, less crucial.

For those codes which model the spectrum as a function of a set of parameters, an initial value for such set is usually required as “guess” hypothesis.

In a recent work (Alevra, 2003), five commonly used unfolding codes are inter-compared: MAXED, MINCHI, GRAVEL, UNFANA and MIEKE. The first three require a guess spectrum, whilst UNFANA and MIEKE do not accept a priori information. MAXED, MIEKE and UNFANA rely on the maximum entropy principle, whilst GRAVEL and MINCHI are least-square methods. Sphere counts taken in three different fields (thermal, epithermal and fast) were introduced in all codes. A flat *1/E* spectrum was used as guess spectra for MAXED, MINCHI and GRAVEL. UNFANA and MIEKE (no a priori information accepted) provided unreliable results, including oscillating structures and narrow peaks. The remaining codes provided smooth solutions, but quite far from the true spectra. Only using appropriate “educated” guess spectra, which included a priori information on the specific fields, good results were provided by MAXED, MINCHI and GRAVEL.

As a conclusion, all the employed codes provided satisfactory results as far as the integral quantities (fluence, ambient dose equivalent) are concerned. Some codes were also able to correctly infer the neutron spectrum, only using “educated” guess spectra.

In general, simple and smooth spectra can be correctly unfolded by the codes, whilst the correct measurement of complex fields (with narrow peaks and fine structures) remains an unsolved problem. For all the investigated codes, the result is strongly influenced by the quality of the a priori information.

The following factors, in addition to the availability of accurate BSS measurements and a well established response matrix, appear to be crucial to obtain good results:

1) good quality a priori information;
2) expert operator.

With the MITOM code (See 6.5), developed by the UAB for nuclear reactor spectra, the dependence of the results from the a priori information has been reduced. The new Frascati unfolding code, FRUIT, taking advantage of the UAB experience, attempts to make the above mentioned factors “less crucial”, in order to provide a simple, interactive and quick tool for research as well as routine monitoring purposes.

With a similar philosophy, the PTB recently developed the NUBAY code, in the WinBUGS ver. 1.4 visual environment (Spiegelhalter, 2003).

6.5 The MITOM code from UAB

6.5.1 *Spectra representation*

Since detailed descriptions of the MITOM code are given elsewhere (Bakali, 2001; Thomás, 2004), only its relevant features will be reported here.

In MITOM, a generic neutron spectrum is described as the linear superposition of three components, namely a Maxwellian ($\varphi_t(E)$), an epithermal ($\varphi_e(E)$) and a fast neutron component ($\varphi_f(E)$), each of them has unity integral.

$$\varphi_t(E)\,\alpha\,\frac{E}{T^2}\cdot e^{-\frac{E}{T}} \qquad \text{with} \quad E < 0.1\text{ eV} \qquad (6.3)$$

Where $T = 0.025$ eV. $\varphi_t(E)$ rapidly falls to zero for $E > 0.1$ eV.

For the intermediate energy range, the classical *1/E* form is no longer applicable, since that function diverges for $E \to 0$ and, for energy of ~ keV, it decreases too slowly. Therefore the following form has been adopted:

$$\varphi_e(E)\,\alpha\left(1-e^{-\frac{E^2}{E_d^2}}\right)\cdot E^{b-1}\cdot e^{-\frac{E}{\beta'}} \qquad (6.4)$$

$0.1\text{ eV} < E < 10\text{ keV}$; $-0.5 < b < 0.5$; $0 < \beta' < 1$

Where the first factor, with E_d=0.0707 eV, limits the function at lower energy, whilst $e^{-\frac{E}{\beta'}}$ ensures a rapid decrease as E increases. b quantifies the departure from the $1/E$ behaviour in the intermediate energy region. The influence of b and β'on the epithermal spectrum shape is shown in figures 6.1 and 6.2.

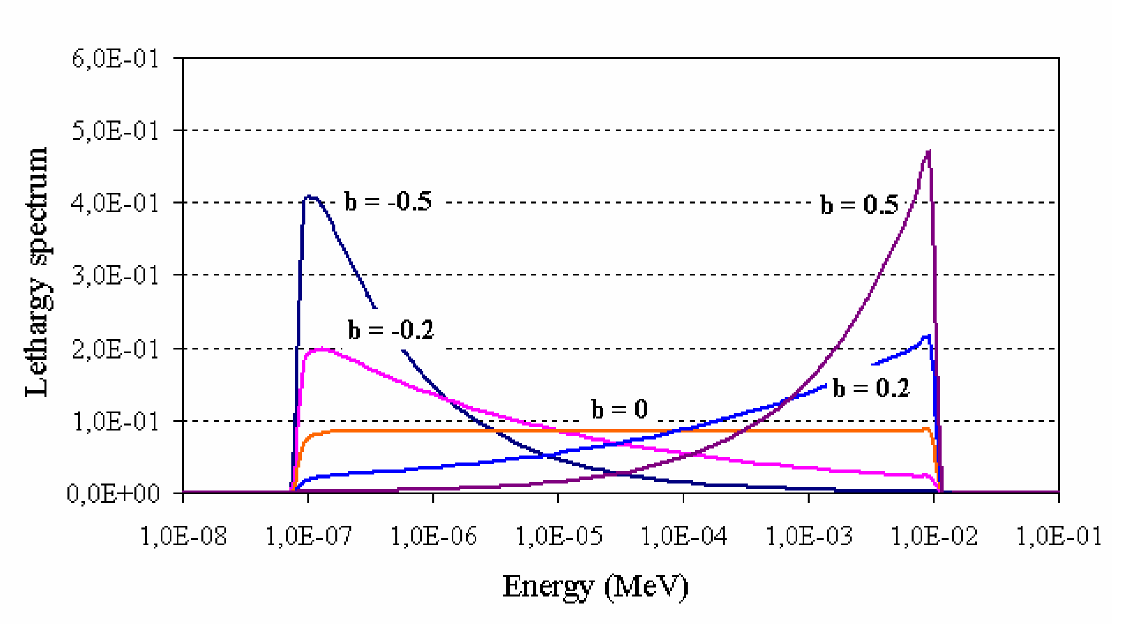

Figure 6.1: Variation of the epithermal spectrum as the parameter *b* varies between -0.5 and 0.5. *b*=0 corresponds to the classical 1/*E* spectrum. The parameter *β'* is fixed at 0.5. (Spectra normalized to unity integral and in equilethargic representation).

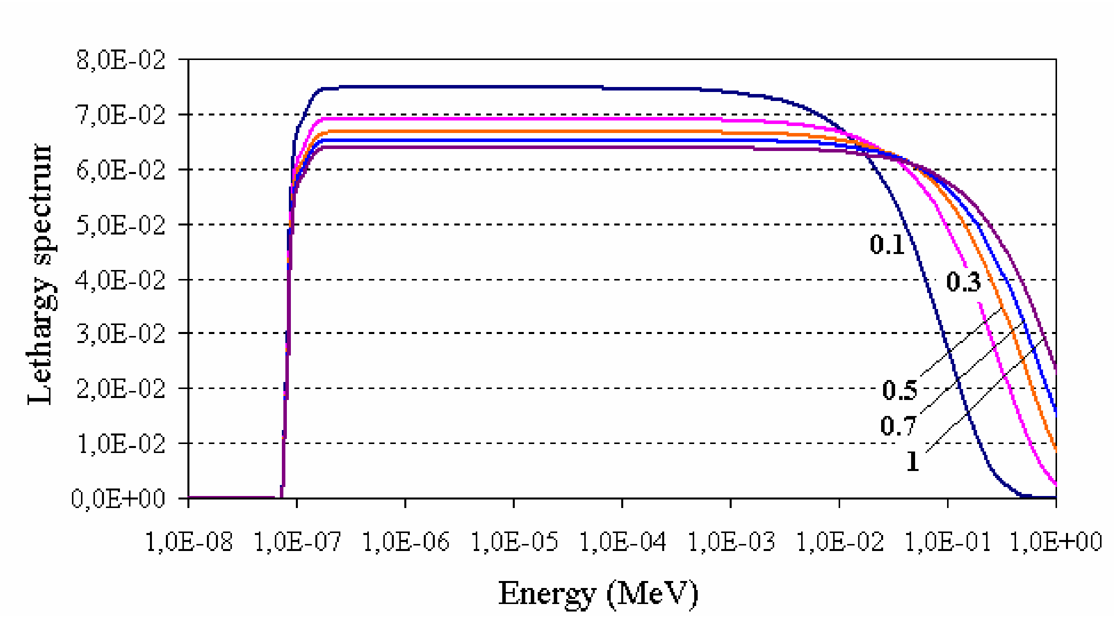

Figure 6.2: Variation of the epithermal spectrum, as the parameter *β'* varies between 0.1 and 1. The *b* value is fixed to 0. (Spectra normalized to unity integral and in equilethargic representation).

The fast neutron component is simply described by a Watt function:

$$\varphi_f(E)\ \alpha\ E^{\alpha}\cdot e^{-\frac{E}{\beta}} \qquad (6.5)$$

$$E > 1\ \text{keV}; \qquad 0 < \alpha < 1; \qquad 1 < \beta < 2$$

The influence of α and β on the fast component of the spectrum is shown in figures 6.3 and 6.4.

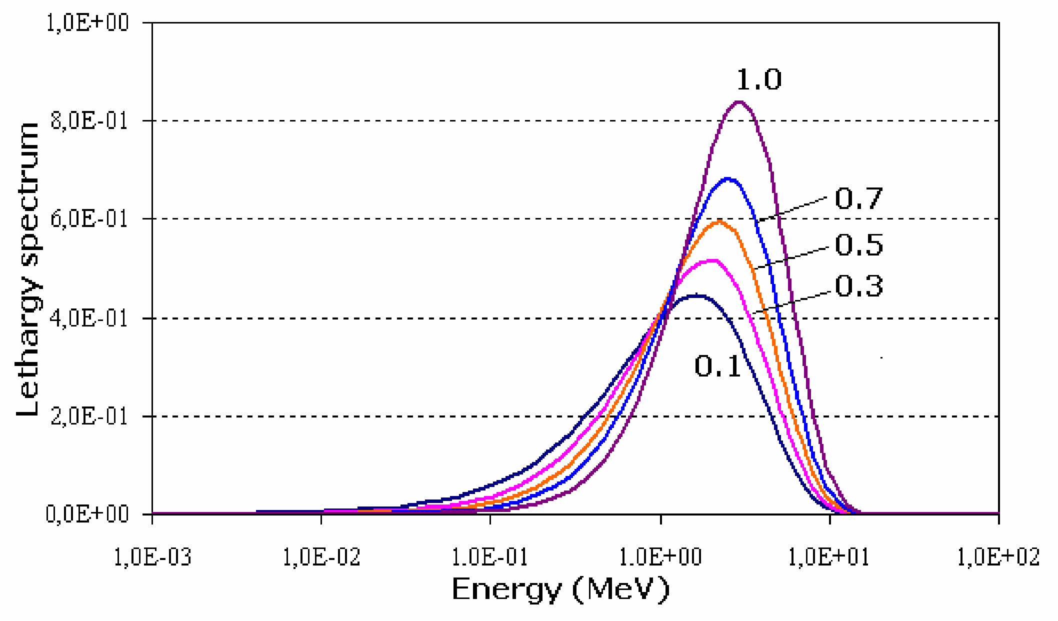

Figure 6.3: Variation of the fast neutron component, as the parameter α varies between 0.1 and 1. The β value is fixed to 1.5. It should be noted that, as α increases, the peak becomes narrower and tends to shift towards the high energy region. (Spectra normalized to unity integral and in equilethargic representation).

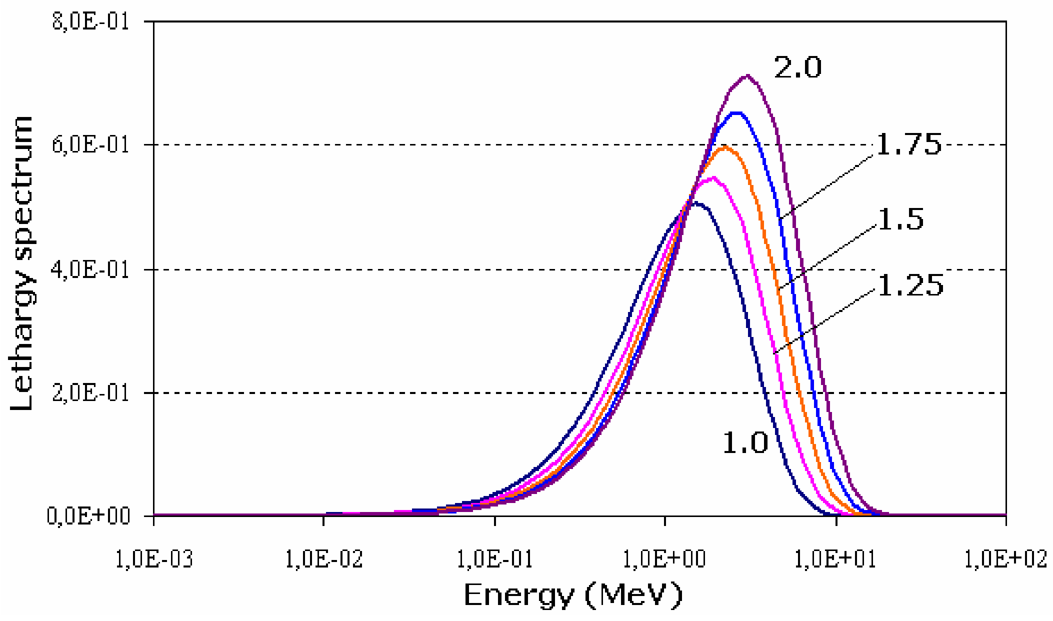

Figure 6.4: Variation of the fast neutron component, as the parameter β varies between 1 and 2. The α value is fixed to 0.5. The peak shift effect is more evident than in figure 6.3. (Spectra normalized to unity integral and in equilethargic representation).

A generic fluence spectrum with unity energy integral can be expressed as a weighted sum of the three functions with weighting factors P_t , P_e ,and P_f .

$$\varphi(E) = P_t \cdot \varphi_t(E) + P_e \cdot \varphi_e(E) + P_f \cdot \varphi_f(E) \qquad (6.6)$$

P_t , P_e ,and P_f are positive or null and $P_t + P_e + P_f = 1$.

If the total neutron fluence is $\varPhi$ and its guess value is $\varPhi_o$, then the following equation can be introduced:

$$\varPhi = \varPhi_o (1 + \delta) \qquad (6.7)$$

Where δ is a perturbation dimensionless parameter. $\varPhi_o$ is directly calculated from the sphere counts using the "three spheres methods" (Bakali, 2001).

Finally, a generic fluence spectrum, of which the expression is

$$\varPhi\,(\mathrm{E}) = \varPhi_o\,(1 + \delta)\,\varphi(E) \qquad (6.8)$$

depends on an array of seven independent parameters, $\{x_j\}_{,\, j=1,..,7}$;

$$\{\mathrm{x}_\mathrm{j}\}_{j=1,..,7} = \{\,\alpha, \beta, \beta', b, P_t, P_f, \delta\,\} \qquad (6.9)$$

6.5.2 *Determination of the spectrum parameters*

MITOM firstly calculates $\varPhi_o$ on the basis of the mentioned "three spheres method". After that, the convergence procedure requires a guess value for the array $\{\mathrm{x}_\mathrm{j}\}$, here called $\{\mathrm{x}_j\}^0$. This guess value should be selected on the basis of previous knowledge on the spectrum to be studied. That value enters in an interactive procedure (William, 1992) briefly described below.

At the k-th interaction of the code, the parameters $\{\mathrm{x}_j\}^k$ are used to derive the k-th spectrum $\varPhi^{\mathrm{k}}$(E), to which the BSS response matrix is applied to obtain the correspondent array of calculated Bonner Sphere counts, $C^k_{calc,i}$ (i=1,..,m). The calculated counts are then compared with the measured data, obtaining the "single sphere deviations", $\xi^k_i\ {}_{i=1,..,m}$, and the "global deviation" , $\varDelta^k$, summed over all spheres:

$$\varDelta^k = \sum_{i=1}^{m} \xi_i^k = \sum_{i=1}^{m} \frac{\left| C_{calc,i}^k - C_{meas,i} \right|}{u_i} \qquad (6.10)$$

The sphere with highest deviation is identified and its deviation $\xi_{\max}^k$ is registered.

Now the following procedure is operated to change one of the parameters, randomly selected:

$$x_f^{k+1} = x_f^k + T_f \cdot (\varGamma - 0.5) \qquad (6.11)$$

Where $\varGamma$ is a random number between 0 and 1, and T_f a tolerance factor, typically of the order of 10^{-3} - 10^{-4}. The (k+1)-th parameter array will be constituted by the k-th one where the f-th parameter has been changed to x_f^{k+1}. Relying on the new parameter array, $\{x_j\}^{k+1}$, the single and global deviations are calculated and the following tests are performed, in order to decide whether $\{x_j\}^{k+1}$ will be accepted in place of $\{x_j\}^k$, or not:

Accepted change:

1) $\varDelta^{k+1} < \varDelta^k \quad and \quad \xi_{i,\ i=1,..,m}^{k+1} < \xi_{\max}^k$, or

2) $\varDelta^{k+1} < \varDelta^k \quad and \quad \xi_{i,\ i=1,..,m}^{k+1} > \xi_{\max}^k$, or

3) $\varDelta^{k+1} > \varDelta^k \quad and \quad \xi_{i,\ i=1,..,m}^{k+1} < \xi_{\max}^k \quad and \quad \left| \frac{\varDelta^{k+1} - \varDelta^k}{\varDelta^k} \right| < \left| \frac{\xi_{i,\ i=1,..,m}^{k+1} - \xi_{\max}^k}{\xi_{\max}^k} \right|$

Rejected change: $\varDelta^{k+1} > \varDelta^k \quad and \quad \xi_{i,\ i=1,..,m}^{k+1} > \xi_{\max}^k$

In addition, the single and global deviations must be lower than a given “cut-off” value, based on both “statistical” and “experience based” considerations:

$$\varDelta^{k+1} < \varDelta_c \quad and \quad \xi_{i,\ i=1,..,m}^{k+1} < \xi_c$$

A predetermined number of interactions is performed (typically 10^5-10^6), then the best estimation for the spectrum parameters is obtained as the average of all “accepted parameters”.

Since ξ represents the deviation between calculated and measured sphere counts in units of standard deviation, it is reasonable to fix ξ_c=3. Moreover, $\varDelta$ is expected to be of the order of the number of degrees of freedom of the problem, i.e. the number of independent measurements, m, minus the number of parameters, 7. Anyway, since $\varDelta$ isn’t a Chi-square, a more realistic threshold value $\varDelta_c$ should be derived by experience. The fact that the convergence algorithm, presented here, relies on a “non Chi-square” global deviation term, $\varDelta$, finds its basis in the “robust convergence” theory (William, 1992).

6.5.3 *Performance and critical points of the MITOM code*

The MITOM code has been used by the UAB group since 2001, and various validation tests have been carried out in neutron fields at nuclear power plants or radionuclide sources. The results were always satisfactory (Bakali, 2001), (Thomás, 2004), within ±10% and ±5% accuracy in the estimation of the dose equivalent or the total neutron fluence respectively.

The MITOM code, however, could constitute a relevant barrier for some practical applications, where the capability to provide on-field quick results without a-priori information is essential. In order to improve these aspects, some "critical points" of the MITOM code have been examined.

The convergence process depends on the following aspects, most of them strictly related to predetermined numeric constants, the value of which cannot be changed during a given "run" of the code:

- The tolerance factor T_f;
- The cut-off values ξ_c and Δ_c;
- The number of iterations, *nps*;
- The guess parameter array, $\{x_j\}^0$.
- The "best estimation" is the average of all accepted parameters: this implies that a very careful choice of T_f, ξ_c, Δ_c and $\{x_j\}^0$ should be made in order to obtain a reasonable result in a limited number of interactions. If the choice is too "tolerant", then the solution could be very far from the real spectrum. If, on the other hand, the choice is too "exigent", a very small number of parameter arrays will pass the test, giving unreliable results. Therefore, the accuracy of the result depends on the quality of the a priori information, synthesized in $\{x_j\}^0$, and the experience of the user. A deep knowledge of the internal routines is also recommended to properly choose those quantities.
- The numerical format of the response functions and the input/output files isn't immediate and, in general, some work is required to assembly/interpret those files.

For the operative needs of a radiation protection group it would be preferable to have a "visual" code, where the input and output data have very simple format, the convergence procedure can be followed during the run and the "tolerance" can be interactively changed according to the progress of the "run". The user should be only asked to prepare a simple text file with the BSS readings, start and control the iterative process, move the tolerance parameter till a reasonable solution is reached. He shouldn't take care of the guess parameters. The format of the results should be suitable for direct exportation. The integral quantities as the average fluence to dose equivalent conversion factor, the fluence and dose equivalent averaged energy, should be automatically provided during the "run".

6.6 The FRUIT code

As mentioned in the previous paragraphs, the FRUIT code has been designed to fulfil the needs of an operative radiation protection group and to provide a suitable tool for the research activity in neutron dosimetry, as well.

The following features, in addition to those reported at the end of 6.5.3, have been implemented, taking advantage of the knowledge of the MITOM code and the facilities offered by the LabView (National Instruments) development environment:

- Rapid convergence to a meaningful solution and possibility to provide the results at the measurement site. This would help in either inter-comparison exercises or routine radiation protection measurements;

- The code should be user friendly and suitable to be used by either unfolding experts or technical personnel eventually in duty for routine measurements;

- The code should "visualize" the convergence procedure and allow the T_f, ξ_c and Δ_c parameters to be changed during the "run". This would imply a high degree of flexibility and strongly reduce the dependence of the results from $\{x_j\}^0$;

- No need of specific "a priori" information or "educated" guess spectra;

- Availability of simple routines to re-bin the spectra and/or the response functions and calculate the integral quantities (fluence averaged neutron energy, dose equivalent averaged neutron energy, ambient dose equivalent). Possibility to easily change the response functions if other detectors are used in the same BSS (gold foils, TLDs);

- Very simple formats for the input data (Bonner Sphere readings and $\{x_j\}^0$) and the result files (numerical spectrum, final parameter array, $\{x_j\}^{final}$).

6.6.1 The FRUIT *spectrum representation*

The FRUIT parameterization of the neutron spectra is basically the same as MITOM, with the following differences:

- the total neutron fluence is not included as unknown parameter in the unfolding procedure. The code normalizes all BS readings to a given sphere (e.g. the 8") and only works on unity spectra. The final solution is a unity spectrum, φ_j^{final}, from which the total neutron fluence may be obtained using the formula

$$\Phi_i = \frac{C_i}{f \cdot \sum_{j=1}^{N_g} R^*{}_{ij} \cdot \varphi_j^{final} \cdot \Delta E_j} \quad \text{i=1,..,m (number of spheres)} \qquad (6.12)$$

Using all the sphere readings, *m* estimations will be available. Their weighted average will provide the best estimation of the total fluence. The uncertainty on each Φ_i value is the quadratic composition of the uncertainties associated to C_i, f and the summation $\sum_{j=1}^{N_g} R^*{}_{ij} \cdot \varphi_j^{final} \cdot \Delta E_j$.

Thus, the parameters array in FRUIT is the following:

$$\{\mathrm{x}_\mathrm{j}\}_{j=1,..,7} = \{\alpha, \beta, \beta', b, P_t, P_f\}$$

The neutron spectrum calculation algorithm is based on the superposition of three independent LabView subroutines, to calculate φ_t, φ_e and φ_f. A relevant consequence is the possibility to easily replace the Watt spectrum with another function that, in a specific problem, could represent more adequately the fast neutron component of the spectrum. For example, as mentioned in 1.6.1, an "evaporation" function has been used to replace the Watt function to better describe the neutron spectra from a high energy accelerator:

$$\varphi_f(E)\ \alpha\ \frac{E}{T^2} \cdot e^{-\frac{E}{T}} \qquad (6.13)$$

Where the temperature parameter T varies in the range $0.5 < T < 1.5$ MeV. In this case, the FRUIT code would use the parameter T instead of α, whilst β would remain unused.

6.6.2 Input and output data

All numerical data in FRUIT have the format 0.0000E+00. The code requires the following input data:

- The Bonner Sphere counts: the user is asked to report the BS counts in a text file, sequentially, from the lowest (bare counter) to the highest diameter (12”+Pb). The file name is arbitrary. The relative uncertainty u_i , taking into account both the BS statistical uncertainty and the response function uncertainty, has to be inserted as well, directly in the LabView control panel. The count from a given sphere will not be used in the calculation if the correspondent uncertainty has been set to zero.

- The initial value of the parameter array: this file (parametri.txt) is filled with default values which have almost no influence on the final results. After the calculation, the final parameter values will be re-written on the same file. It is, therefore, recommended to save it with a different name after each “run”. Examples of the BS counts and parameter files are given in Figure 6.5.

BSS readings file

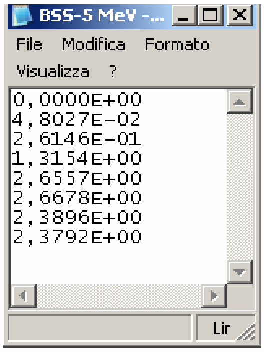

```
0,0000E+00
4,8027E-02
2,6146E-01
1,3154E+00
2,6557E+00
2,6678E+00
2,3896E+00
2,3792E+00
```

Parameters file

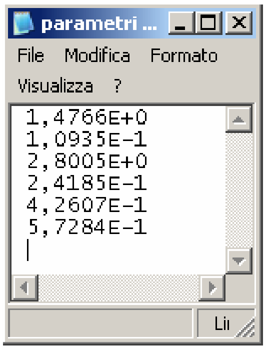

```
1,4766E+0
1,0935E-1
2,8005E+0
2,4185E-1
4,2607E-1
5,7284E-1
```

Figure 6.5: Examples of the BS counts file (on the left) and parameter file (on the right). The BS counts are ordered from the “bare detector” to the 12”+Pb sphere. The parameters are ordered as follows: $\left\{\alpha,\beta,\beta',b,P_t,P_f\right\}$.

The output spectrum will be a 116 lines text file, “best spectrum.txt”. The same format is used for the following “internal files”: the energy binning file, “Ecentrale.txt”, the energy interval file “deltaE.txt”, the BS response files, “bare.txt”, “2-pol.txt”, “3-pol.txt”, “5-pol.txt”, “8-pol.txt”, “10-pol.txt”, “12-pol.txt”, “12-pb.txt”, the fluence to ambient dose equivalent conversion coefficient file, “H-ICRP.txt”.

6.6.3 The calculation procedure

The spectrum parameters are determined according to the “robust convergence” criteria, as in MITOM (see 6.5.2). Anyway, some changes have been operated in order to make easier the convergence and reduce the dependence of the results on the quantities T_f, ξ_c, Δ_c and $\{x_j\}^0$. In particular, FRUIT allows changing the values of T_f, ξ_c and Δ_c during the run. Another relevant change is the mathematical formulation of the final solution: whilst in MITOM the best parameter array is the average of all accepted arrays, in FRUIT the solution is the limit of a convergent succession of parameters. This difference can be explained as follows.

MITOM doesn’t allow changing the convergence parameters during the run: the T_f, ξ_c and Δ_c values are pre-determined, their values have to be well chosen in order to obtain a reasonable solution. As a consequence, all accepted parameters will be reasonably “near” to the final solution. Some pre-runs of the code and a considerable experience are needed to make the appropriate selection.

Basic objectives of FRUIT are the independence of the results on the initial choices and the ability to find a satisfactory solution regardless the presence of specific a priori information. This implies that the first accepted solutions, usually very far from the true spectrum, will only serve to “move” the process to the vicinity of the solution. Under these hypothesis, the choice of a “limit” approach rather than an “average” approach, is expected to give more accurate results.

The FRUIT iterative process: the initial value of T_f is quite high (5%-10%, typically) in order to rapidly drive the process to the “vicinity” of the solution. At the same time ξ_c and Δ_c are set very high (100, for example), in order to accept all changes which improve the $\xi_{\max}$ and Δ values, regardless the “distance” to the final solution. The first ~10^4 interactions dramatically reduce $\xi_{\max}$ and Δ till almost “constant” values (10 and 50, for example) are reached. At this stage the user stops the calculation. The best parameters obtained, $\{x_j\}^{best}$, are accepted and the related $\xi_{\max}$ and Δ value automatically replace ξ_c and Δ_c. The user lowers T_f (to 1%, for example) and re-starts the process with the new ξ_c and Δ_c values. $\xi_{\max}$ and Δ will decrease and, again reach constant values. Again the user stops, replacing ξ_c and Δ_c with the $\xi_{\max}$ and Δ from the most recent solution. T_f is moved to 0.1%, and so on. During the run, the spectrum is dynamically visualized in an equilethargic plot. It is clear that the user has to follow the run, that can take few minutes.

Each time a new solution is accepted, the parameters are saved in “parametri.txt”, the spectrum is saved in “best spectrum.txt”, the calculated BS counts and the integral spectral values (fluence and dose equivalent averaged energy, average fluence to dose equivalent conversion factor) are displayed.

As a conclusion, the dependence of the results on the initial choices has been reduced. The final numerical spectrum and related parameters are provided in a simple text format. The program can be easily operated and controlled, using “common sense” criteria: if $\xi_{\max}$ and Δ are very “high”, the tolerance parameter T_f has to be high; as soon as $\xi_{\max}$ and Δ decrease, T_f can be reduced.
The performance of the code has been tested with neutron spectra from ISO standard sources. Chapter 7 is devoted to present these results.

Chapter 7

PERFORMANCE OF THE FRUIT UNFOLDING CODE

7.1 Performance evaluation criteria

In order to evaluate the accuracy of the FRUIT unfolding code, some performance tests have been performed, relying on the ISO standard neutron spectra plus a realistic "workplace" spectrum produced at the ENEA Bologna neutron calibration facility. The "conventionally true" numerical spectra were known from the ISO standard 8529-1 or from previous Monte Carlo calculations. For each spectrum, the "simulated" BS counts have been derived by applying the following equation:

$$C_i = f \cdot \Phi \cdot \sum_{j=1}^{N_g} R^*{}_{ij} \cdot \varphi_j \cdot \Delta E_j \qquad \text{i=1,..,m (number of spheres)} \qquad (7.1)$$

where Φ has been conventionally set to one. The BS counts have been unfolded with non-specific input parameters. Uncertainties on the BS counts have been set to ±3%, in agreement with the validation experiments shown in Chapter 5. The resulting spectrum has been graphically compared with the conventionally true one, and the following integral quantities have been derived and compared with their reference values:

- total neutron fluence, Φ;
- average fluence to ambient dose equivalent conversion factor, h^*_φ;
- fluence averaged energy, E_φ;
- ambient dose equivalent averaged energy, E_H;

Whilst E_φ and E_H have been chosen in order to control the "shape" of the unfolded spectrum, Φ and h^*_φ allows evaluating the accuracy of the unfolding code for the determination of the fluence and dose equivalent quantities.

The tests have been performed with the following neutron spectra:

- ^{241}Am-Be, ^{252}Cf and ^{252}Cf(D$_2$O) from ISO (ISO, 2001). In order to show the suitability of the FRUIT code to work with different model spectra than the Watt model, the ^{241}Am-Be spectrum has been also unfolded with an evaporation function.
- the total spectrum produced in the ENEA-Bologna calibration room, at 1 m from the

^{252}Cf($D_2$0) source (Bedogni, 2000). The spectrum, which includes a thermal neutron component, has been calculated with the MCNP ver. 4B Monte Carlo code.

7.2 ^{252}Cf source

The ISO and the unfolded spectra of the ^{252}Cf source are shown in Figure 7.1. The excellent agreement is due to the fact that the neutrons produced by spontaneous fission have a Watt energy distribution, which can be well described by the "fast" neutron component of the algorithm.

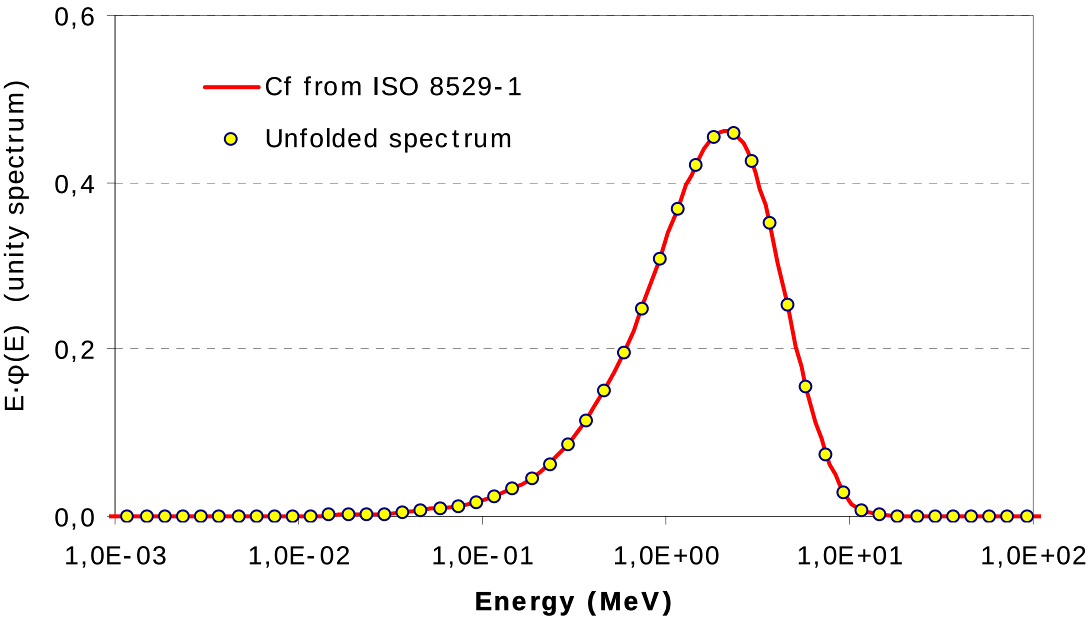

Figure 7.1: ISO reference spectrum and unfolded spectrum for the ^{252}Cf source (normalized to unity integral and in equilethargic representation).

The parameters describing the unfolded spectrum are reported in Table 7.1. It should be noticed that the values found for the α and β parameters (0.507 and 1.414 respectively) correspond well to those in the Watt equation for the ^{252}Cf theoretical spectrum (0.5 and 1.42) , taken from ISO 8529-1:

$$\varphi_{^{252}Cf}(E) = \frac{2}{\sqrt{\pi}\cdot(1.42)^{\frac{3}{2}}} E^{0.5}\cdot e^{-\frac{E}{1.42}} \qquad (7.2)$$

Parameter	Unfolded Value
α	0.507
β	1.414
β'	-
b	-
P_t	-
P_f	0.997

Table 7.1: Parameters describing the ^{252}Cf unfolded spectrum.

The integral quantities are reported in Table 7.2.

Quantity	Conventionally true value	Unfolded value	$\left\lvert\frac{Unfolded - true}{true}\right\rvert$
E_φ (MeV)	2.13	2.13	-
E_H (MeV)	2.3	2.3	-
Φ (cm^{-2}s^{-1})	1	1.001±0.002	0.1%
h_φ^* (pSv.cm^2)	385	384	0.3%

Table 7.2: Conventionally true and unfolded values of the integral quantities for the ^{252}Cf. The uncertainty on the total neutron fluence takes into account the variability of the fluence value obtained from each single sphere.

The results obtained with the ^{252}Cf spectrum are fully satisfactory, considering the dosimetric quantities as well as the shape of the spectrum.

7.3 ^{252}Cf(D$_2$O) source

The ^{252}Cf source, moderated in a 30 cm diameter heavy water sphere and covered by a 1 mm cadmium shell, is retained to be representative of a fission spectrum degraded by light shielding materials. The spectrum extends over seven orders of magnitude, with some discontinuities. The unfolding code is expected to correctly reproduce the “general” shape of the spectrum and provide accurate estimation of the integral quantities. Figure 7.2, Tables 7.3 and 7.4 show the results of the test.

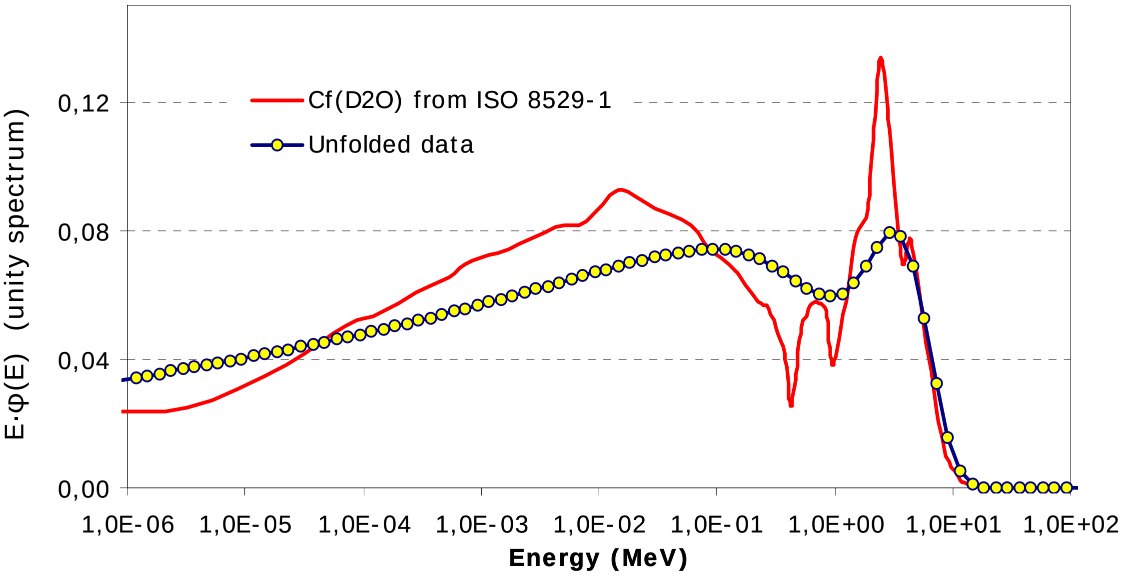

Figure 7.2: ISO reference spectrum and unfolded spectrum for the ^{252}Cf(D_2O) source (normalized to unity integral and in equilethargic representation).

In Figure 7.2 it can be observed that the unfolding code is able to correctly position the higher energy peak and also takes into account the secondary peak below 1 MeV. The epithermal component is overestimated below 100 eV and underestimated above 100 eV. Taking into account the complexity of the spectrum, the performance can be considered satisfactory. As far as the integral values are concerned, good results are obtained (Table 7.4).

Parameter	Unfolded Value
α	1.396
β	1.473
β’	1.123
b	$7.53 \cdot 10^{-2}$
P_t	0
P_f	$1.248 \cdot 10^{-1}$

Table 7.3: Parameters describing the ^{252}Cf(D_2O) unfolded spectrum.

Quantity	Conventionally true value	Unfolded value	$\left\lvert\frac{Unfolded - true}{true}\right\rvert$
E_φ (MeV)	0.55	0.55	-
E_H (MeV)	2.1	2.1	-
Φ (cm^{-2}.s^{-1})	1	0.996 ± 0.008	0.4%
h^*_φ (pSv.cm^2)	105	106	0.9%

Table 7.4: Conventionally true and unfolded values of the integral quantities for the ^{252}Cf(D_2O) source. The uncertainty on the total neutron fluence takes into account the variability of the fluence value obtained from each single sphere.

Also for the moderated ^{252}Cf source, the dosimetry related quantities are estimated with very high accuracy. As far as the shape of the spectrum is concerned, the performance of the code is adequate, taking into account the spectrum discontinuities. It should be noted that, even with some over- or under-estimations in the spectrum shape, the code conserves very well the fluence or dose equivalent averaged energy.

7.4 ^{241}Am-Be source

The ^{241}Am-Be source, due to its long life and the similarity of its energy distribution to the giant resonance spectrum, is usually employed to calibrate radiation protection devices to be used around particle accelerators. The spectrum shows several peaks and extends between 0.1 and 10 MeV. Figure 7.3 and Tables 7.5 and 7.6 show the results of the test.

Parameter	Unfolded Value
α	2.107
β	1.525
β'	1.860
b	$4.450 \cdot 10^{-1}$
P_t	0
P_f	$8.773 \cdot 10^{-1}$

Table 7.5: Parameters describing the ^{241}Am-Be unfolded spectrum.

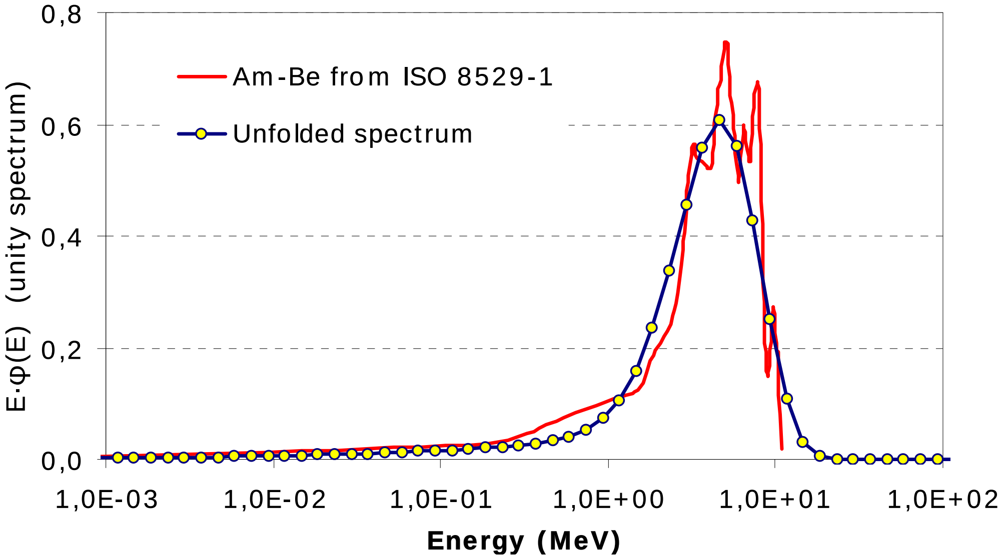

Figure 7.3: ISO reference spectrum and unfolded spectrum for the ^{241}Am-Be source (normalized to unity integral and in equilethargic representation).

As expected, the code isn't able to reproduce all discontinuities in the ^{241}Am-Be spectrum, but only their "average" behaviour. Concerning the spectrum shape related and dosimetry related integral quantities, the agreement is satisfactory.

Quantity	Conventionally true value	Unfolded value	$\left\lvert\frac{Unfolded - true}{true}\right\rvert$
E_φ (MeV)	4.16	4.26	2%
E_H (MeV)	4.4	4.5	2%
Φ (cm^{-2}s^{-1})	1	1.002 ± 0.002	0.2%
h^*_φ (pSv.cm^2)	391	391	-

Table 7.6: Conventionally true and unfolded values of the integral quantities for the ^{241}Am-Be source. The uncertainty on the total neutron fluence takes into account the variability of the fluence value obtained from each single sphere.

7.4.1 *Application of the "evaporation" version of the FRUIT code*

In order to show the suitability of the code to work with a generic model spectrum, the Am-Be spectrum has been also unfolded with an "evaporation" function. Although best results were expected with the more generic Watt model (described by 2 parameters), yet the evaporation fit also showed a satisfactory agreement, as shown in Figure 7.4 and Table 7.7. The parameters of the fit are reported in Table 7.8.

Quantity	Conventionally true value	Unfolded value	$\left\lvert\frac{Unfolded - true}{true}\right\rvert$
E_φ (MeV)	4.16	4.30	3%
E_H (MeV)	4.4	4.7	7%
Φ (cm^{-2}s^{-1})	1	1.001 ± 0.001	0.1%
h^*_φ (pSv.cm^2)	391	380	3%

Table 7.7: Evaporation model. Conventionally true and unfolded values of the integral quantities for the ^{241}Am-Be source. The uncertainty on the total neutron fluence takes into account the variability of the fluence value obtained from each single sphere.

Parameter	Unfolded Value
T	2.637
β'	1.930
b	$3.459 \cdot 10^{-1}$
P_t	0
P_f	$9.261 \cdot 10^{-1}$

Table 7.8: Evaporation model. Parameters describing the ^{241}Am-Be unfolded spectrum.

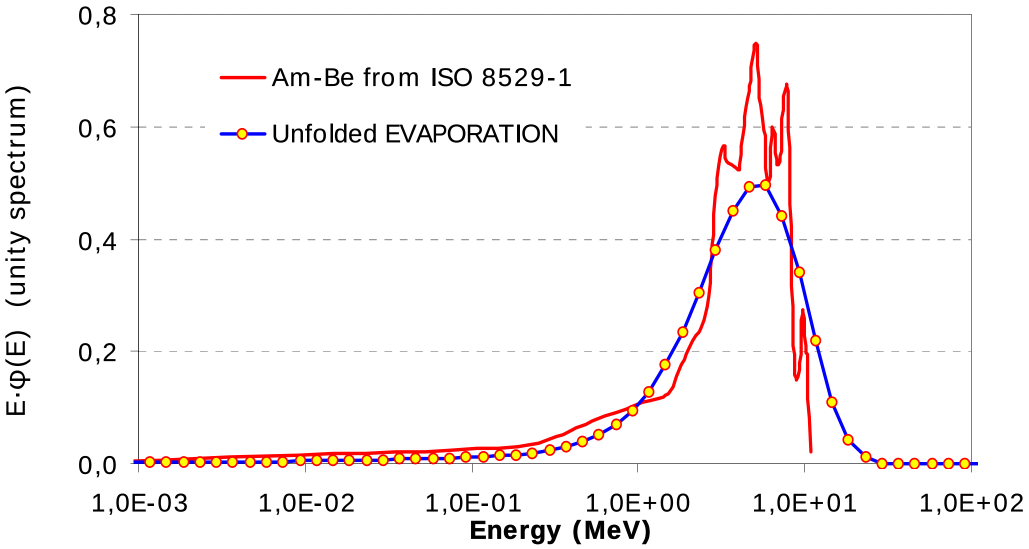

Figure 7.4: Evaporation model. ISO reference spectrum and unfolded spectrum for the ^{241}Am-Be source (normalized to unity integral and in equilethargic representation).

Satisfactory results have been obtained when the FRUIT code was used to unfold the Am-Be sphere counts with an evaporation model, obtaining satisfactory results. The loss of accuracy, with respect to the Watt model, is due to the fact that the evaporation spectrum is described by one parameter only.

7.5 Workplace spectrum

In order to evaluate the unfolding code in the thermal part of the spectrum as well, the total spectrum from the moderated ^{252}Cf source in a given point of the ENEA Bologna irradiation room has been considered. This test is supposed to be the most complex of all the validation exercises, since it adds a thermal component to the complex energy distribution of the moderated Cf source. The results are presented in Figure 7.5, Tables 7.9 and 7.10.

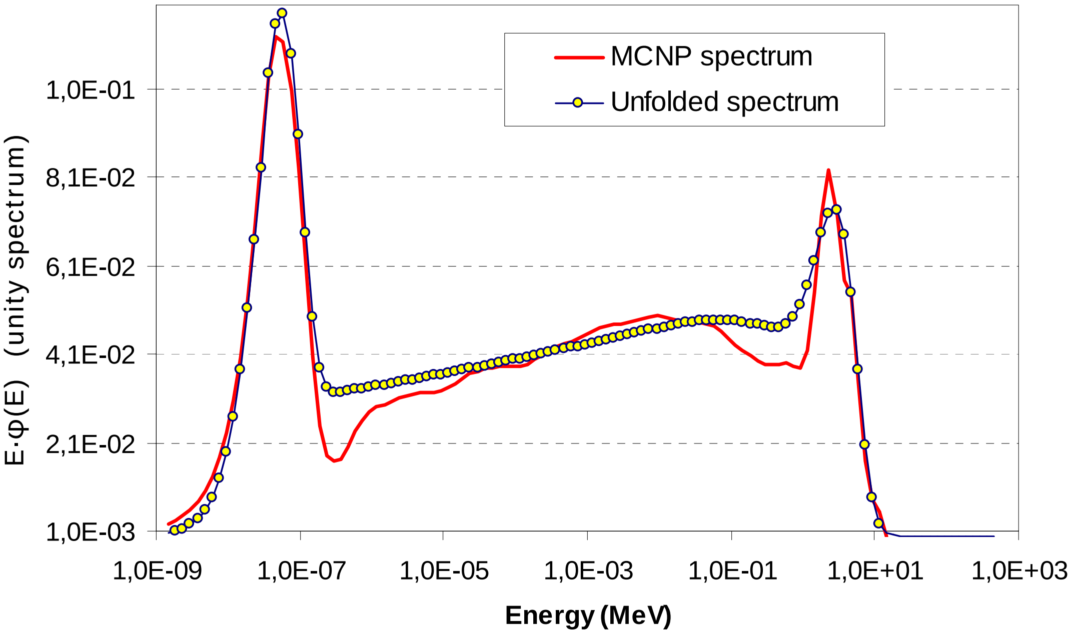

Figure 7.5: MCNP reference spectrum and unfolded spectrum for the workplace spectrum at the ENEA-Bologna neutron calibration room (normalized to unity integral and in equilethargic representation).

All the structures of the reference spectrum are adequately described by the unfolding code, including the thermal and epithermal parts.

Parameter	Unfolded Value
α	1.293
β	1.348
β'	1.712
b	$3.678 \cdot 10^{-2}$
P_t	$1.947 \cdot 10^{-1}$
P_f	$1.088 \cdot 10^{-1}$

Table 7.9: Parameters describing the ENEA-Bologna workplace unfolded spectrum.

Quantity	Conventionally true value	Unfolded value	$\left\lvert\frac{Unfolded - true}{true}\right\rvert$
E_φ (MeV)	0.43	0.43	0%
E_H (MeV)	2.0	1.9	5%
Φ (cm^{-2}s^{-1})	1	1.002 ± 0.005	0.2%
h_φ^* (pSv.cm^2)	86	89	3%

Table 7.10: Conventionally true and unfolded values of the integral quantities for the ENEA-Bologna workplace spectrum. The uncertainty on the total neutron fluence takes into account the variability of the fluence value obtained from each single sphere.

All the integral quantities, that take into account the spectrum shape and the dosimetry and field related properties, are adequately described by the unfolding code.

7.6 Accuracy in the evaluation of the integral quantities

In order to assess the accuracy of the unfolding code for correctly reproducing the spectrum shape, the neutron fluence and the dose equivalent, the approach followed in (Bakali, 2001) has been extended to the integral quantities: E_φ, E_H, Φ and h_φ^*. The Bologna workplace spectrum, which ranges over 10 orders of magnitude in energy, has been selected. The corresponding BS counts have been varied using a Gaussian perturbation with standard deviation 5%, which takes into account the accuracy of the response functions described in Chapter 5 (±3%) plus a typical statistic uncertainty of the BS counts (±3%). Ten sets of BS counts have been generated and unfolded, obtaining the following results.

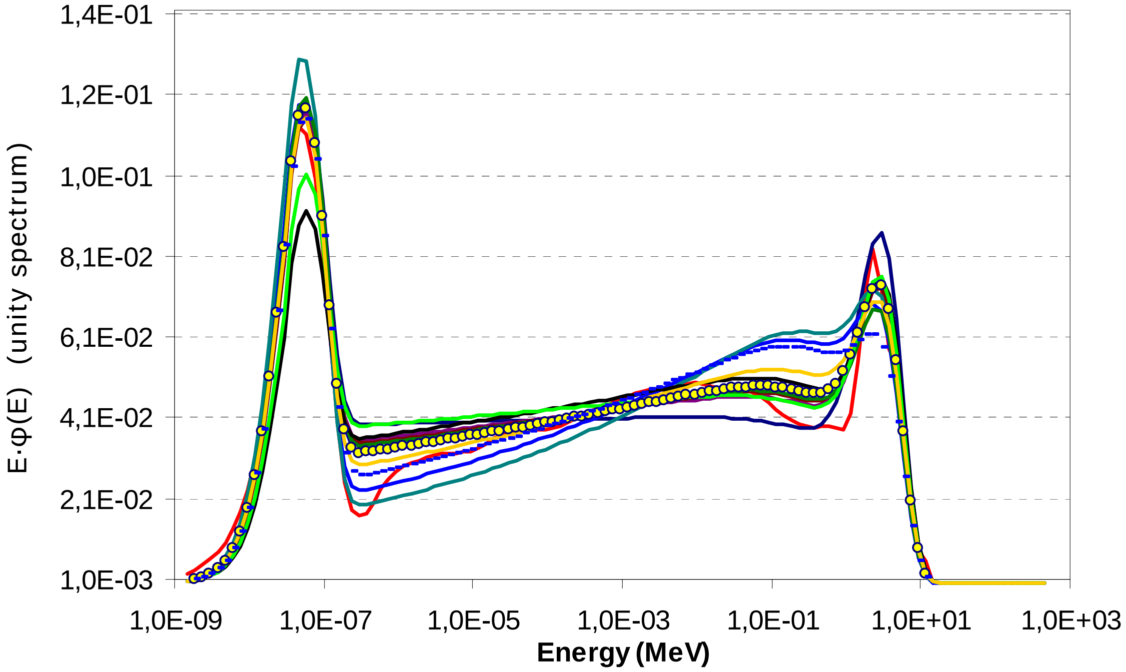

Figure 7.6: Variation of the unfolded spectrum when the BS counts are varied by applying a Gaussian perturbation with 5% standard deviation. Ten spectra are shown. (The spectra are normalized to unity integral and in equilethargic representation).

Table 7.11 reports the variability range (one standard deviation) of the four parameters when the BS counts are varied by applying a 5% Gaussian perturbation. Figures from 7.7 to 7.10 show, for each integral quantity, its variation as the BS counts are varied during the test.

Quantity	Variability range (1 σ)
E_φ	±8%
E_H	±8%
Φ	±3%
h^*_φ	±4%

Table 7.11: Variability range (one standard deviation) of the four integral parameters when the BS counts are varied by applying a 5% Gaussian perturbation.

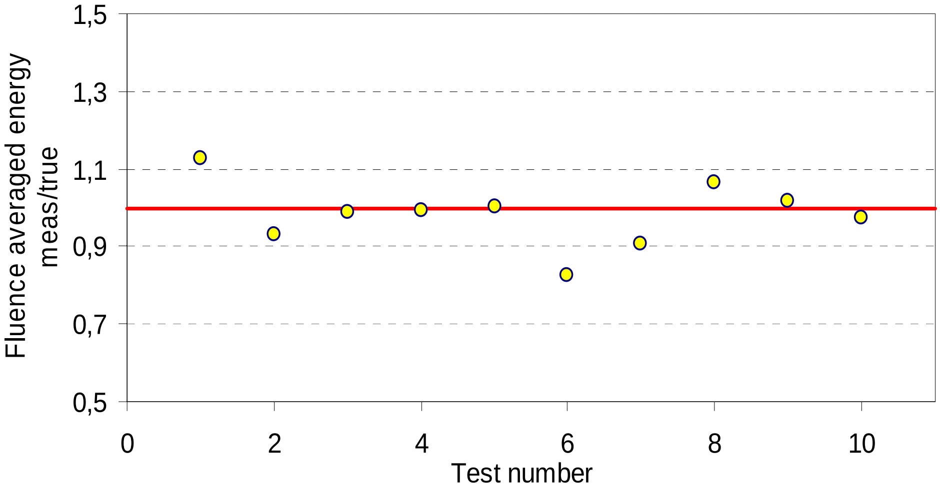

Figure 7.7: Fluence averaged neutron energy: variability during the test.

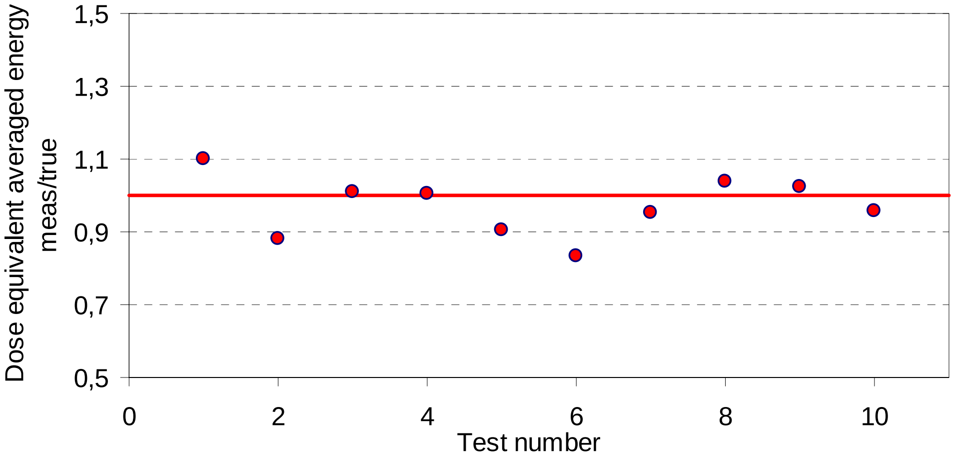

Figure 7.8: Dose equivalent averaged energy: variability during the test.

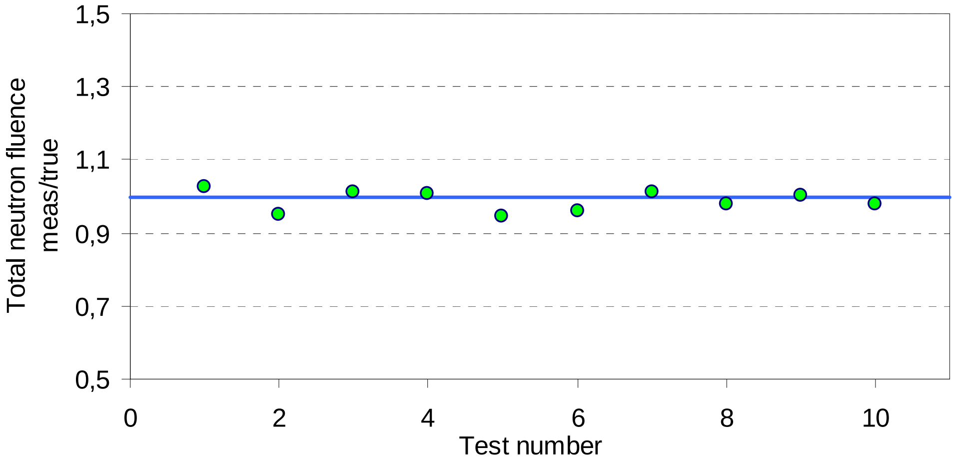

Figure 7.9: Total neutron fluence: variability during the test.

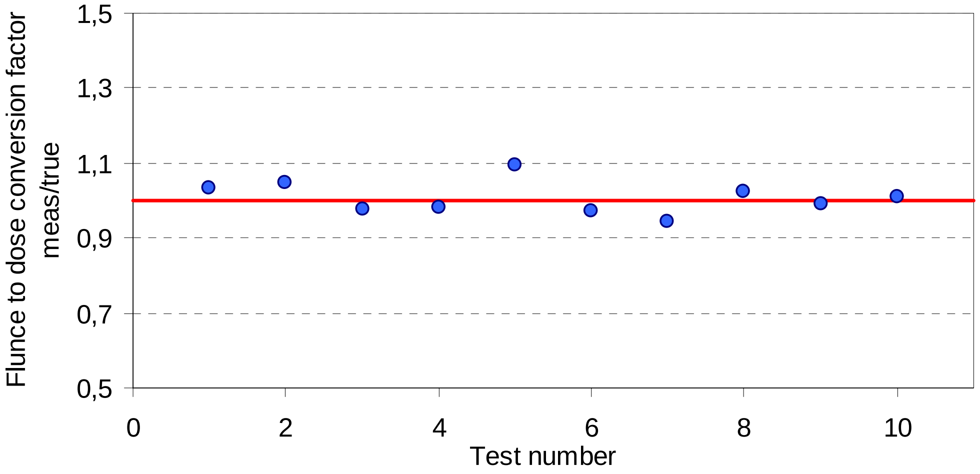

Figure 7.10: Fluence to Dose equivalent conversion coefficient: variability during the test.

From the results it can be deduced that the fluence and dose equivalent averaged energies show the highest variability (±8%), whilst the variability of the fluence to dose equivalent conversion factor is lower (±4%). The overall accuracy of the unfolding code for fluence evaluation can be typically evaluated as ±3%. For dose equivalent evaluations, the uncertainties on Φ and h_{φ}^{*} have to be combined, giving ±5%.

These figures are fully compatible with those found in literature. For example, the MITOM code allows estimating the dose equivalent and the fluence with ±10% and 2% uncertainties, respectively (Thomás, 2004). Relying on the past spectrometry inter-comparison exercises (Thomas D. J., 1997), it can be assumed that h_{φ}^{*} can be determined with ±15% uncertainty, in absence of a priori information. This figure can be reduced to ±5% when detailed a priori information are available (Gressier, 2004).

The results presented in this Chapter verified the accuracy of the FRUIT convergence procedures, allowing its use in unknown workplace neutron spectra.

Chapter 8

NEUTRON SPECTROMETRY AROUND THE DAΦNE e^+/e^- COLLIDER

8.1 **The Frascati accelerator complex**

8.1.1 *Overview*

The Frascati electron-positron collider, DAΦNE, is basically a high luminosity Φ factory, built after the decommissioning of ADONE in 1993 and operating since 1997. The complex, shown in Figures 8.1 and 8.2, is constituted by a 800 MeV electron/positron LINAC followed by an accumulator ring and finally a main ring. The three elements are connected via 180 m of transfer lines. The electron and positron beams can collide in two points, where the detectors KLOE (K LOng Experiment) and FINUDA (FIsica NUcleare a DAΦNE) are placed. In addition, the electrons from the LINAC can be directly driven to a Beam Test Facility (BTF), where detectors for high energy experiments can be tested. Moreover, a synchrotron light beam line, tangential to the main ring, is operating.

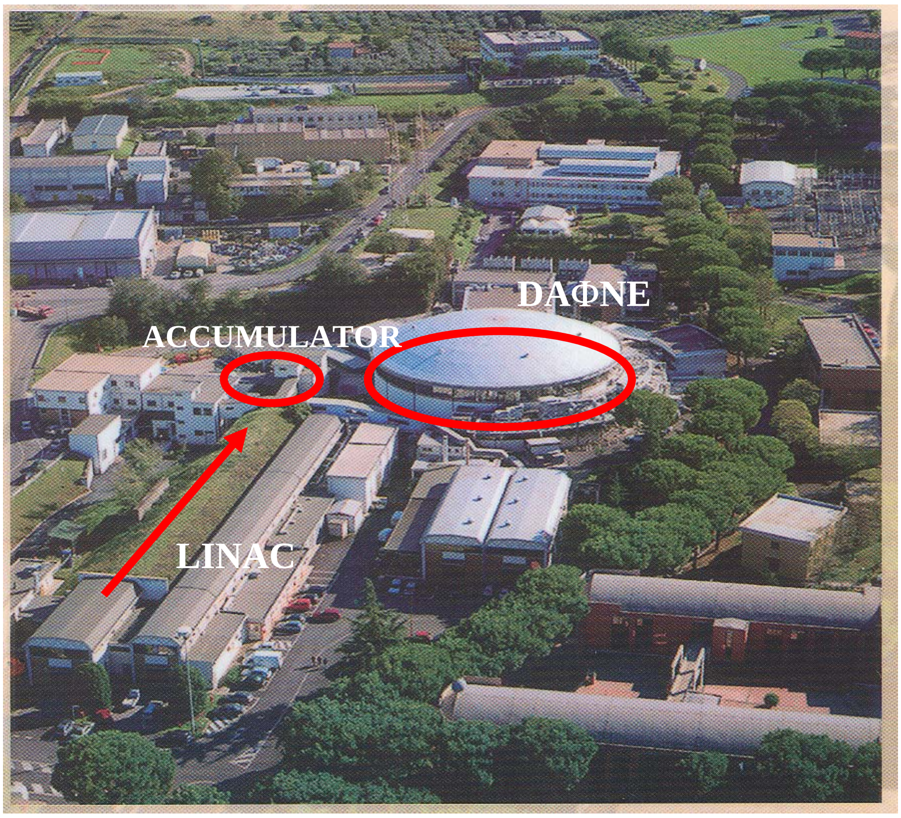

Figure 8.1: View of the INFN Frascati National Laboratories. The LINAC, accumulator and main ring buildings are highlighted.

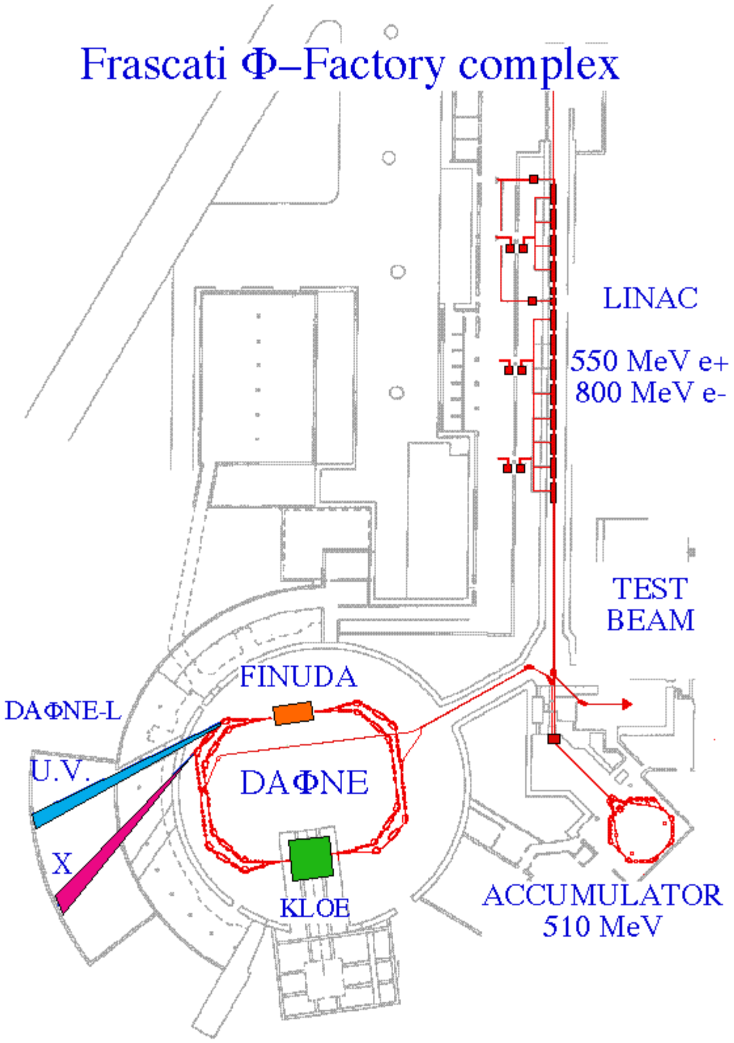

Figure 8.2: Layout of the Frascati accelerator complex.

The DAΦNE injection system has been designed to fill the required large amount of current in the Main Rings, around 1.5 A (electrons peak current) and 0.8 A (positrons peak current) in few minutes. The whole system runs at the operating energy of the collider (510 MeV per beam), so that the current decay can be compensated by refilling the rings on top of the already circulating current (this injection mode is called "topping up"). The particles are injected into DAΦNE according to the following sequence:

1) acceleration in the LINAC (10 ns pulses at 50 Hz);
2) injection into the Accumulator and stabilization of the bunch;
3) extraction towards main ring;

The points above are repeated for all bunches to be injected into the main ring. Then the LINAC is “switched” in order to produce the antiparticle bunches, which follow the same path. A typical time diagram of the currents in DAΦNE is shown in Figure 8.3.

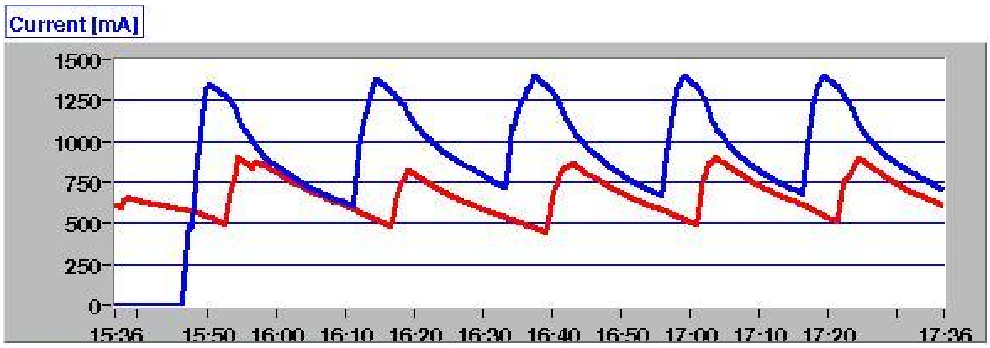

Figure 8.3: Typical time diagram of the electron/positron current in DAΦNE. The positron current is in red, whilst the electron current is in blue.

8.1.2 *The LINAC*

The 60 m long LINAC works at 2.865 GHz and is driven by four 45 MW klystrons. It delivers 10 ns pulses at a repetition rate of 50 Hz. A quadrupole based focusing system is distributed along the entire structure. A triode gun delivers up to 10 A electrons at 120 kV. The beam is then accelerated at 250 MeV by five 3 m long accelerating sections up to a removable target, where it is focused by a quadrupole system to a 1 mm radius spot to produce positrons with an efficiency of ~0.9%. The positrons are collected by a magnetic lens, separated from the electrons by means of a dipole based "chicane", and then accelerated up to a maximum energy of 550 MeV by 10 accelerating sections.

In the electron mode, the converter is removed from the beam and the electrons are accelerated through the whole structure up to a maximum energy of 800 MeV. The pulse current is 150 mA.

The accelerator usually operates at 510 MeV per beam.

8.1.3 *The accumulator ring*

The DAΦNE accumulator is a small quasi-octagonal storage ring with a total length of 32.5 m on the nominal trajectory. Its structure relies on the following magnetic elements, shown in Figure 8.4: four arcs, each constituted by two 45° dipole magnets, a quadrupole triplet and two sextupoles.

The electron beam coming from the LINAC is injected into the ring by means of a system of two magnets, the first bending the beam by 34° and the second performing the final deflection of 2°. The positron beam follows the opposite path. Two straight sections host the pulsed kicker magnets used to deflect the beam at injection and extraction and the R.F. cavity.

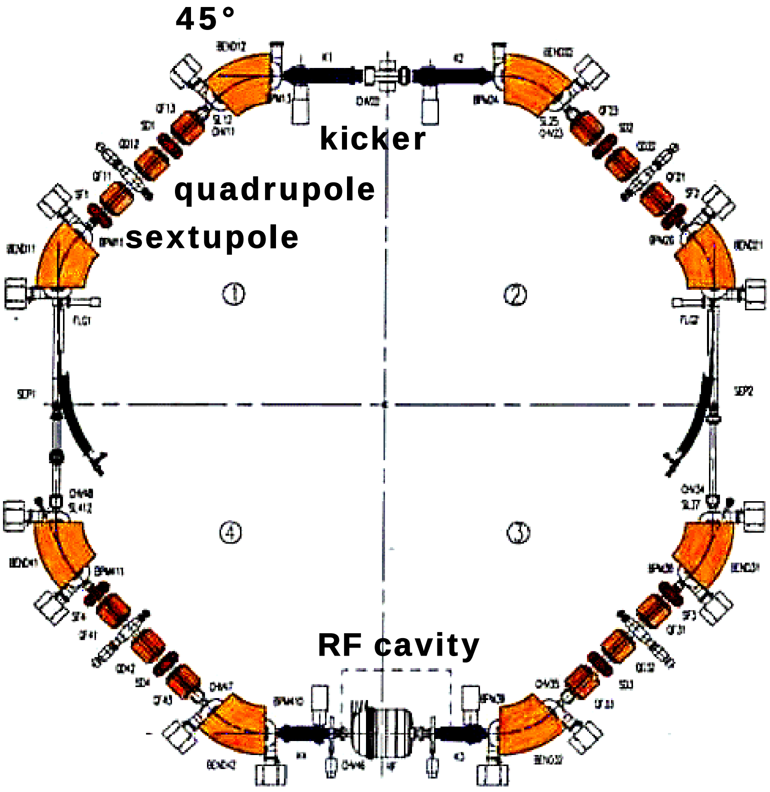

Figure 8.4: Structure of the accumulator ring.

8.1.4 *The DAΦNE main ring*

The main ring of DAΦNE, shown in Figures 8.5 and 8.6, occupies a 32.5 m x 23.3 m area and includes 216 magnets of 22 different kinds, including normal conducting electromagnets, superconducting solenoids and permanent magnet quadrupoles, powered by 290 independent power supplies.

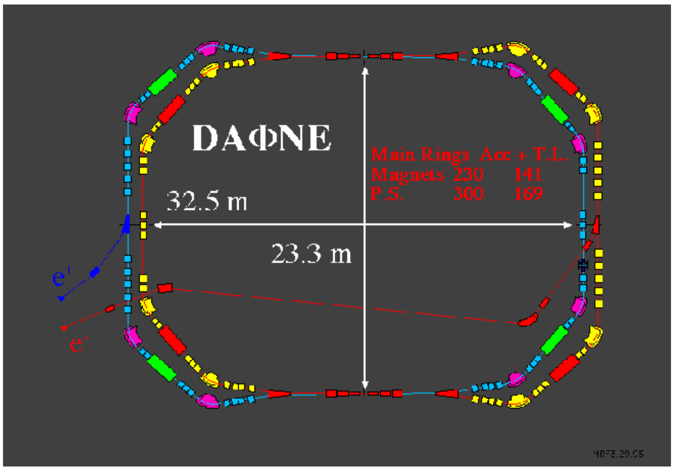

Figure 8.5: Structure of the DAΦNE main ring.

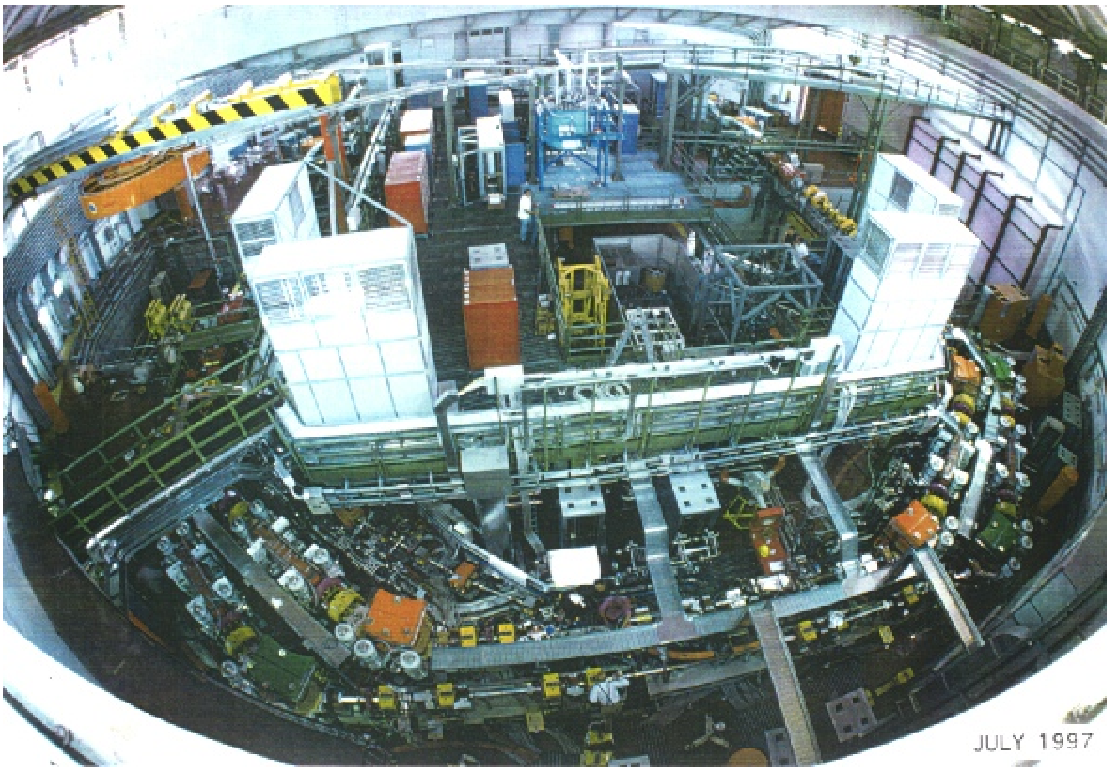

Figure 8.6: View of the DAΦNE main ring.

8.2 Selection of the points for measuring the neutron spectra

The LNF Radiation Protection Group is in charge of the radiation safety and the physical surveillance of the LNF. Environmental and individual radiation monitoring are routinely performed by means of active and passive dosemeters. The environmental dosimetry is based on a lattice of about 100 measurement points distributed around the DAΦNE accelerator complex, extending from the accelerator up to the boundary of the center. Each point is monitored by means of two TLD based dosemeters, one of which is processed by the LNF Radiation Protection Group, and the other from the ENEA-Bologna legal dosimetry service. The same double dosemeter system is used for the individual monitoring of the ``Category B" workers.

A network of active monitoring units, each formed by a rem-counter and an ion chamber, is also located around the DAΦNE accelerator complex. In case the instantaneous ambient dose rate exceeds a given threshold level in a given point, the corresponding unit provides an ``alarm signal" which immediately shuts down the accelerator.

In addition, a confirmatory monitoring with active neutron and gamma portable instruments is performed as well. Figure 8.7 shows the points where the confirmatory neutron and gamma monitoring is performed. Due to the thick concrete (1 m) + earth (4 m) shield, no external radiation is detected around the LINAC. The accumulator ring and the DAΦNE buildings are shielded with around 1 m of concrete. The weak point from the point of view of the radiation shielding is the non shielded upper window of the DAΦNE building (around 12 meters from ground), from which some skyshine radiation arises. For this reason the monitoring points are mainly located around this building. The area around the accumulator is also a potential source of ambient radiation, because of its injection sections and bending elements.

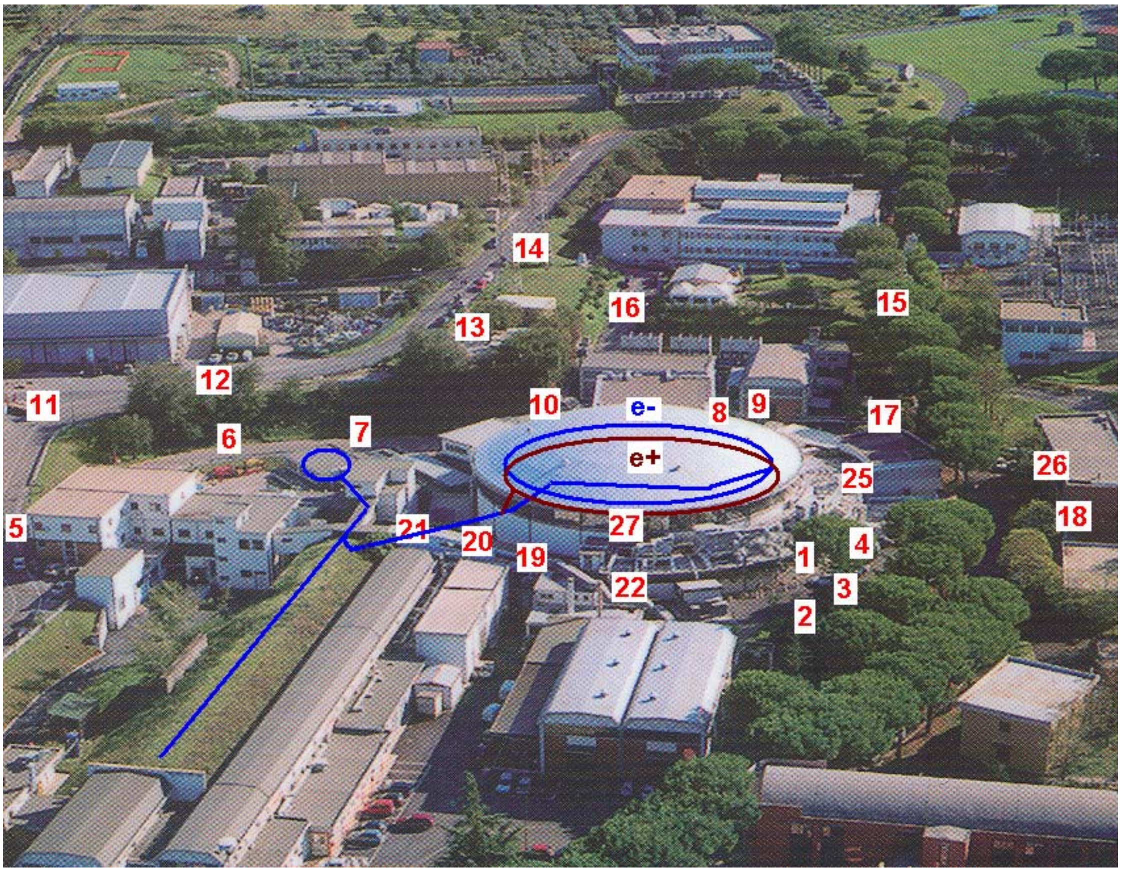

Figure 8.7: Location of the points of interest for the confirmatory neutron and gamma monitoring.

Table 8.1 shows the results of the neutron and photon monitoring performed during December 2005. For photons, an AUTOMESS 6150 AD-b instrument, properly calibrated in terms of $H^*(10)$, has been used. For neutrons, a Berthold LB6411 (see 2.4) calibrated in a ^{241}Am-Be field has been used. The instruments have been simultaneously employed in "integration" mode during the indicated time. The reported dose rate is the average value in the time interval, from which the natural background (measured in each point in August 2005 in "DAΦNE off" condition) has been subtracted. The instrumental reproducibility at the reported dose rate values can be evaluated as ±5% for both devices.

Monitoring point	Measurement time (h.min)	$H^*(10)$ photons ($\mu Sv \cdot h^{-1}$)	$H^*(10)$ neutrons ($\mu Sv \cdot h^{-1}$)
1	0.30	0.10	0.16
2	1.29	0.06	0.15
3	1.18	-	0.21
4	1.10	-	0.20
5	0.58	-	0.07
6	1.14	-	0.09
7	1.33	0.11	0.12
8	0.52	0.06	0.10
9	1.15	0.02	-
10	1.17	0.05	0.12
11	1.02	-	-
12	1.08	0.01	-
13	1.05	-	-
14	1.07	0.11	-
15	1.05	-	-
16	0.50	-	-
17	1.22	-	0.10
18	0.40	-	0.11
19	1.10	0.25	0.51
20	0.55	0.23	0.40
21	1.30	0.15	0.34
22	0.45	0.01	-
23	0.46	0.01	-
24	1.14	0.07	-
25	1.00	0.12	0.19
26	1.40	0.01	-
27	0.50	14.2	32

Table 8.1: Results of the neutron and photon confirmatory monitoring performed with an AUTOMESS 6150 AD-b for photons and a Berthold LB6411 for neutrons. Both instruments are calibrated in terms of $H^*(10)$. The reported quantities are average dose rates in the time interval from which the natural background has been subtracted. The instrumental reproducibility at the reported dose rates can be evaluated as ±5% for both devices. The missing data corresponds to values non distinguishable from the natural background. Data taken on December 2005.

On the basis of these results, the following relevant points have been identified and selected for neutron spectrometry measurements:

- Points 19, 20 and 21: placed along a corridor tangential to the DAΦNE building, nearly 4 m below the DAΦNE window. The points are directly facing the DAΦNE window at relatively short distance (15 meters). Here the neutron spectrum is expected to be highly thermalized, since mainly scattered neutrons can reach this point. Figures 8.8 and 8.9 illustrate the geometry of the corridor (point 20 has be chosen as representative of the area) with respect to the DAΦNE window.

Figure 8.8: Position of point 20 (inside the corridor). In the square: view from point 20 toward the accelerator.

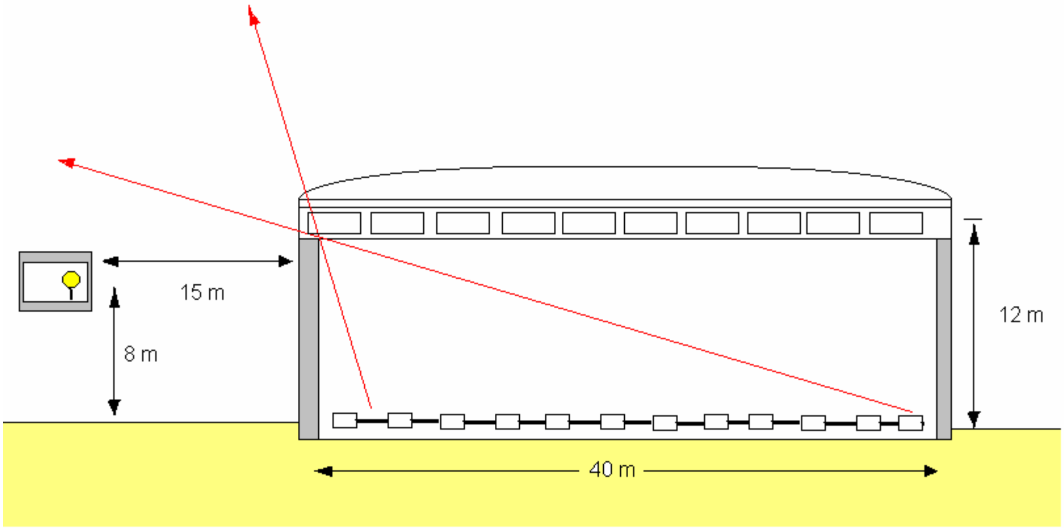

Figure 8.9: Geometry of point 20, represented inside the section of the corridor. Considering that the radiation source is uniformly distributed along the accelerator rings, no direct radiation can reach the point. The spectrum is expected to be composed by low energy scattered neutrons (shyshine effect).

- Point 25 has an identical geometry as point 20, but on the other side with respect to DAΦNE. This point is located inside a building, at around 5 m height from ground and around 8 m from the window.

- Point 27 is placed inside the DAΦNE building, in contact with the upper window. It faces directly the accelerator (from this point the Fig. 8.6 has been taken). Here the neutron spectrum is expected to cover the whole energy range included in the source term, from thermal up to 10^2 MeV.

Figure 8.10 shows the DAΦNE building. Here the position of point 27, inside the accelerator building in contact with the window, is marked.

Figure 8.10: DAΦNE building in a picture taken from point 18. Point 20 is on the left, 25 on the right. Point 27 is highlighted.

8.3 Neutron spectrometry measurements: experimental set up

The neutron spectra in the selected points around the DAΦNE complex have been measured with the BSS. The eight spectrometry configurations (0”, 2”, 3”, 5”, 8”, 10”, 12” and 12”+Pb) have been sequentially exposed in the measurement point, for approximately one day each. Since the neutron fluence rate from the accelerator shows a time variation, depending on a complex set of machine parameters, all BSS readings have been normalized to an independent monitor instrument. A rem counter ALNOR mod. 2002B, (see n. 1 in Figure 8.11), has been used as monitor instrument. Its reading (counts) will be also called “monitor units”, MU. Due to its geometry and dimension, the energy dependence of the ALNOR is similar to that of the 10” sphere. Its reproducibility, tested in a standard ^{241}Am-Be field, is ±1%.

Since each Bonner Sphere has been jointly exposed with the monitor instrument, the neutron fluence normalized to the monitor units (Φ, expressed in $cm^{-2} \cdot MU^{-1}$) in the measurement points has been precisely derived (uncertainties are in the order of ±3%). Then, a series of repeated measurements with the monitor instrument allowed the estimation of the average radiation output from the accelerator, i.e. the $MU.s^{-1}$ in a given point (this can be affected by large uncertainties, such as ±20%). The product of the two mentioned quantities provides the average neutron fluence rate, $\dot{\Phi}$ ($cm^{-2} \cdot s^{-1}$).

In the hypothesis that, during the spectrometric measurements (around one week), the neutron spectrum in a given point can only change in intensity, this normalization method allows a very accurate determination of the neutron energy distribution.

In order to verify the reproducibility of the neutron energy distribution in a given point, a series of simultaneous measurements with two devices showing different energy dependence has been performed. For this purpose, the ALNOR and the 2” sphere have been selected. The range of variability (1 standard deviation) of the ratio between the two readings is identified with the uncertainty due to the change in the neutron spectrum from the accelerator. Typical values are from ±4% to ±8%.

In addition, some complementary dosimetry measurements have been performed using the devices of Figure 8.11.

Figure 8.11: The monitor instrument (1) and the complementary devices used in the spectrometric / dosimetric measurements around the DAΦNE accelerator complex. The lead loaded LB6411-Pb (n. 3) is presented with only half lead shielding. The AUTOMESS 6150 AD-b (n.4) has been used to estimate the photon dose.

Also the complementary measurements have been normalized to the monitor instrument reading, in order to obtain comparable results. The rem counter Berthold LB6411 (n. 2 in Figure 8.11) and its lead loaded version, LB6411-Pb (n. 3), are routinely used for the radiation protection measurements around the DAΦNE complex, for the following reasons:

- the energy dependence of the LB6411 (Burgkhardt, 1997) is quite similar to that of the ICRP74 fluence to ambient dose equivalent conversion coefficient (ICRP, 1996 bis), see Figure 8.12. Taking advantage of the spectra measured around DAΦNE, workplace-specific calibration factors have been determined for this instrument.

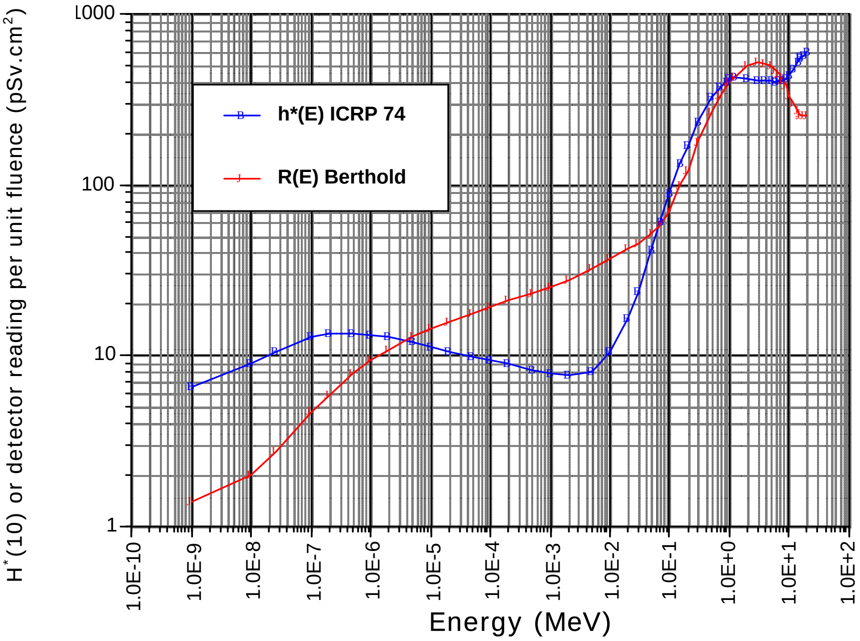

Figure 8.12: Energy dependence of the ICRP74 fluence to ambient dose equivalent conversion coefficient, H*(10)/ϕ, compared with the response of the LB6411 rem counter in terms of reading per unit fluence.

- The rem counter LB6411-Pb (n. 3, equipped with a 1 cm external lead shell) is a prototype from Berthold Technologies. Tests made at the CERF, the high energy neutron calibration facility of the CERN, showed that this instrument correctly follows the fluence to $H^*(10)$ conversion coefficient up to hundreds of MeV (Klett, 2005), whilst the response of the traditional LB6411 dramatically falls down above 20 MeV.

This instrument is routinely used to detect the presence of high energy neutrons in the workplace: as operational criterion, if the reading of the LB6411 and the LB6411-Pb are the same, within the uncertainties, then the presence of neutrons above 20 MeV can be neglected for radiation protection purposes.

- The photon dose rate meter, type AUTOMESS 6150 AD-b, has been used to complete the information on the radiation field. Measurements to evaluate the quality of the photon radiation around DAΦNE showed that the ambient dose equivalent averaged photon energy is around 250 keV (Bedogni, 2006b). Because the energy dependence of the AUTOMESS 6150 AD-b is almost flat above 100 keV, a calibration with a ^{137}Cs provides an adequate calibration factor for use around the accelerator.

8.4 Measurements in point 20

Point 20 has been monitored from 24/2/2006 till 28/2/2006 with the experimental assembly shown in 8.3. The Bonner Spheres or complementary devices have been sequentially positioned at the reference point, placed at 1.80 m height in front of the corridor’s window which faces the

DAΦNE window (see Figure 8.8). The monitor unit has been always in function. The results are shown in Table 8.2. The uncertainty on the BSS to Monitor instrument ratio, $\varDelta\left(\frac{C_i}{MU}\right)$, takes into account the ±3% accuracy of the BSS response function (Chapter 5), the statistical uncertainty on the counts and the uncertainty due to spectrum variability (±6%). The latter has been evaluated as the standard deviation of the ratio between the readings of the monitor unit and the 2” sphere, in a series of repeated measurements.

Sphere	C_i *(counts)*	MU *(counts)*	$\frac{C_i}{MU}$	$\varDelta\left(\frac{C_i}{MU}\right)$	$R_i^{unfolded}$ (cm^2)	$\varPhi_i$ (cm$^{-2}\cdot$MU^{-1})	$\frac{C_i}{MU}$ *unfolded/meas*
bare	2747	7760	0.35	±9%	0.0747	16.8	1.00
2”	3913	6390	0.61	±9%	0.1235	17.6	0.96
3”	1278	1536	0.83	±10%	0.1672	17.6	0.96
5”	2578	3754	0.69	±9%	0.1514	16.1	1.05
8”	2457	8014	0.31	±9%	0.0647	16.8	1.00
10”	2169	14697	0.15	±9%	0.0327	16.0	1.05
12”	476	6273	0.076	±11%	0.0160	16.8	1.00
12”+Pb	651	7050	0.092	±11%	0.0183	17.9	0.94

Table 8.2: Data from the BSS in point 20. The uncertainty term accounts for the statistical uncertainty on the counts, the ±3% accuracy of the BSS response matrix and the variability of the neutron energy distribution from the accelerator (±6%), evaluated as the standard deviation of the ratio between the monitor unit and the 2” sphere.

The $\frac{C_i}{MU}$ values have been used as input data for the unfolding program. The $\varDelta\left(\frac{C_i}{MU}\right)$ column has been used as uncertainty data. The unfolded spectrum (Figure 8.13) is highly thermalized with an endpoint at around 10 MeV. For each sphere, the unfolded response, $R_i^{unfolded}$, has been derived as follows:

$$R_i^{unfolded} = \sum_{j=1}^{N_g} R^*{}_{ij} \cdot \varphi_j^{unfolded} \cdot \varDelta E_j \qquad (8.1)$$

where $R^*{}_{ij}$ is the discrete version of the response function of the i-th sphere and $\varphi_j^{unfolded}$ is the unfolded spectrum normalized to unity integral. Then, the total neutron fluence normalized to the monitor unit, $\varPhi_i$, has been calculated from each sphere with the formula (8.2):

$$\varPhi_i = \frac{C_i}{f \cdot R_i^{unfolded}} \qquad (8.2)$$

Where f is the calibration factor of the spectrometer.

The best estimation for the total neutron fluence per monitor unit, Φ, has been derived as the weighted average of the Φ_i values, obtaining

$$\mathbf{\Phi = (16.9 \pm 0.6)\ cm^{-2} \cdot UM^{-1}}$$

As weighting factors, the inverse square of the uncertainties on the Φ_i have been used. The uncertainty on Φ (±3.5%) is the quadratic combination of the statistical contribution from the weighted average process (±3.3%) and the uncertainty on the calibration factor (±1.3%).

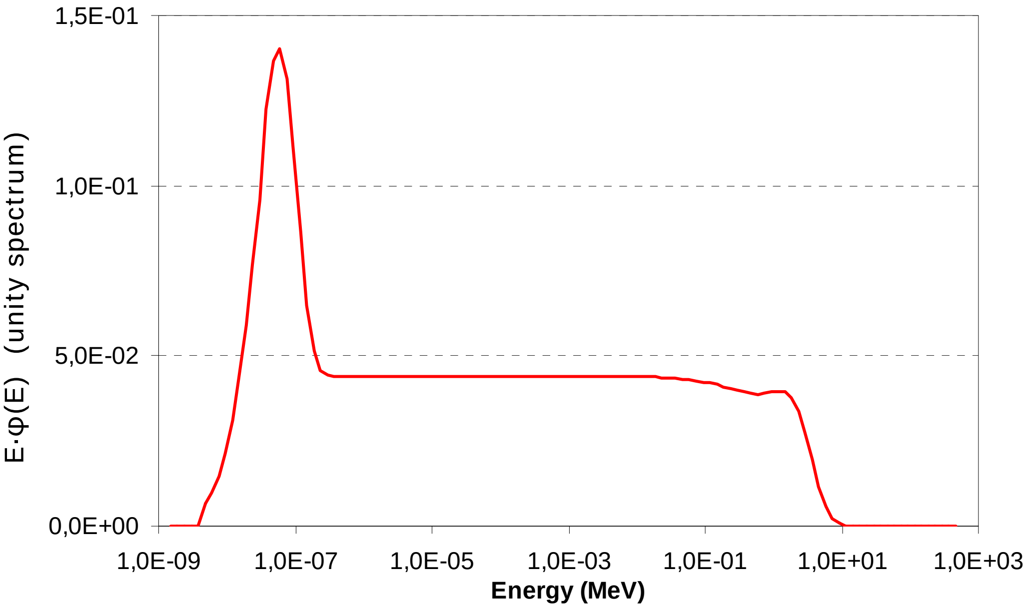

Figure 8.13: Neutron spectrum (normalized to unity integral and in equilethargic representation) measured in point 20 with the BSS.

The agreement between the unfolded and measured data is very good, since the maximum deviation is 5%, as shown in column 8 of Table 8.2 and in Figure 8.14.

In order to assess the average fluence rate and dose equivalent rate, the average value of monitor units per second has been calculated, obtaining

$$\text{Monitor unit rate} = \mathbf{0.108 \pm 0.016}\ \text{MU.s}^{-1}$$

The uncertainty (±15%) represents the time variability of the accelerator radiation output expressed as 1 sigma.

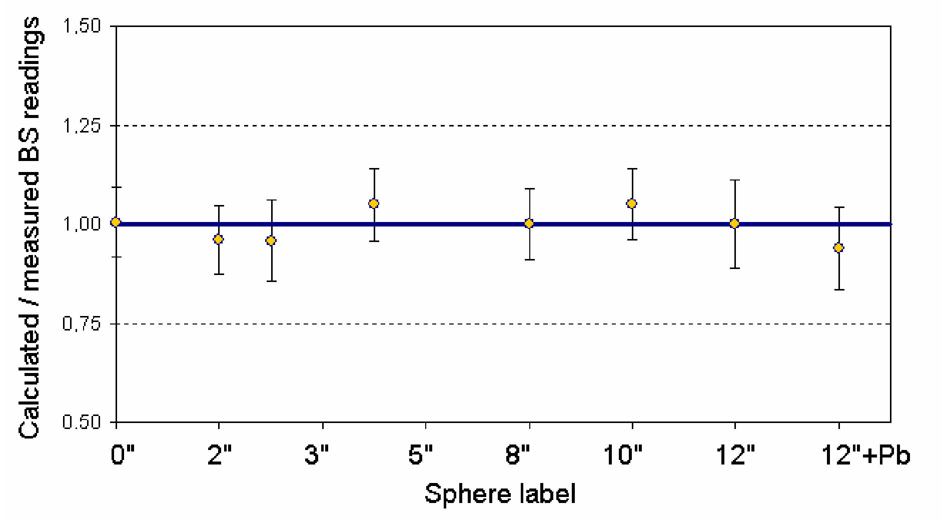

Figure 8.14: Ratio between the unfolded and the experimental BS readings.

Table 8.3 shows the field and dosimetric characteristics of point 20 derived by spectrometric measurements. The measurements from the complementary instruments are reported in Table 8.4.

Point 20: Spectrometric and dosimetric characteristics	
E_φ (MeV)	0.16
E_H (MeV)	1.1
h^*_φ (pSv.cm^2)	56
Φ (cm^{-2}.MU^{-1})	16.9±0.6
$H^*(10)^{norm}$ (μSv.MU^{-1})	(9.5±0.3)·10^{-4}
Monitor unit rate (MU.s^{-1})	0.108±0.016
$\dot{\Phi}$ (cm^{-2}.s^{-1})	1.8±0.3
$H^*(10)$ (μSv.h^{-1})	0.37±0.06

Table 8.3: Field and dosimetric characteristics of point 20, derived by spectrometric measurements. The superscript "*norm*" means that the quantity has been divided by the number of monitor units.

Point 20: complementary measurements	
$LB6411^{norm}$ (μSv.MU^{-1})	(8.2±0.4)·10^{-4}
$LB6411\text{-}Pb^{\ norm}$ (μSv.MU^{-1})	(8.5±0.4)·10^{-4}
$AUTOMESS^{norm}$ (μSv.MU^{-1})	(4.8±0.2)·10^{-4}

Table 8.4: Measurements taken with the LB6411, the LB6411-Pb and the AUTOMESS in point 20. The superscript "*norm*" means that the quantity has been normalized to the number of monitor units.

It should be noticed that the LB6411 underestimates the $H^{*}(10)$ value obtained from the unfolded spectrum. Namely, the LB6411/ $H^{*}(10)$ ratio is (0.86±0.05). This can be explained referring to the knowledge of the neutron spectrum and the energy dependence of the LB6411 response, in terms of reading per unit fluence.

The energy dependence of the LB6411 (Figure 8.12), in terms of reading per unit fluence, is well known by simulation and experimental validation (Burgkhardt, 1997) and available in the LB6411 technical sheet. By means of a calibration in a reference ^{241}Am-Be field, the published response has been adapted to the specimen in use at the LNF. Then it has been applied to the unfolded neutron spectrum in point 20 to obtain the expected LB6411 reading per unit fluence in that point.

The following procedures have been adopted:

- The energy response of the LB6411 in use at the LNF has been obtained by normalizing the published data with a ^{241}Am-Be calibration:

$$R^{LB6411-LNF}{}_{ij} = R^{LB6411-published}{}_{ij} \cdot \frac{R^{LB6411-LNF}_{Am-Be}}{R^{LB6411-pulished}_{Am-Be}} \qquad (8.3)$$

The $R^{LB6411-pulished}_{Am-Be}$ factor, calculated by integrating the published response function (enclosed in the instrument technical sheet) with the ISO ^{241}Am-Be spectrum, is 442 pSv.cm^2.

The $R^{LB6411-LNF}_{Am-Be}$ has been calculated as the ratio of the $h^{*}_{\varphi-AmBe}$ average conversion coefficient (391 pSv.cm^2) and the LB6411-LNF calibration factor, N_{Am-Be} = (1.05 ± 0.05) (measured at both the LNF and the ENEA-Bologna neutron calibration rooms), namely $R^{LB6411-LNF}_{Am-Be}$ = 391/1.05 = 372 pSv.cm^2. Then, the LNF to literature normalization factor is F_{norm} = 372 / 442 = 0.84.

- At this stage, it is possible to calculate the “expected” LB6411 reading per unit fluence in point 20:

$$R^{LB6411-LNF}_{point\,20} = F_{norm} \cdot \sum_{j=1}^{N_g} R^{LB6411-published}{}_{ij} \cdot \varphi^{unfolded}_{j} \cdot \Delta E_{j} \qquad = 48.9 \text{ pSv.cm}^2 \qquad (8.4)$$

- Thus, the “expected” LB6411/ $H^{*}(10)$ ratio is $R^{LB6411-LNF}_{point\,20}$ / h^{*}_{φ} = 48.9 / 56 = 0.87, which is fully compatible with the measured ratio, 0.86. The LB6411 workplace specific calibration factor in point 20 is therefore

$$N_{20} = (H^{*}(10) / \text{LB6411})_{\text{point 20}} = 1.16 \pm 0.06$$

The LB6411 and its lead loaded version provide comparable results, taking into account the uncertainties. Other methods should be used in order to investigate the presence of high energy neutrons. This is explained in 8.4.1.

8.4.1 Investigation on the presence of high energy neutrons

The experimental data obtained in point 20 have been unfolded with the FRUIT code, using a model spectra algorithm that relies on the superposition of three components: thermal, epithermal and a Watt spectrum. Of course, this excludes the possibility to detect neutrons above 20 MeV. The unfolded data for point 20 agree, within the uncertainties, with the "Watt" model, as shown in Figure 8.14.

Anyway, the presence of high energy neutrons, produced via pseudo-deuteron and photo-pion effects, should not be excluded. The 12"+Pb sphere is crucial for this kind of analysis, because is the only detector of the BSS with relevant response in the 10^2 MeV region.

Literature spectra, measured around similar accelerators, suggest the presence of high energy neutrons:

- A "high energy tail", was measured with BSS around the SLAC 2.3 GeV electron booster synchrotron (Vylet, 1997);
- The photo-neutron spectrum calculated with FLUKA around the facility SRRC, a 1.5 GeV electron booster synchrotron (Taiwan), shows an evaporation shaped peak at around 100 MeV (Sheu, 2003);
- The photo-neutron spectra produced by a thick Pb target bombarded with 1.2 and 2.0 GeV electrons, at KEK and at the Pohang Accelerator Laboratory (Korea), were measured with the TOF method. Neutrons up to 200 MeV have been observed (Ban, 2000).

In order to investigate such hypothesis, an unfolding model with an evaporation spectrum + high energy peak has been introduced into the FRUIT code, providing a new version where the spectrum is described by seven parameters:

T: the Temperature parameter of the evaporation spectrum;
T_{high}: the Temperature parameter of the high energy peak;
β', b: parameters describing the intermediate neutrons, as in MITOM;
P_t: fraction of thermal neutrons;
P_e: fraction of intermediate neutrons;
P_f: fraction of evaporation neutrons;
P_{high}: fraction of high energy neutrons.

To complete the comparison, a simple evaporation model (P_{high} = 0) has been also applied. Finally, the measurements taken in point 20 have been unfolded with three versions of the FRUIT code: Watt model, simple evaporation model, evaporation + high energy model. In all cases, the quantities h_{φ}^{*}, Φ and the "fit" parameters of the code, Δ (global deviation) and ξ^{max} (maximum sphere deviation), have been recorded. Table 8.5 summarizes the results, including additional information on the fractions of fluence and dose equivalent above 10 MeV.

Quantity	Watt	Simple evaporation	Evaporation + high energy
h_{φ}^{*} (pSv.cm^2)	56	60	58
Φ (cm^{-2}.MU^{-1})	16.9 ± 0.6	17.1 ± 0.6	17.0 ± 0.6
Fluence below 0.4 eV	32%	33%	31%
Fluence above 10 MeV	-	-	1%
H(10)* above 10 MeV	-	-	6%
Δ	2.56	3.98	2.03
ξ^{max}	0.56	0.91	0.54

Table 8.5: Point 20: comparison of three different unfolding models.

According to the value of the convergence parameters, the high energy model provides the best fit. On the other hand, the three models provide the same value of neutron fluence. Also the variability of the fluence to dose equivalent conversion coefficient is limited (the standard deviation of the three h_{φ}^{*} values is ±3%), if compared with the uncertainties on the initial data (around ±10%).

Nevertheless, physical considerations related to the pseudo-deuteron and the photo-pion effects, together with the literature data, suggest that a high energy component should be present in the spectrum.

As far as the experimental results are concerned, the modified high energy unfolding model minimizes the convergence parameters Δ and ξ^{max}, because it allows a better interpretation of the 12"+Pb result.

The high energy peak, located at around 100 MeV, provides 1% of the fluence and 6% of the ambient dose equivalent. Figure 8.15 compares the "simple" Watt model with the high energy model.

It is clear that the introduction of a high energy unfolding model is not crucial in this measurement point, because large shields are interposed between the accelerator and the measurement point.

Nevertheless, the new high-energy version of the FRUIT code provides interesting results, which are fully in agreement with the literature data and the relevant physical phenomena. This code is expected to give even more promising results in those points that are directly exposed to the photo-neutron source, such as point 27.

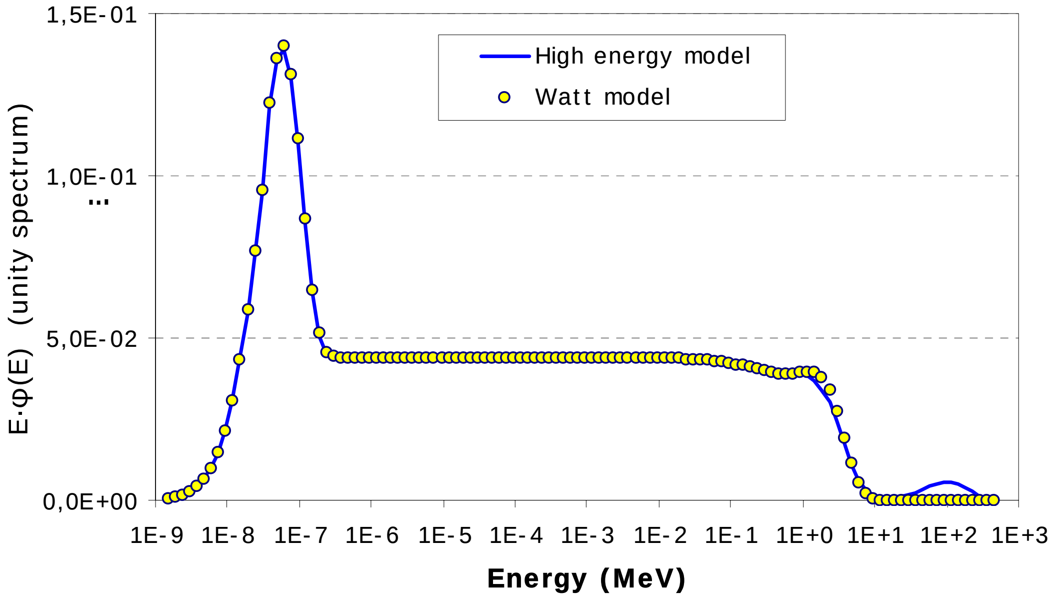

Figure 8.15: Neutron spectrum measured in point 20 (normalized to unity integral and in equilethargic representation), unfolded with a Watt model and an evaporation+high energy model.

8.5 Measurements in point 25

Point 25 has been monitored from 11/11/2005 till 20/11/2005 with the experimental assembly shown in 8.3. The Bonner Spheres or complementary devices have been sequentially positioned at the point of test, placed at a height of 1.70 m in front of a window from which the DAΦNE upper window was visible. This point is located along the direction of the positron and electron injection septa in DAΦNE. In addition, with respect to point 20, it's closer to the accelerator. Thus, the ratio between transmitted and skyshine component is expected to be higher than in point 20.

The experimental results are shown in Table 8.6. The uncertainties affecting the BSS to Monitor instrument ratio, $\Delta\left(\frac{C_i}{MU}\right)$, take into account the ±3% accuracy of the BSS response function (Chapter 5), the statistical uncertainty on the counts and the variability of the energy distribution from the accelerator (±4%). The latter has been evaluated as the standard deviation of the ratio between the monitor unit and the 2" sphere, obtained in a series of repeated measurements.

Sphere	C_i *(counts)*	MU *(counts)*	$\frac{C_i}{MU}$	$\Delta\left(\frac{C_i}{MU}\right)$	$R_i^{unfolded}$ (cm^2)	Φ_i (cm^{-2}·MU^{-1})	$\frac{C_i}{MU}$ *unfolded/meas*
bare	1832	6306	0.29	±7%	0.0834	12.3	1.00
2”	3292	7406	0.44	±7%	0.1228	12.8	0.96
3”	1718	3318	0.52	±8%	0.1572	11.7	1.05
5”	1841	3522	0.52	±8%	0.1367	13.6	0.91
8”	907	4225	0.21	±8%	0.0619	12.3	1.00
10”	492	3608	0.136	±9%	0.0343	14.1	0.87
12”	958	16158	0.059	±8%	0.0188	11.2	1.10
12”+Pb	408	5155	0.079	±10%	0.0228	12.3	1.00

Table 8.6: Data from the BSS in point 25. The uncertainty term accounts for the statistical uncertainty on the counts, the ±3% accuracy of the BSS response matrix and the variability of the neutron energy distribution from the accelerator (±4%), evaluated as the standard deviation of the ratio between the monitor unit and the 2” sphere.

As usually, the spectrum has been derived using three different models:

1) Simple Watt model
2) Evaporation model
3) Evaporation model + high energy peak.

Only the best fit, obtained with model n. 3, is reported in Figure 8.16. Table 8.7 summarizes the spectral parameters provided by the three versions of the unfolding code.

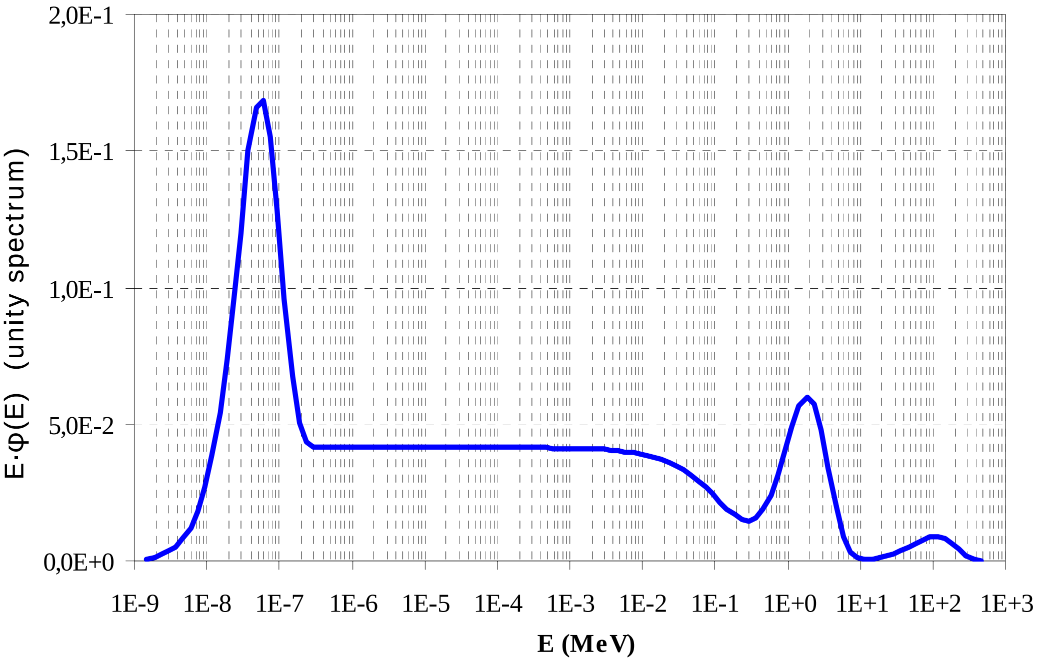

Figure 8.16: Neutron spectrum measured in point 25 with the BSS (Normalized to unity integral and in equilethargic representation).

Quantity	Watt	Simple evaporation	Evaporation + high energy
h^*_φ (pSv.cm^2)	56	58	63
Φ (cm^{-2}.MU^{-1})	12.5 ± 0.4	12.3 ± 0.4	12.4 ± 0.4
Fluence below 0.4 eV	37%	37%	37%
Fluence above 10 MeV	-	-	1.6%
H(10)* above 10 MeV	-	-	8.6%
Δ	6.00	5.90	5.20
ξ^{max}	1.70	1.45	1.38

Table 8.7: Point 20 - comparison of three different unfolding models.

As expected, the giant resonance peak is more evident than in point 20. Only 1.6% of the fluence is comprised in the high energy peak, but the associated ambient dose equivalent fraction is 9%, due to the high value of the fluence to dose equivalent conversion coefficient in that energy range.

The ratio between the calculated and measured BS counts is shown in Figure 8.17.

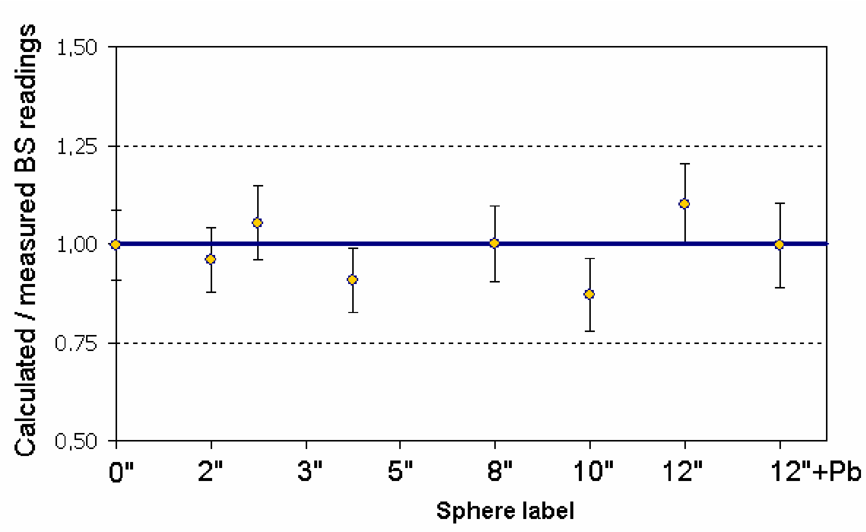

Figure 8.17: Point 25: ratio between the unfolded and the experimental BS readings.

The best estimation for the total neutron fluence per monitor unit, Φ, has been derived, from the high energy model, as the weighted average of the Φ_i values, obtaining

$$\mathbf{\Phi = (12.4 \pm 0.4)\ cm^{-2} \cdot UM^{-1}}$$

As weighting factors, the inverse square of the uncertainties on the Φ_i have been used. The uncertainty on Φ, ±3.1%, is the quadratic combination of the statistical contribution from the weighted average process (±2.8%) and the uncertainty on the calibration factor (±1.3%).

The measurements in point 25, in terms of fluence, ambient dose equivalent and complementary measurements are summarized in Table 8.8.

Point 25: summary of the results	
Φ (cm^{-2}.MU^{-1})	12.4 ± 0.4
Monitor unit rate (MU.s^{-1})	0.070 ± 0.017
$\dot{\Phi}$ (cm^{-2}.s^{-1})	0.87± 0.21
$H^*(10)$ (μSv·h^{-1})	0.20 ± 0.05
$H^*(10)^{norm}$ (μSv.MU^{-1})	$(7.8\pm0.2)\cdot10^{-4}$
$LB6411^{norm}$ (μSv.MU^{-1})	$(7.1\pm0.4)\cdot10^{-4}$
$LB6411\text{-}Pb^{\ norm}$ (μSv.MU^{-1})	$(7.5\pm0.4)\cdot10^{-4}$
$AUTOMESS^{norm}$ (μSv.MU^{-1})	$(6.6\pm0.3)\cdot10^{-4}$

Table 8.8: Summary of the field and dosimetric quantities in point 25, obtained with the BSS and the complementary instruments. The superscript "*norm*" means that the quantity has been divided by the number of monitor units.

Also in this case, the ratio between the LB6411 reading and *H*(10)*, 0.91, is justified by the spectrum shape and the instrument response. The unfolded spectrum applied to the literature LB6411 response (supposed null above 20 MeV), yields 63 pSv·cm^2. Since the LNF to literature LB6411 normalization ratio is 0.84, the LNF instrument should have responded 0.84 * 63 pSv·cm^2 = 53 pSv·cm^2, whilst the unfolded h^*_φ value (below 20 MeV) is 58 pSv·cm^2. The expected LB6411 underestimation factor is then 53/58 = 0.91, which agrees with the measured ratio.

The LB6411 workplace specific calibration factor in point 25 is

$$N_{25} = (H^*(10)\ /\ \text{LB6411})_{\text{point 25}} = 1.10\pm0.06$$

Again the uncertainties on the LB6411 and its loaded version don't allow detecting the presence of high energy neutrons, which represent only 1.6% of the total fluence.

8.6 Measurements in point 27

Point 27 has been monitored from 9/12/2005 till 12/12/2005 with the experimental assembly shown in 8.3. The Bonner Spheres or complementary devices have been sequentially positioned at the reference point, placed at the medium height of the DAΦNE window. This point is inside the accelerator building and directly watches to the main ring. Here the highest dose rate and the hardest spectrum are expected. A relevant 100 MeV neutrons fraction is also expected.

Due to a power supply fault, the 12” measurement was lost. It wasn’t possible to repeat it, due to access problems.

The experimental results are shown in Table 8.9. The uncertainties on the BS to Monitor unit ratio takes into account the ±3% accuracy of the BSS response function (Chapter 5), the statistical uncertainty on the counts and the variability related to the energy distribution from the accelerator (±7%).

Sphere	C_i *(counts)*	MU *(counts)*	$\frac{C_i}{MU}$	$\Delta\left(\frac{C_i}{MU}\right)$	$R_i^{unfolded}$ (cm^2)	Φ_i (cm^{-2}·MU^{-1})	$\frac{C_i}{MU}$ *unfolded/meas*
bare	40657	79780	0.51	±8%	0.0629	28.7	1.00
2”	22029	29638	0.74	±8%	0.0820	32.1	0.89
3”	8407	9340	0.90	±9%	0.1208	26.4	1.09
5”	14205	12563	1.13	±9%	0.1561	25.7	1.12
8”	105137	130177	0.81	±8%	0.0996	28.7	1.00
10”	62966	147203	0.43	±8%	0.0584	26.0	1.11
12”	-	-	-	-	-	-	-
12”+Pb	46448	136140	0.34	±8%	0.0421	28.8	1.00

Table 8.9: Data from the BSS in point 27.

The spectrum has been derived using three different models: Watt, evaporation and evaporation + high energy. The latter, considered as the best fit, is reported in Figure 8.18. Table 8.10 summarizes the spectral and convergence parameters provided by the three versions of the unfolding code.

The best estimation for the total neutron fluence per monitor unit, Φ, has been derived, from the high energy model, as the weighted average of the Φ_i values, obtaining

$$\boldsymbol{\Phi = (27.8 \pm 1.0)\ \mathrm{cm}^{-2}\cdot\mathrm{UM}^{-1}}$$

As weighting factors, the inverse square of the uncertainties on the Φ_i have been used. The uncertainty on Φ is the quadratic combination of the statistical contribution from the weighted average process (±3.2%) and the uncertainty on the calibration factor (±1.3%).

Quantity	Watt	Evaporation	High energy
h^*_φ (pSv.cm^2)	124	122	155
Φ (cm^{-2}.MU^{-1})	28.1 ± 1.0	28.3 ± 1.0	27.8 ± 1.0
Fluence below 0.4 eV	30%	33%	29%
Fluence above 10 MeV	-	-	5%
H(10)* above 10 MeV	-	-	11%
Δ	7.70	8.73	4.90
ξ^{max}	1.90	1.77	1.32

Table 8.10: Point 27 - spectral and convergence parameters.

From the values of the convergence parameters in Table 8.10, it is clear that the adoption of an unfolding code adapted to the high energy field provides the best results.

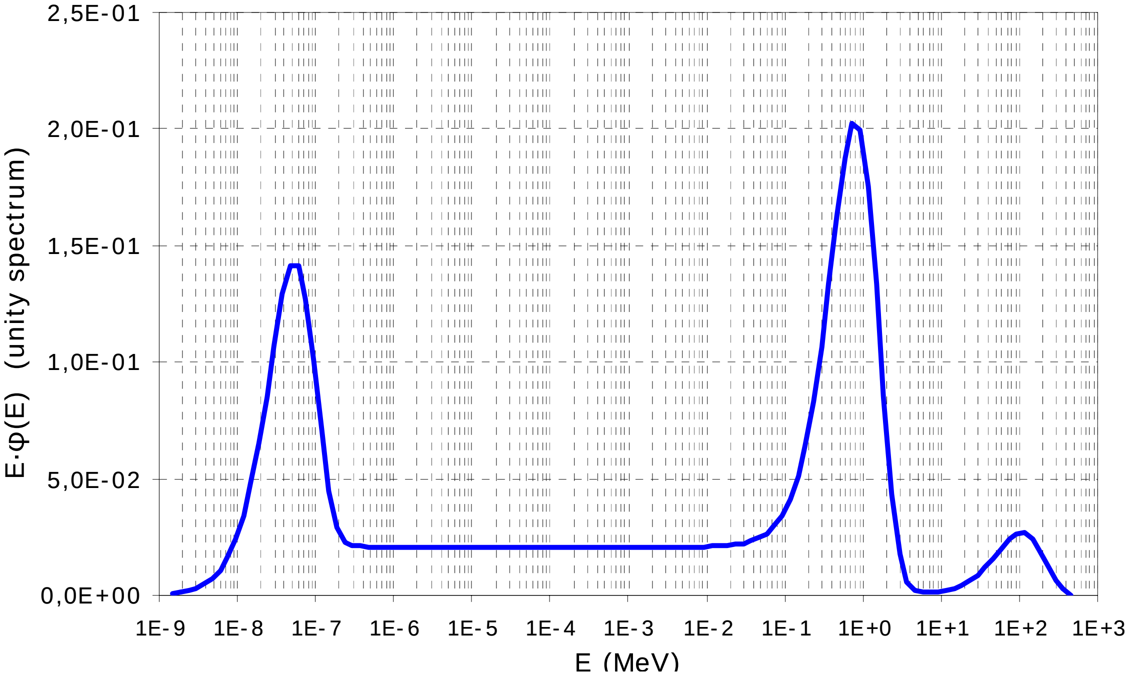

Figure 8.18: Neutron spectrum measured in point 27 (Normalized to unity integral and in equilethargic representation).

The agreement between the unfolded spectrum and the experimental data is shown in Figure 8.19.

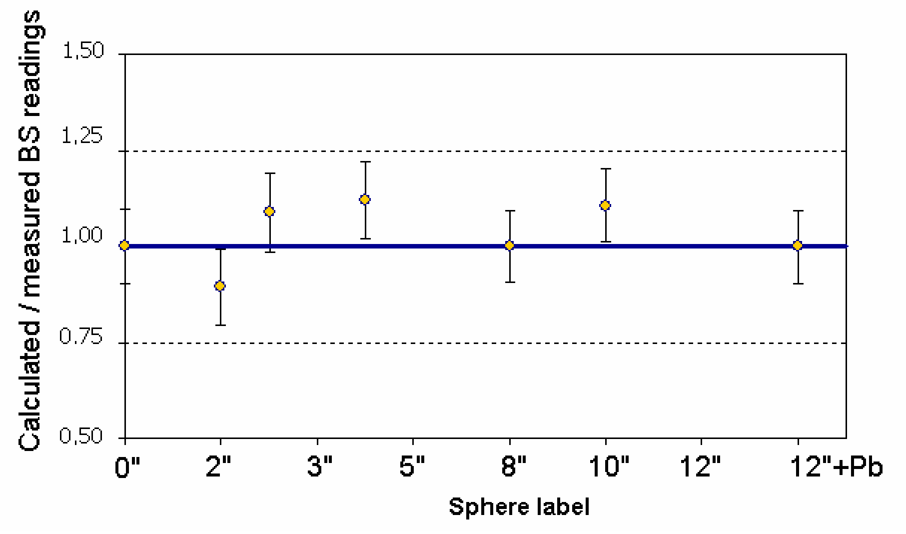

Figure 8.19: Point 27: ratio between the unfolded and the experimental BS readings.

The measurements in point 27, in terms of fluence, ambient dose equivalent and complementary measurements, are summarized in Table 8.11. The unfolded data have been derived with the high energy model.

Point 27: summary	
Φ (cm^{-2}.MU^{-1})	27.8±1.0
Monitor unit rate (MU.s^{-1})	2.3±0.4
$\dot{\Phi}$ (cm^{-2}.s^{-1})	64±11
$H^*(10)$ (μSv·h^{-1})	36 ± 7
$H^*(10)^{norm}$ (μSv.MU^{-1})	(4.31±0.15)·10^{-3}
LB6411^{norm} (μSv.MU^{-1})	(3.3±0.2)·10^{-3}
LB6411-Pb ^{norm} (μSv.MU^{-1})	(3.9±0.2)·10^{-3}
AUTOMESS^{norm} (μSv.MU^{-1})	(1.40±0.07)·10^{-3}

Table 8.11: Summary of the field and dosimetric quantities in point 27, obtained with the BSS and the complementary instruments. The superscript "*norm*" means that the quantity has been divided by the number of monitor units.

Again, the measurements with the LB6411 can be interpreted taking advantage of the unfolded neutron spectrum. The unfolded spectrum applied to the literature LB6411 response, (supposed null above 20 MeV) yields 131 pSv·cm^2. Since the LNF to literature LB6411 normalization ratio is 0.84, the LNF instrument should have responded 0.84 * 131 pSv·cm^2 = 110 pSv·cm^2, whilst the unfolded h_φ^* value (below 20 MeV) is 140 pSv·cm^2. The expected LB6411 underestimation faction is therefore 110/140 = 0.78, which is comparable with the measured 3.3/4.31 = 0.76.

The LB6411 workplace specific calibration factor in point 27 is

$$N_{27} = (H^{*}(10)\ /\ \mathrm{LB6411})_{\mathrm{point\ 27}} = 1.31 \pm 0.08$$

It should be noticed that LB6411-Pb reading is significantly higher (+18%) than that of the LB6411, due to the increased fraction of high energy neutrons (5% in fluence and 11% in dose equivalent) with respect to the other points.

8.7 Considerations on the measurements at DAΦNE

Owing to the different location and geometry of the three measurements points, different spectra have been observed. Moreover, due to changes in the operation mode of DAΦNE during the measurement period (four months), the points cannot be compared relying on the measured fluence rates. Nevertheless, interesting information can be drawn by comparing the neutron spectra.

As previously explained, point 20 mainly receives a skyshine spectrum, due to its location (see Fig. 8.9), the distance to DAΦNE and the presence of the shields. The giant resonance contribution is very poor (only 2.5% of the neutrons are in the evaporation peak) and the average conversion coefficient, h_{φ}^{*} = 58 pSv·cm^2, is the lowest among the observed points.

Point 25 has the peculiarity to lie along the direction of the DAΦNE injection lines, so the neutron field was expected to be, with respect to point 20:

- more influenced by the transmitted component;
- less influenced by the skyshine component.

As expected, the neutron spectrum in point 25 shows an evident giant resonance distribution, which contains 11% of the neutrons. Moreover, the average conversion coefficient, h_{φ}^{*} = 63 pSv·cm^2, is higher than in point 20.

Point 27 is strongly influenced by the “uncollided” source spectrum, since it directly faces the accelerator without shields. 35% of the neutrons are included in the evaporation peak, whilst 5% are in the high energy peak. The conversion coefficient, h_{φ}^{*} = 155 pSv·cm^2, is the highest among the measured points.

In general, a small fraction of high energy neutrons, contained in a peak at around 100 MeV, can be identified in the measured spectra. The importance of this component ranges in 1% to 5% in terms of fluence, and in 6% to 11% in terms of ambient dose equivalent. This component is transmitted through the lateral shields of the DAΦNE building. This is in agreement with literature data obtained at similar facilities.

As far as the rem counter LB6411 is concerned, workplace calibration factors from 1.10 up to 1.31 have been obtained, depending on the measurement site. If an "average" calibration factor of 1.20 is adopted for routine measurements, regardless the measurement point, an additional ±10% uncertainty should be accounted. This underlines the importance of the knowledge of the neutron spectrum to interpret the reading of the survey meters correctly.

Concerning the unfolding aspects, the FRUIT code provided satisfactory results and showed a high level of flexibility and interactivity. In fact, very small modifications were needed to adapt the calculation system from a Watt model to an evaporation model or an evaporation model with a high energy component.

Chapter 9

CONCLUSIONS AND PERSPECTIVES

As a result of the 1987 national referendum, the Italian nuclear energy program came to an end. For this reason, little or no activity has been promoted in nuclear-related fields in the past two decades. In particular, most of the Italian laboratories engaged in the field of neutron measurements and dosimetry have been closed soon after the retirement of scientists, who reached the retirement age almost simultaneously, since most of them started working in the 60s.

It is with these considerations in mind that I felt that it was important to work in the field of neutron dosimetry.

Eventually, being a qualified health physicist at the Frascati Laboratories of the National Institute of Nuclear Physics, greatly strengthens my mission goal.

The need to ensure the radiation protection surveillance around the INFN accelerators makes it mandatory to carry out research activities in the neutron field.

What stated above explains the entire structure of the thesis, which also refers to a variety of different experimental activities carried out in the past in different Italian research Institutes. However, the most important part of the thesis is the development of a simple procedure for the accurate evaluation of the neutron exposures around high energy accelerators.

Because of the importance of the neutron spectrometry for the correct evaluation of the radiation protection quantities, the entire issue has been thoroughly addressed by including such topics as:

- the identification of the “source terms”;
- the full characterization of a Bonner Sphere Spectrometer;
- the development of a new “dedicated” unfolding code, FRUIT (FRascati Unfolding InTeractive code),
- the “in field” spectrometric and dosimetric measurements.

After an initial overview on the radiation protection aspects around accelerator facilities and the current neutron dosimetry and spectrometry techniques, the Bonner Sphere Spectrometer in use at the LNF has been extensively studied. Its reproducibility, photon sensitivity and calibration have been investigated.

The response matrix of the spectrometer has been selected among the numerous versions available in literature, calculated from the 60s till the 90s. Since the selected matrix has been recently calculated and validated against experimental tests in reference monoenergetic neutron fields, only radionuclide sources were chosen for the validation tests. The accuracy of the adopted matrix resulted ±3%.

The “inverse problem” of the determination of the neutron spectrum from the sphere readings has been studied. The MITOM code, developed at the UAB, has been analyzed and some crucial points have been identified. With these starting points, the new visual and interactive unfolding code, FRUIT, has been written ad-hoc for the needs of the Frascati radiation protection group. Specific goals were the simplicity, the capability to provide reliable “on site” results, the independence of the result from the initial hypothesis, the interactivity, and a high degree of flexibility for application to different practical problems.

The FRUIT code has been tested with different reference spectra, with satisfactory results from point of view of both dosimetry and spectrometry. A variational test has been performed, in order to assess the typical “in field” accuracy of the unfolding code: ±3% and ±4% for the evaluation of the neutron fluence and the average fluence to dose equivalent conversion factor, respectively.

The whole LNF spectrometry system, composed by the instrument and the FRUIT code, has been finally used around the DAΦNE 510 MeV electron/positron collider, where some interesting measurement locations were identified. The neutron spectra in these points were expected to be composed by a skyshine constribution, arising from the unshielded upper window of DAΦNE, superposed to a transmitted high energy contribution. These hypotheses, also sustained in recent literature (Vylet, 1997; Sheu, 2003; Ban, 2000), were confirmed by the measured spectra. In addition, explanations were given to the differences encountered among the spectra measured in different locations. These places were also characterized in terms of ambient dose equivalent, allowing to evaluate the accuracy of a commercial rem counter which is routinely employed around DAΦNE. Correction factors from 1.11 to 1.31 were found, confirming the importance of the knowledge of the neutron spectrum even in the routine dosimetry evaluations.

Concerning the presence of high energy neutrons (around 100 MeV), the use of a 12” sphere with an internal lead shell allowed to estimate this component, even if very low (1% to 5%) in fluence. In order to take into account these neutrons, arising from the pseudo-deuteron and photo-pion effects when high Z materials are bombarded with high energy electrons, the FRUIT code has been easily adapted from a Watt model (up to 20 MeV) to a “high energy” model, showing a high level of flexibility.

This technique show promise for application around heavy charged particles accelerators or in the cosmic rays natural field. For these applications, where the high energy component becomes essential, two new spheres with lead and copper inserts have been designed, following the idea

of the NEMUS system from PTB (Wiegel, 2002a).
Moreover, calibrations and tests in specific high-energy fields, such as the CERF facility or the GSI, are planned. This would give another opportunity to test the instrument and the unfolding code, as well.

The LNF spectrometer has been used in monoenergetic neutron fields produced by accelerators. The facilities, at the JRC-IRMM Geel (Belgium) (from 0.3 to 19 MeV) and the ENEA-Frascati Fast Neutron Generator (2.5 and 14.1 MeV), provide quasi monoenergetic fields which peak locations are very well known. Nevertheless, the total neutron emission is known with quite high uncertainty (±10%). Anyway, these experiments were very useful to test the FRUIT code: after a small adaptation, the unfolding code was able to detect very precisely (±3%) the peak energy, and the total neutron fluence was measured with estimated uncertainty lower than 3%. Irradiations in monoenergetic reference fields, such as at the PTB or at the IRSN facilities, would be an important test to confirm these results.

Down to the low energy range, the LNF spectrometer has been already used around a 18 MV medical LINAC, with a double passive system: TLD pairs and gold foils. The preliminary results, obtained by using recent literature response functions, provided very satisfactory results. The spectra obtained with the two systems are compatible in terms of shape and total fluence. In this case, the FRUIT code has been adapted to a simple evaporation model, which allowed locating the main peak in the region between 0.2 and 0.3 MeV. Monte Carlo calculation and experimental validation of the TLD and gold foils response functions have been planned in the future.

Acknowledgements

Many pages would be necessary in order to thank individually all the people who, in several ways, supported me during this work. I will try to recall them, very briefly, with the aim to show that a good human environment is a fertile heart for growing good scientific contents.

I'm grateful to the colleagues of the INFN LNF Radiation Protection Group, Adolfo, Maurizio and Alfonso, for the valuable suggestions and the untiring support given in the preparation and the operation of the spectrometry measurements, ….especially when laborious expeditions were necessary to transport very heavy polyethylene spheres or lead loaded instruments on the top of the accelerator !!

Many thanks are due to the ex-colleagues from ENEA-Bologna, who made possible all the calibration and validation experiments in reference neutron fields. In particular, I wish to thank Gianfranco Gualdrini, who supported me with the Monte Carlo simulations needed to verify the response matrix of the spectrometer and to calculate the realistic spectra in the irradiation room.
And Fabio Monteventi, for the availability of the calibration room and for the "accuracy culture" that he transmitted to me during the years spent in the same laboratory.

Also, infinite thanks are due to the colleagues and friends from the UAB, especially Prof. Francisco Fernández, who gave me an extraordinary scientific and human support. When I came to him, proposing a Ph.D. project, he didn't know me, but he was as excited as I was, and trusted me since the first instant. Muchisimas gracias, Paco.

Now back to the family, which has been for me the starting point for all my steps. So, many thanks to my parents, who always encouraged me and taught me the universal recipe to face….not only the examinations, but all aspects of life: dedication and hard work.

And my wife Rocio, to whom this work is dedicated: she has been near to me always, with the extraordinary capability to compensate the attention that I subtracted from her for preparing this work, with an increased sweetness and affection.

References

Alevra, 1992

Alevra, A. V., Cosack, M., Hunt, J. B., Thomas, D. J., Schraube, H. *Experimental determination of the response of four Bonner spheres sets to monoenergetic neutrons (II).* Radiat. Prot. Dosim. **40**(1-4), 91-102 (1992).

Alevra, 2002

Alevra, A. V. and Plostinaru, V. D. *Characterisation of the IPNE Bonner sphere spectrometer by comparison with the PTB system.* Nucl. Instr. and Meth. A **476**, 21-25 (2002).

Alevra, 2003

Alevra, A. V. and Thomas, D. J. *Neutron spectrometry in mixed fields: multisphere spectrometers.* Radiat. Prot. Dosim. **107**(1-3), 37-72 (2003).

Bakali, 2001

Bakali, M. *Espectrometria neutronica en las centrales nucleares mediante un sistema de esferas Bonner.* Ph. D. Thesis, Universidad autonoma de Barcelona (2001). (In Spanish).

Ban, 2000

Ban, S., Namito, Y., Hirayama, H., Terunuma, N., Urakawa, J., Sato, T., Yuasa, R., Shin, K., Lee, H. S., Bak, J. S. *Measurements of photoneutron spectra from thick Pb target bombarded by 1.2 and 2.0 GeV electrons*. 2nd International Workshop on EGS, Tsukuba (Japan), 8-12 Aug. 2000. KEK Proceedings 200-20, 130-134 (2000).

Barquero, 2005

Barquero, R., Mendez, R., Vega-Carrillo, H. R., Iñiguez M. P. and Edwards, T. M. *Neutron spectra and dosimetric features around an 18 MV LINAC accelerator.* Health Phys. **88**(1), 48-58 (2005).

Bartlett, 2003

Bartlett, D. T., Chartier, J. –L., Matzke, M., Rimpler, A., Thomas, D. J. *Concepts and quantities in spectrometry and radiation protection.* Radiat. Prot. Dosim. **107**(1-3), 23-35 (2003).

Bedogni, 2000

Bedogni, R. *Qualificazione di un'unità di irraggiamento per la metrologia dei neutroni veloci: valutazioni sperimentali e Monte Carlo.* Post Graduate Specialization School Thesis in *Fisica Sanitaria*, University of Bologna (2000). (In Italian).

Bedogni, 2001

Bedogni, R., Fantuzzi, E. and Monteventi, F. *ENEA personal dosemeters to assess Hp(10) and Hp(0.07)*. Radiat. Prot. Dosim. **96**(1-3), 187-190 (2001).

Bedogni, 2002

Bedogni, R., Gualdrini, G. and Monteventi, F. *Field parameters and dosimetric characteristics of a fast neutron calibration facility: experimental and Monte Carlo evaluations*. Nucl. Instr. Meth. A **476**, 381-385 (2002).

Bedogni, 2002a

Bedogni, R. and Fantuzzi, E. *A personal neutron monitoring system based on CR-39 recoil proton track detectors: assessment of Hp(10) using Image process algorithms*. Radiat. Prot. Dosim. **101**(1-4), 183-186 (2002).

Bedogni, 2003

Bedogni, R. *Development of a reader for the routine analysis of CR-39 fast neutron dosemeters: improvement of the dosimetric performance using automatic vision and motion tool.* Radiat. Meas. **36**(1-6), 239-243 (2003).

Bedogni, 2004

Bedogni, R., Monteventi, F., Gualdrini, G. *Caratterizzazione degli impianti di irraggiamento per la dosimetria dei neutroni termici presso l'Istituto di Radioprotezione dell'ENEA.* ENEA Technical Report RT/2004/38/ION. ISSN/0393-3016.

Bedogni, 2006

Bedogni, R, Angelone, M., Esposito, A. and Chiti, M. *Inter-comparison among different TLD based techniques in a standard multisphere assembly for the characterization of neutron fields.* (In press on Radiat. Prot. Dosim.).

Bedogni, 2006a

Bedogni, R., Esposito, A., Angelone, M., Chiti, M. *Determination of the response to photons and thermal neutrons of new LiF based TL materials for radiation protection purposes.* (In press on Trans. Nucl. Sci.).

Bedogni, 2006b

Bedogni, R. *Registro della sorveglianza fisica del complesso DAΦNE.* INFN, Laboratori Nazionali di Frascati (2006). (*official document of the physical surveillance at the LNF, in italian).*

Birattari, 1990

Birattari, C., Ferrari, A., Nuccetelli, C., Pelliccioni, M. and Silari, M. *An extended range neutron rem counter.* Nucl. Instrum. Methods A **297**, 250-257 (1990).

Birattari, 1998

Birattari, C., Esposito, A., Ferrari, A., Pelliccioni, M., Rancati, T. and Silari, M. *The extended range neutron rem counter LINUS: Overview and latest developments.* Radiat. Prot. Dosim. **76** (3), 135-148 (1998).

Birattari, 1998a

Birattari, C., Ferrari, A., Hoefert, M., Otto, T., Rancati, T. and Silari, M. *Recent results at the CERN-EC high energy reference field facility*. Pages 219 to 234 in Proceedings of the Third Specialists Meeting on Shielding Aspects of Accelerators, Targets and Irradiation Facilities (SATIF3), OECD/NEA, Paris (1998).

Bramblett, 1960

Bramblett, R. L., Ewing, R. I. and Bonner, T. W. *A new type of neutron spectrometer.* Nucl. Instr. Meth. **9**, 1-12 (1960).

Brooks, 2002

Brooks, F. D. and Klein, H. *Neutron spectrometry – historical review and present status.* Nucl. Instr. Meth. A **476**, 1-11 (2002).

Budzanowski, 1995

Budzanowski, M. and Burgkhardt, B. *Thin* ^{6} ^{7}*LiF:Mg,Cu,P and* ^{6} ^{7}*LiF:Mg,Ti detectors for automatic albedo neutron dosimetry*. Radiat. Meas. **24**(4), 445-448 (1995).

Burgkhardt, 1997

Burgkhardt, B., Fieg, G., Klett, A., Plewnia, A. and Siebert, B. R. L. *The neutron fluence and H*(10) response of the new LB 6411 Rem counter.* Radiat. Prot. Dosim. **70** (1-4), 361-364 (1997).

d’Errico, 2003

d’Errico, F., Matzke, M. *Neutron spectrometry in mixed fields: superheated drop (bubble) detectors.* Radiat. Prot. Dosim. **107**(1-3), 111-124 (2003).

Doroshenko, 1977

Doroshenko, J. J., Kraitor S. N., Kuznetsova, T. V., Kushnereva, K. K. and Leonov, E. S. *New methods for measuring neutron spectra with energy from 0.4 eV to 10 MeV by track and activation detectors.* Nucl. Technol. **33**, 296-304 (1977).

Elevant, 2002

Elevant, T. *Fusion neutron energy spectra measured by time-of-flight spectrometers.* Nucl. Instr. Meth. A **476**, 485-489 (2002).

Esposito, 1992

Esposito, A., Pelliccioni, M. *DAΦNE shielding.* INFN-LNF Technical report LNF-92/044 (IR) (1992).

Eurisys, 1999

Eurisys. *Compteur ^{3}He.* Technical Report, Eurisys. Z.I. La vallée du Parc. 37600 Loches, France (1999).

Fantuzzi, 2002

Fantuzzi, E., Morelli, B., Falangi, G., Patrizii, L. and Togo, V. *CR-39 acceptance test and optimization for fast neutron dosimetry applications.* Radiat. Prot. Dosim. **101**(1-4), 573-578 (2002).

Ferrari, 1995

Ferrari, A. and Pelliccioni, M. *The effect of air on the dose equivalent at 10 mm depth in the ICRU sphere.* Radiat. Prot. Dosim. **60**(4), 243-247 (1995).

García, 2005

García. M. J., Amgarou, K., Domingo, C., Fernández, F. *Neutron Response of two CR-39 personal dosemeters with air and nylon converters*. Radiat. Meas. **40**(2-6), 607-611 (2005).

Gilvin, 2001

Gilvin, P. J., Bartlett, D. T., Shaw, P. V., Steele, J. D. and Tanner, R. J. *The NRPB PADC neutron personal dosimetry service.* Radiat. Prot. Dosim. **96**(1-3), 191-195 (2001).

Gressier, 2004

Gressier, V., Lacoste, V., Lebreton, L., Muller, H., Pelcot, G., Bakali, M., Fernandez, F., Thomas, M., Roberts, N. J., Thomas, D. J., Reginatto, M., Wiegel, B., Wittstock, J. *Characterization of the IRSN facility CANEL/T400 producing realistic neutron fields for calibration and test purposes.* Radiat. Prot. Dosim. **110**(1-4), 523-527 (2004).

Griffith, 1990

Griffith, R. V. and Tommasino, L. *Etch track detectors*, pages 323-426 in *Dosimetry of Ionizing Radiation*, Vol. III, Kase, K. R., Bjarngard, B. E. and Attix, F. H. Eds. (Academic Press, New York) (1990).

Gualdrini, 2004

Gualdrini, G., Bedogni, R., Monteventi, F. *Developing a thermal neutron irradiation system for the calibration of personal dosemeters in terms of Hp(10).* Radiat. Prot. Dosim. **110**(1-4), 43-48 (2004).

Gualdrini, 2004a

Gualdrini, G., Bedogni, R., Fantuzzi, E., Mariotti, F. *The ENEA criticality accident dosimetry system: a contribution to the 2002 international intercomparison at the Silene reactor.* Radiat. Prot. Dosim. **110**(1-4), 465-469 (2004).

Hajek, 2002

Hajek, T., Berger, T., Schöner, W. and Vana, N. *Analysis of the neutron component at high altitude mountains using active and passive measurement devices.* Nucl. Instr. Meth. A **476**, 69-73 (2002).

Hertel, 1985

Hertel, N. E. and Davidson, J. W., *The response of Bonner spheres to neutrons from thermal energies to 17.3 MeV.* Nucl. Instr. and Meth. A **238**, 509-516 (1985).

Hoefert, 1980

Hoefert, M. and Raffnsoe, C. *Measurement of absolute absorbed dose and dose-equivalent response for instruments used around high-energy proton accelerators.* Nucl. Instrum. Methods **176,** 443-448 (1980).

IAEA, 1990
International Atomic Energy Agency - Technical Reports Series n. 318, *Compendium of neutron spectra and detector responses for radiation protection purposes.* IAEA, Vienna (1990).

IAEA, 2001
International Atomic Energy Agency - Technical Reports Series n. 403, *Compendium of neutron spectra and detector responses for radiation protection purposes. Supplement to Technical Report Series No. 318.* IAEA, Vienna (2001).

ICRP, 1964
International Commission on Radiological Protection. *Report of Committee IV on Protection Against Electromagnetic Radiation Above 3 MeV and Electrons, Neutrons and Protons.* Publication 4. (Oford: Pergamon Press) (1964).

ICRP, 1991
International Commission on Radiological Protection. *1990 Recommendations of the International Commission on Radiological Protection.* Publication 60. Ann. ICRP 21(1-3) (Oford: Pergamon Press) (1991).

ICRP, 1995
International Commission on Radiological Protection. *Age-Dependent Doses to Members of the Public from Intakes of Radionuclides: Part 3. Ingestion Dose Coefficients.* Publication 69. (Oford: Pergamon Press) (1995).

ICRP, 1996
International Commission on Radiological Protection. *Age-Dependent Doses to Members of the Public from Intakes of Radionuclides: Part 4. Inhalation Dose Coefficients.* Publication 71. (Oford: Pergamon Press) (1996).

ICRP, 1996a
International Commission on Radiological Protection. *Conversion Coefficients for Use in Radiological Protection against External Radiation.* Publication 74. (Oford: Pergamon Press) (1996).

ICRU, 1985
International Commission on Radiation Units and Measurement. *Determination of Dose Equivalents Resulting from External Radiation Sources.* Report 39. (Bethesda, Maryland: ICRU) (1985).

ICRU, 1988
International Commission on Radiation Units and Measurement. *Determination of Dose Equivalents resulting from External Radiation Sources – Part 2.* Report 43. (Bethesda, Maryland: ICRU) (1988).

ICRU, 1992
International Commission on Radiation Units and Measurement. *Measurement of Dose Equivalents from External Photon and Electron Radiations.* Report 47. (Bethesda, Maryland: ICRU) (1992).

ICRU, 1993
International Commission on Radiation Units and Measurement. *Quantities and Units in Radiation Protection Dosimetry.* Report 51. (Bethesda, Maryland: ICRU) (1993).

ICRU, 1998
International Commission on Radiation Units and Measurement. *Conversion Coefficients for Use in Radiological Protection against External Radiation.* Report 57. (Bethesda, Maryland: ICRU) (1998).

ICRU, 2001
International Commission on Radiation Units and Measurement. *Determination of operational dose equivalent quantities for neutrons.* Publication 66. (Bethesda, Maryland: ICRU) (2001).

ISO, 1998
International Standard ISO 8529. *Reference neutron radiations – Part 3: Calibration of area and personal dosimeters and determination of their response as a function of neutron energy and angle of incidence.* International Standard ISO 8529-3 (1998).

ISO, 2000
International Standard ISO 8529. *Reference neutron radiations – Part 2: Calibration fundamentals of radiation protection devices related to the basic quantities characterizing the radiation field.* International Standard ISO 8529-2 (2000).

ISO, 2001

International Standard ISO 8529. *Reference neutron radiations – Part 1: Characteristics and methods of production*. International Standard ISO 8529-1 (2001).

ISO, 2001a

International Standard ISO 12789. *Reference neutron radiations: Characteristics and methods of production of simulated workplace neutron fields.* International Standard ISO 12789 (2001).

Klein, 2003

Klein, H. *Neutron spectrometry in mixed fields: NE213/BC501A liquid scintillation spectrometers.* Radiat. Prot. Dosim. **107**(1-3), 95-109 (2003).

Klett, 2005

Klett, A. (Berthold Technologies) Private Communication.

Lacoste, 2004

Lacoste, V., Gressier, V., Pochat, J. –L., Fernández, F., Bakali, M., Bouassoule, T. *Characterization of Bonner Sphere systems at monoenergetic and thermal neutron fields.* Radiat. Prot. Dosim. **110**(1-4), 529-532 (2004).

Lowry, 1984

Lowry, K. A. and Johnson, T. L. *Modification to iterative recursion unfolding algorithms and computer codes to find more appropriate neutron spectra.* NRL Report 5340 (Washington, DC: Naval Research Laboratory) (1984).

Lowry, 1986

Lowry, K. A. and Johnson, T. L., *The effect of the choice of response matrix on neutron spectra unfolded from Bonner sphere data.* Health Phys. **50**(4), 543 (1986).

Mao, 2000

Mao, X. S., Fassò, A., Liu, J. C., Nelson, W. R. and Rokni, S. *Bremmstrahlung Source Term Produced in Thick Targets by 50 MeV to 10 GeV Electrons.* SLAC-PUB-7722 (January 2000).

Mares, 1994

Mares, V. and Schraube, H. *Evaluation of the response matrix of a Bonner sphere spectrometer with LiI detector from thermal energy to 100 MeV.* Nucl. Instr. and Meth. A **337**, 461-473 (1994).

Matzke, 1994

Matzke, M. *Unfolding of pulse height spectra: the HEPRO program system.* Report PTB-N-19. (Braunschweig: Physikalisch-Technische Bundesanstalt) (1994).

Matzke, 2003

Matzke, M. *Neutron spectrometry in mixed fields: unfolding procedures.* Radiat. Prot. Dosim. **107**(1-3), 37-72 (2003).

McDonald, 2001

McDonald, J. C. *Determination of personal dose equivalents in accelerator radiation fields.* Radiat. Prot. Dosim. **96**(4), 423-427 (2001).

McElroy, 1967

McElroy, W. N., Berg, S., Crockett, T. and Hawkins, R. G. *A computer automated iterative method for neutron flux spectra determination by foil activation.* Report AFWL-TR-67-41 (Kirtland, NM: US Air Force Weapons Laboratory) (1967).

NCRP, 2004

National Council on Radiation Protection and Measurements. *Radiation Protection for particle accelerator facilities.* Report 144. NCRP (2004).

Parker, 1948

Parker, H. M. *Health Physics, Instrumentation, and Radiation Protection.* Adv. Biol. Med. Phys. **1**, 223 (1948).

Pelliccioni, 1987

Pelliccioni, M. and Esposito, A. *Measurements of gas bremmstrahlung in the Adone storage ring* Proceedings of the 20th Midyear Topical Symposium on of the Health Physics Society, *Health Physics of Radiation Producing Machines*, Busick, D. D. and Swanson, W. P., Eds., CONF-8602106 (National Technical Information Service, Springfield, Virginia), (1987).

Pelliccioni, 2000

Pelliccioni, M. *Overview of fluence to effective dose and fluence to ambient dose equivalent conversion coefficients for high energy radiation calculated using the FLUKA code.* Radiat. Prot. Dosim. **88**(4), 279-297 (2000).

Perey, 1978

Perey, F. G., *Least-squares dosimetry unfolding: the program STAY'SL.* Report ORNL/TM-6062 (Oak Ridge, TN: Oak Ridge National Laboratory) (1978).

Persico, 1968

Persico, E., Ferrari, E. and Segré, S.E. *Principles of Particle Accelerators.* W.A. Benjamin, NeW York (1968).

Reginatto, 1998

Reginatto, M. and Goldhagen, P. *A computer code for the deconvolution of multisphere neutron spectrometer data using the maximum entropy method.* Report EML-595 (New York: Environmental Measurement Laboratory) (1998).

Routti, 1980

Routti, J. T. and Sandberg, J. V., *General purpose unfolding program LOUHI78 with linear and non linear regulations.* Comput. Phys. Commun. **21**, 119-144 (1980).

Sanna, 1973

Sanna, R. S., *Thirty one group response matrices for the multisphere neutron spectrometer over the energy range Thermal to 400 MeV*. USAEC, HASL-267 (1973).

Sheu, 2003

Sheu, R. J., Wang, J. P., Chen, C. R., Liu, J., Chang, F. D. and Jiang, S. H. *Network-based real-time radiation monitoring system in synchrotron radiation research center.* Health Phys. **85**(4), 485-493 (2003).

Spiegelhalter, 2003

Spiegelhalter D. J. et al., WinBUGS Version 1.4 User Manual, MRC Biostatistics Unit.: http:/ www.mrc-bsu.cam.ac.uk/bugs (2003).

Spurny, 2004

Spurny, F. *Response of Thermoluminescence detectors to charged particles and to neutrons.* Radiat. Meas. **38**, 407-412 (2004).

Swanson, 1979

Swanson, W. P. *Radiological Safety Aspects of the Operation of Electron Linear Accelerators* (Vienna: International Atomic Energy Agency) STI/DOC/188 (1979).

Swanson, 1990

Swanson, W.P. and Thomas, R.H. *Dosimetry for radiological protection at high energy particle accelerators,* pages 1 to 161 in *The Dosimetry of Ionizing Radiation,* Vol. III, Kase, K.R., Bjarngard, B. and Attix, F.H., Eds. Academic Press, New York (1990).

Tagziria, 2003

Tagziria, H. and Hansen, W. *Neutron spectrometry in mixed fields: proportional counter spectrometers.* Radiat. Prot. Dosim. **107**(1-3), 73-93 (2003).

Thomas D. J., 1992

Thomas, D. J. *Use of the program ANISN to calculate response functions for a Bonner sphere set with a* ^{3}*He detector.* NPL Report RSA(EXT) 31. Teddington, National Physical Laboratory (1992).

Thomas D. J., 1994

Thomas, D. J., Alevra, A. V., Hunt, J. B., Schraube, H. *Experimental determination of the response of four Bonner sphere sets to thermal neutrons.* Radiat. Prot. Dosim. **54**(1-4), 25-31 (1994).

Thomas D. J., 1997

Thomas, D.J., Chartier, J.-L., Klein, H., Naismith, O.F., Posny, F. and Taylor, G.C. *Results of a Large Scale Neutron Spectrometry and Dosimetry Comparison Exercise at the Cadarache Moderator Assembly*. Radiat. Prot. Dosim. **70**(1-4), 313-322 (1997).

Thomas D. J., 2002

Thomas, D. J., Bardell, A. G.. Macaulay, E. M. Characterisation of a gold foil-based Bonner sphere set and measurements of neutron spectra at a medical accelerator. Nucl. Instr. and Meth. A**476**, 31-35 (2002).

Thomas D. J., 2002a

Thomas, D. J., Alevra, A. V. *Bonner sphere spectrometers – a critical review.* Nucl. Instr. and Meth. A **476**, 12-20 (2002).

Thomas R., 1997

Thomas, R. H. Editorial: *We have met the enemy and he is us.* Radiat. Prot. Dosim. **71**, 83-84 (1997).

Thomás, 2004

Thomás, M., Fernández, F., Bakali, M. and Muller, H. *MITOM: a new unfolding code based on a spectra model method applied to neutron spectrometry*. Radiat. Prot. Dosim. **110**(1-4), 545-548 (2004).

Vega-Carrillo, 2002

Vega-Carrillo, H. R. *TLD pairs, as thermal neutron detectors in neutron multisphere spectrometry.* Radiat. Meas. **35**, 251-254 (2002).

Vega-Carrillo, 2004

Vega-Carrillo, H. R., Manzanares-Acuña, E. *Background neutron spectrum at 2420 m above sea level.* Nucl. Instr. and Meth. A **524**, 146-151 (2004).

Veinot, 1998

Veinot, K. G., Hertel, N. E., Brooks, K. W. and Sweezy, J. E. *Multisphere neutron spectra measurements near a high energy medical accelerator.* Health Phys. **75**(3), 285-290 (1998).

Vylet, 1997

Vylet, V., Liu, J. C., Rokni, S. H. and Thai, L. –X. *Measurements of neutron spectra at the Stanford linear accelerator center*. Radiat. Prot. Dosim. **70**(1-4), 425-428 (1997).

Vylet, 2001

Vylet, V. and Liu, C. *Radiation Protection at high energy electron accelerators.* Radiat. Prot. Dosim. **96**, N. 4, 333-343 (2001).

Vylet, 2002

Vylet, V. *Response matrix of an extended Bonner sphere system.* Nucl. Instr. and Meth. A **476**, 26-30 (2002).

Vylet, 2005

Vylet, V. *Energy response of the lead loaded 12” sphere,* Private communication.

Wagner, 1961

Wagner, E. and Hurst, G. S. *A Geiger-Muller gamma-ray dosimeter with low neutron sensitivity.* Health Phys. **5,** 20-25 (1961).

Weise, 1995

Weise, K. *Mathematical foundation of an analytical approach to Bayesian statistical Monte Carlo spectrum unfolding.* Report PTB-N-24 (Braunschweig: Physikalisch-Technische Bundesanstalt) (1995).

Wiegel, 1994

Wiegel, B., Alevra, A. V. and Siebert, B. R. L. Calculation of the response function of Bonner spheres with a spherical ^{3}He proportional counter using realistic detector model. Report PTB-N-21. Braunschweig, Physikalish-Technische Bundesanstalt (1994).

Wiegel, 2002

Wiegel, B. and Alevra, A. V. *NEMUS – the PTB Neutron Multisphere Spectrometer: Bonner spheres and more.* Nucl. Instr. and Meth. A **476**, 36-41 (2002).

Wiegel, 2002a

Wiegel, B., Alevra, A. V., Matzke, M., Scherme, U. J. And Wittstock, J. *Spectrometry using the PTB neutron mulstisphere spectrometer (NEMUS) at flight altitudes and at ground level.* Nucl. Instr. and Meth. A **476**, 52-57 (2002).

William, 1992

William, H. P., Saul, A. T., William, T. V. and Brian, P. F. *Numerical recipes in fortran.* Cambridge University Press, Cambridge (1992).